University of Zürich

Physics Institute

MEMS Comb Actuator for Straining Carbon Nanotubes

Ozan Zeray

Master's Thesis

Supervisor: Prof. Mikael Perrin
Supervisor: Prof. Davide Bleiner
M.Sc. in Physics
July 2025

Universität Zürich[UZH]

Abstract

This thesis presents the design, simulation, and fabrication of a MEMS comb actuator for applying controlled uniaxial strain to carbon nanotubes (CNTs), enabling precise tuning of their electronic properties. CNTs exhibit exceptional mechanical and electrical characteristics, with their band structure being highly sensitive to strain. Traditional methods such as AFM-based straining suffer from non-uniform deformation and poor reproducibility. This work proposes a chip-integrated solution for uniform, scalable CNT straining.

COMSOL simulations were conducted to guide the MEMS actuator design and model its physical behavior. Based on these results, a device capable of achieving displacements up to 200 nm was designed which will strain the nanotube up to 10%. The actuator chip was then fabricated in a cleanroom, where various challenges were addressed using custom-developed techniques.

Post-fabrication, the actuator's displacement was validated through SEM imaging. To complement the experimental work, theoretical models based on the non-equilibrium Green's function (NEGF) formalism were developed to study the impact of strain on electronic transport.

This platform offers a reproducible, on-chip approach to exploring strain engineering in CNTs for advanced nanoelectronic and quantum devices. Integration of CNTs enables future strain-dependent electronic transport studies.

Acknowledgments

I would like to express my deepest gratitude to Prof. Mikael Perrin for welcoming me into his lab and supporting this work. I have greatly benefited from his approachable nature, insightful discussions, and access to his leading laboratory specializing in carbon-based quantum devices. My colleague, Peter Lendway, a PhD student in the same lab, has been incredibly helpful, collaborative, and patient in guiding me through the clean-room processes. I also thank PhD student Frederic Van Veen for engaging discussions on quantum phenomena at the nanoscale. Special thanks to the staff at IBM Zürich Binning-Rohrer Nanocenter, especially Ute Drechsler and Ronald Grundbacher, for their invaluable assistance with liftoff challenges and for engaging discussions on RIE, DRIE and Vapor HF processes. I am grateful to Prof. Johann Michler from EMPA Thun for his valuable assistance with COMSOL simulations and his expertise in the mechanics of nanostructures. I would like to thank Prof. Mathieu Luisier for enlightening conversations about NEGF calculations, his lectures on Quantum Transport at Nanoscale, as well as his PhD student Jiang Cao for generously dedicating time to debug the NEGF code and share his implementation.

Finally, I wish to acknowledge Prof. Daniele Passerone from EMPA Dübendorf for technical discussions on integrating LAMMPS simulations into the NEGF framework. I am particularly indebted to his PhD student Anooja Jayaraj for diligently verifying simulations and for her attentive support during our meetings.

Contents

1 Chapter 1 - Introduction

1.1 Systems

1.1.1 What are Carbon Nanotubes?

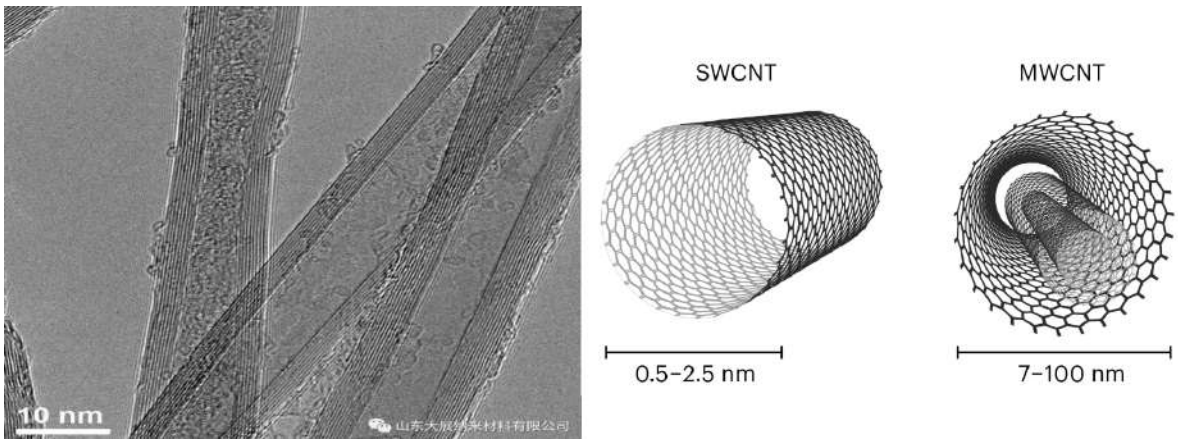

Figure 1: Transmission Electron Microscopy image of Multi-walled Carbon Nanotube (MWCNT) and pictorial description of these molecules with Single-walled Carbon Nanotube (SWCNT). [1] [2].

The story of carbon nanotubes begins with its discovery,significantly driven by the synthesis of molecular carbon structures in the form of C_{60} and other fullerenes, in 1991 as rolled graphitic carbon into tubular shape by Sumio Iijima [3]. Layers of rolling graphitic sheets of carbon creates Single layered and multi layered carbon nanotubes. Due to the hexagonal shape of the atomic lattice of these sheets, connection of the rolled sheet at its edges is only possible at certain angles of rolling, since not at every angle, chosen to roll the sheet around it, is so that the hexagonal lattice overlaps at the sheet edges. The way rolling angle determines how the edge of the sheet connects, which is called chirality, which in turn determines the periodicity of the lattice. Different periodicities in the lattice structure gives rise to electron band hamiltonian with different symmetries causing nanotube to be either metallic or semiconducting. The vast arsenal of carbon nanotube types stems mainly from many possible chiral tubes.

Aside from it's peculiar electron bands, the never ending interest in carbon nanotubes stems also from it's electrical, mechanical and thermal properties. Electrical characterization [4] shows that metallic tubes can withstand current densities as high as 6×10^6A cm^{-1} and have resistivity in the range of 5×10^{-6} cm, note that copper has a resistivity 1.77×10^{-6} cm. Mechanical characterization shows that carbon nanotubes, also referred as CNT's, can withstand enourmos strains. Their Young's modulus being in between 270 and 950 GPa and the tensile strength between 11 and 63 GPa. Comparing this with steel having a Young's modulus of 200GPa and tensile strength being 0.4 GPa [5], CNT's prove themselves clearly superior over the common structural materials. However this doesn't end here. Considering the thermal conductivity, it is shown that they exhibit conductivity greater than 3000 W/K m [6], while copper having 400 W/ K m and diamond having 1000 W/K m. The enthusiasm of integrating carbon nanotubes to nanodevices is thus further enchanced given that impressive thermal conductivity given that thermal management in nanosized devices becomes increasingly important as the

size of the device reduces.

1.1.2 What is MEMS? What is a MEMS Actuator?

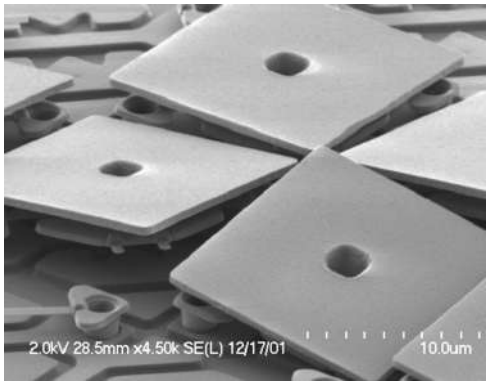

(a) Texas Instruments Digital Micro Mirror Array device. Ability to tilt the square reflecting panels sitting on micromechanical balances upon an electrical signal enables the modern projection technology. [7]

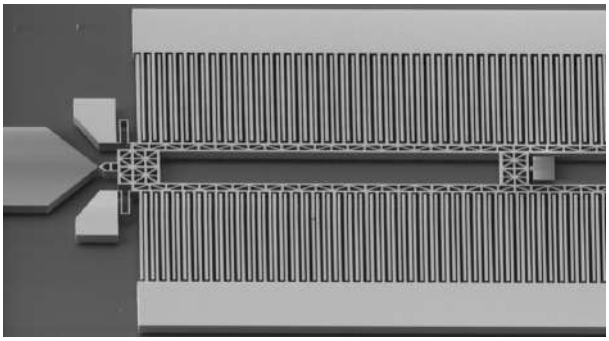

(b) Comb drive actuator fabricated by our laboratory for the purposes of break junction experiments. [8]

The acronym MEMS stands for Micro electro mechanical systems which refers to devices that have micron or smaller sized suspended, hanged, balanced or alike structures, mostly made of silicon, that can move back and forward, in or out of plane, rotate, oscillate in position, bend or perform other mechanical motions being in influence by electrical fields. MEMS is a direct child of semiconductor manufacturing technology, experiencing its burst in 80's. Although initial MEMS devices are based in silicon, currently MEMS made of plastic, ceramics, glass, etc. are also gaining popularity due to interests in applying MEMS to biology, which requires biocompatible materials. The MEMS device used in this work is called a " MEMS Actuator" or a " Comb Drive". Idea of this structure is that if two charged plates are brought together, they attract. Then a body suspended in air by a spring with a plate surface facing another plate at a small distance can be pulled by it via charging these plates with opposite charges. Furthermore in order to multiply this electrostatic attraction, series of facing plates can be fabricated so that enough pulling force can be generated.

1.2 Motivation

1.2.1 Previous Experiments On Straining Nanotubes

A wide range of experiments have explored the use of mechanical strain to modify the electrical properties of carbon nanotubes (CNTs), particularly for applications in sensing and device tuning. Various methods have been employed to apply strain to CNTs. For instance, some studies utilize the tip of an Atomic Force Microscope (AFM) to directly stretch individual nanotubes [9], while others embed CNTs in elastomeric substrates to induce strain through substrate deformation [10]. Another common approach involves depositing CNTs onto surfaces where buckling arises naturally during the drying process of the solvent, allowing post hoc identification of strained tubes [11]. However, many of these techniques either depend on bulk samples of CNTs or are not readily integrated

into chip-scale devices. This highlights the significance of a MEMS-based platform for CNT straining, as it offers both a novel approach and a scalable, on-chip solution that can enable more controlled and reproducible experiments, opening new possibilities for fundamental research and technological applications.

One study reports that band structure of a carbon nanotube (NT) can be dramatically altered by mechanical strain [9]. In their approach, an Atomic Force Microscope (AFM) tip is used to simultaneously exert mechanical strain on the carbon nanotube and apply an electrostatic gate. Through this setup, they demonstrate that strain can induce a band gap in metallic nanotubes and effectively tune the band gap in semiconducting ones. Theoretical models support these findings, predicting that strain-induced changes in the band gap can be as large as 100 meV per 1 percent of applied elongation. However in this approach the straining is not uniform along the axis as it bends the tube. Furthermore the presence of AFM tip causes interaction with carbon orbitals causing additional effects.

Another study reports a resistance increase from 85 kΩ up to 200 kΩ in a strained carbon nanotube, where the strain is applied using an AFM tip [12]. However, a significant challenge in this setup is the variability of the contact resistance between the carbon nanotube and the metal electrodes, which are deposited directly on top of the tubes to pin them in place. Any slight movement or slippage of the nanotube under the contacts leads to uncontrolled changes in contact resistance, complicating the interpretation of the intrinsic electrical response to strain. This issue severely limits the reproducibility and reliability of such measurements. In contrast, a MEMS-based on-chip straining platform offers a more stable and integrated solution. Since the nanotubes can be suspended and anchored in a controlled microfabricated environment, the strain can be applied uniformly without the unintended movement at the contact points.

2 Chapter 2 - Basic Physics

2.1 Physics of Quantum Dots

The primary distinction between macroscale electronics and nanoelectronics lies in a few key aspects, of which are the quantization of electron energies, the absence of electrostatic potential screening and electron-electron interaction due to very small confinement in nanostructures. The lack of screening leads to electrons in the conductor experiencing the potential field created by nearby macroscopic electrodes, known as gate electrodes. As a result, the interaction between the gate electrode and the electrons within the conductor becomes significant, differing from what is typically observed in macroscale electronics. Below is a plot of the potential field over the wire.

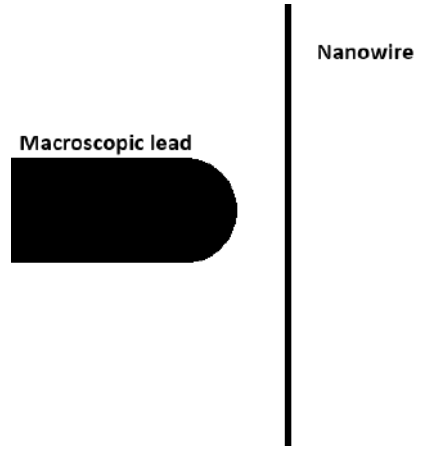

(a) Schematic of the nanostructure.

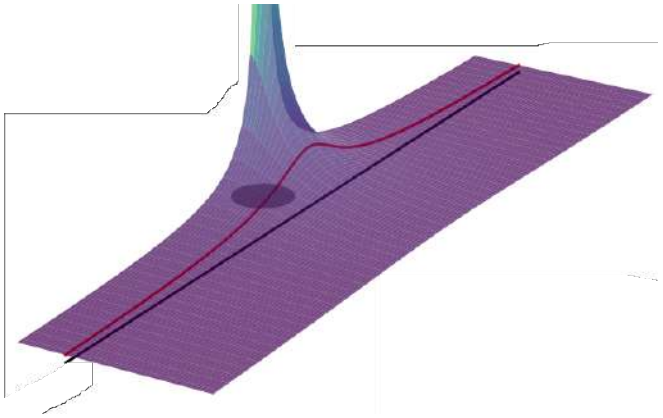

(b) Plot of the $1/r$ potential field generated by the black dot, as experienced along the nanowire.

Figure 3: In (b), the black circle represents the gate electrode, and the black line denotes the nanowire. The red line indicates the magnitude of the potential field along the wire. Due to the absence of screening in the nanowire, this potential landscape persists within it. Consequently, electrons moving along the one-dimensional wire encounter a potential barrier shaped as shown. Grounding the gate electrode removes this barrier, allowing electron flow. This mechanism underlies the operation of field-effect transistors and enabling transport by gating in Coulomb Blockade devices as we will see below.

2.1.1 Single Electron Box

In this section and the next, we will go through couple of models for the single electron transporting devices.

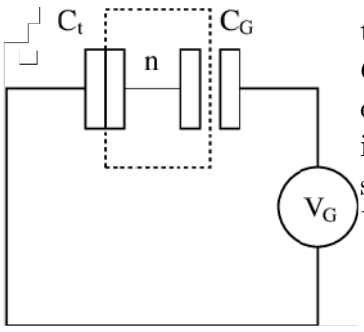

Figure 4: Single electron box circuit.

We begin with single electron box. Consider a circuit with two capacitors, C_t with ability to also tunnel electrons and C_G. The box with dashed lines denote the island on which electrons reside and n is the integer amount of charge on this island. Due to charges on the island accumulating on two sides we have $Q_t - Q_G = en$ and from equilibrium of voltages $V_G = \frac{Q_t}{C_t} - \frac{Q_G}{C_G}$.

$$Energy(Q_t, Q_G, V_g) = \frac{1}{2}(\frac{Q_t^2}{C_t} + \frac{Q_G^2}{C_G}) - Q_G V_G$$

where $-Q_G V_G$ is due to bringing electrons to the potential at gate electrode. Therefore we have the relation:

$$\begin{bmatrix} en \\ V_G \end{bmatrix} = \begin{bmatrix} 1 & -1 \\ \frac{1}{C_t} & \frac{1}{C_G} \end{bmatrix} \cdot \begin{bmatrix} Q_t \\ Q_G \end{bmatrix}$$

Finding en and V_G in terms of Q_t and Q_G then plugging it in the energy equation gives us [13]

$$E(n, V_G) = \frac{e^2}{2(C_t + C_G)}(n + C_G V_G)^2 - \frac{(C_G V_G)^2}{2C_G}$$

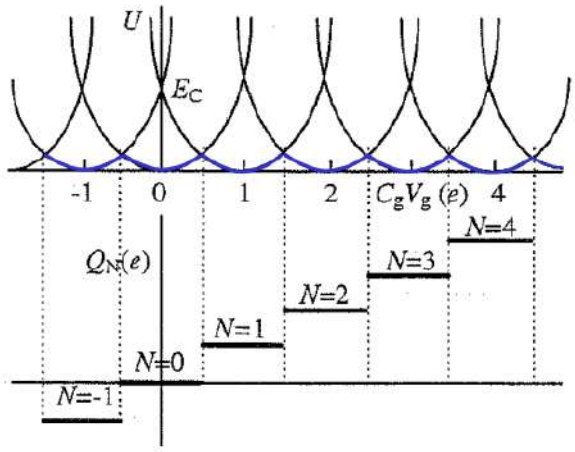

Figure 5: electron number n - gate voltage diagram of energy in the circuit. [14]

Plotting the energy equation then results in periodically spaced parabolic levels. When the system has n=0 and the voltage is high, due to the option of electron tunnelling, the system has access to adjacent parabolas by losing an electron, which sets n=-1. With this we can tune the electron in the box. Notice that also as we increase the voltage, energy level spacing between n=0 and n=1, that is the vertical gap between parabolas, decreases.

2.1.2 Single Electron Transistor

Now we consider the island between two electrodes. When the gap between two conductors shrinks to an incredibly tiny scale, the energy needed to push a lone electron through it becomes noticeable. If you stack two junctions in a line with a conducting island in the middle, or isolate a single junction in a high-resistance setup, this charging energy, E_C, imposes a limit on the current passing through the system.

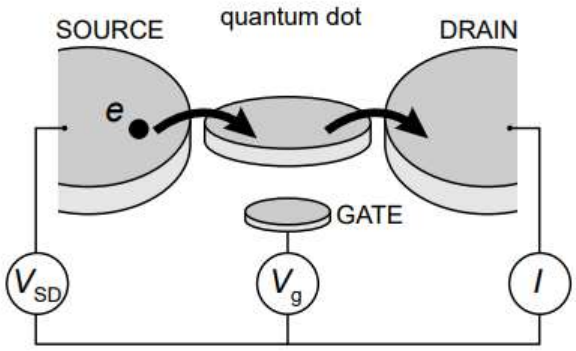

Figure 6: The diagram illustrates a basic nano island circuit. In this design, the source and drain electrodes are positioned very close to the nano metal island in the center, which is simply a collection of atoms whose shape is not important. A third gate electrode is placed nearby, though not as close, so that it can still influence the potential of the nano island.

To quantitatively understand the system we start by total energy calculation of the nano island system with circuit theory. We denote the capacitance of source, gate and drain between quantum dot as C_S, C_D and C_G. Also, defining the charge on the dot as $Q = C_GV_G + C_SV_S + C_DV_D$ and writing the energy of the circuit in terms of quantized charge on the dot and the gate voltage, we get a similar charging energy. [13]

$$E_{charging}(n, V_G) = \frac{e^2}{2(C_S + C_G + C_D)}(n + Q)^2$$

Using this formula from the very simple model of 3 capacitors connected to same node with different applied voltages, we will be able to understand the Coulomb blockade in the next section.

2.1.3 Coulomb Blockade

The coulomn blockade refers to the situation in nano circuits where the electron transmissin from one lead to another is suppressed to a degree that electron flow is not present. This phenomena is most often seen in single electron transmission processes, where for the electron to flow, it has to gain a certain energy that is not available due the system being at low temperatures. Therefore this unfullfilled energy balance does not allow the electron to tunnel to a higher energy state on the dot and then tunnel to the drain electrode.

To illustrate the following reasoning, consider the given figure

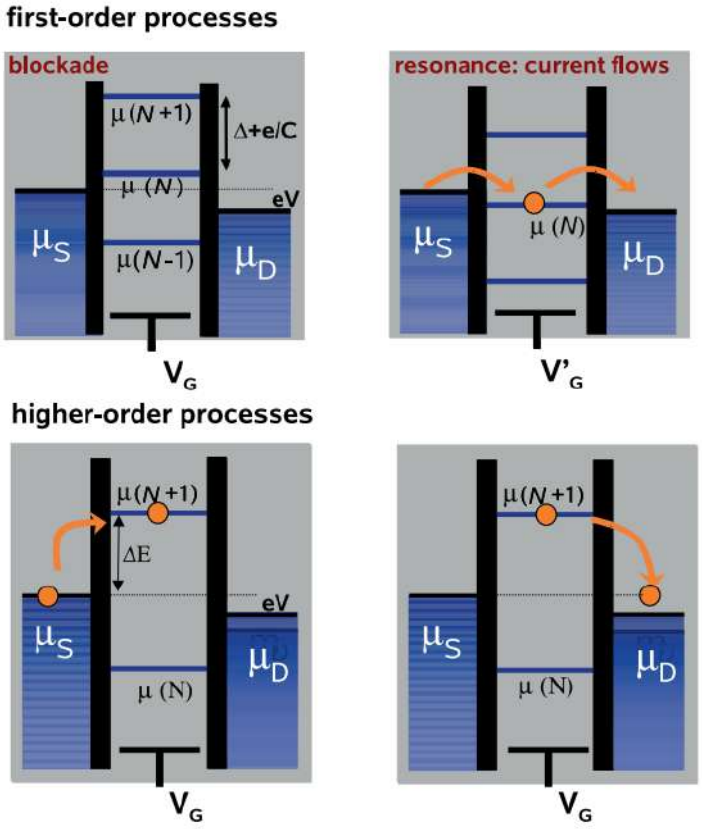

Figure 7: Possible transport schemes over energy levels of a Coulomb Blockade device [15]

The source and drain electrodes are denoted by their chemical potential μ_S and μ_D which in turn expresses the filling of the energy states. From the charging energy formula of previous single electron transmission section, we find that adding one electron to the island with n electrons requires

$$E_{charging}(n+1) - E_{charging}(n) = \frac{e^2}{2C_\Sigma}[2(n+Q)+1]$$

Considering a system where C_S and C_D are the same while V_S=$-V_D$ sets the definition

of Q as $Q = C_G V_G$, plugging this into the previous formula

$$E_{charging}(n+1) - E_{charging}(n) = \frac{e^2(2n+1)}{2C_{\Sigma}} + \frac{e^2 C_G V_G}{C_{\Sigma}}$$

From this we see how the gate voltage increases the level spacing of the dot.

$$E = \frac{2C^2V^2 + CCgV^2 + CCgVg^2 + \frac{eN^2}{2}}{C_{\Sigma}}$$

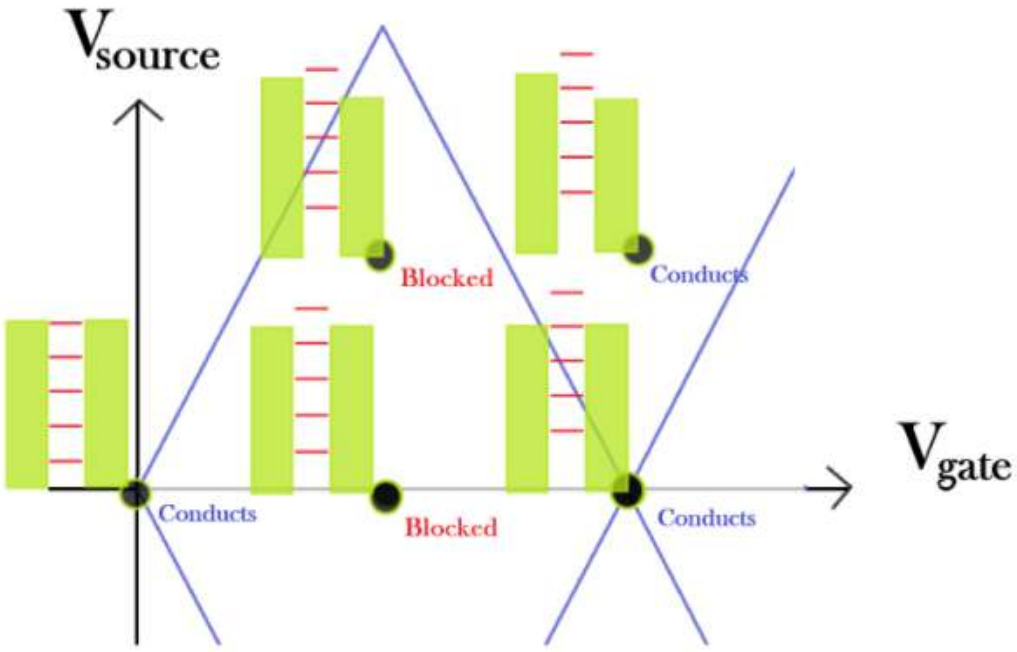

Figure 8: Diagram of coulomb diamonds. Here the source and drain voltages are denoted by right and left green columns that are placed next to each black dot. In the middle of these columns the energy states of quantum dot is present. These level are raised up or down by the gate voltage seen at the x axis.

The figure above shows the parameter space of source and gate voltages in a single-electron transistor. The blue lines form diamond-shaped regions where the measured current within is zero, indicating that current is blocked. The green illustrations next to each data point help visualize the energy levels. When no quantum dot energy level lies within the source-drain voltage window, current is suppressed. However, if an energy level falls within this gap, electrons can tunnel through, allowing current to flow. This phenomenon, known as Coulomb blockade, illustrates the principle of energy conservation: electrons can only tunnel if a quantum state exists within the energy range allowed by the source and drain. Importantly, for Coulomb blockade to occur, the energy levels on the island (quantum dot) must be sufficiently quantized. If the energy levels were continuous, their density would scale linearly with the source-drain voltage, resulting in ohmic (linear) current–voltage behavior instead.

2.1.4 Helium Atom as an example

In order to have significant energy level quantization in quantum dots, one needs very small potential wells such as a nanometer sized metallic island. Another significant contribution in these dots come from electron electron interactions, which are not negligible at those scales. To explore the electron-electron interaction in quantum dots, we can start by considering the smallest possible quantum dot, which is a single atom. If we apply the modified Bohr formula for hydrogenic atoms, $Energy = \frac{-R_0 Z^2}{n^2}$, where R_0 is the Rydberg constant and Z is the atomic number, we can calculate the ground state energy for a helium atom. For helium, with $Z = 2$, the ground state energy would be $-4R_0 = 54.4\,\text{eV}$. However, when we measure the ionization energy of helium, we find that the energy required to remove the first electron is 24.5 eV, as shown by experimental data from the NIST Atomic Spectrum Database, and the energy required to remove the second electron is 54.4 eV.

Now, if we were to place two electrons in the ground state of helium, we would expect the total energy to be $-2 \times 54.4\,\text{eV} = -108.8\,\text{eV}$, assuming that there is no electron-electron interaction. But in reality, it is observed that the total energy for the two-electron system is $-24.5\,\text{eV} - 54.4\,\text{eV} = -78.9\,\text{eV}$. The difference of 29.9 eV between the expected and measured energies represents the energy held between the two electrons due to their mutual interaction. This difference highlights that the non-interacting approximation is not accurate and emphasizes the importance of considering electron-electron interactions when modeling systems reaching atomic sizes.

2.2 Physics of Carbon Nanotubes

Carbon nanotubes (CNTs) are hollow cylindrical structures composed entirely of carbon atoms. They come in various forms, including nanotube-like structures, but the two fundamental types are multi-walled nanotubes (MWNTs), which have diameters around 10 nm, and single-walled nanotubes (SWNTs) with diameters of approximately 1 nm.

CNTs can be visualized as graphene sheets rolled into cylinders. Since there are multiple ways to roll a graphene sheet, CNTs theoretically exist in an infinite variety, assuming no restrictions on diameter. The orientation of a CNT's axis relative to the graphene crystal axes significantly affects its electronic properties. The structure of a CNT is defined by a wrapping vector, which encircles the nanotube's circumference, forming a closed loop where the vector's tip aligns with its starting point.

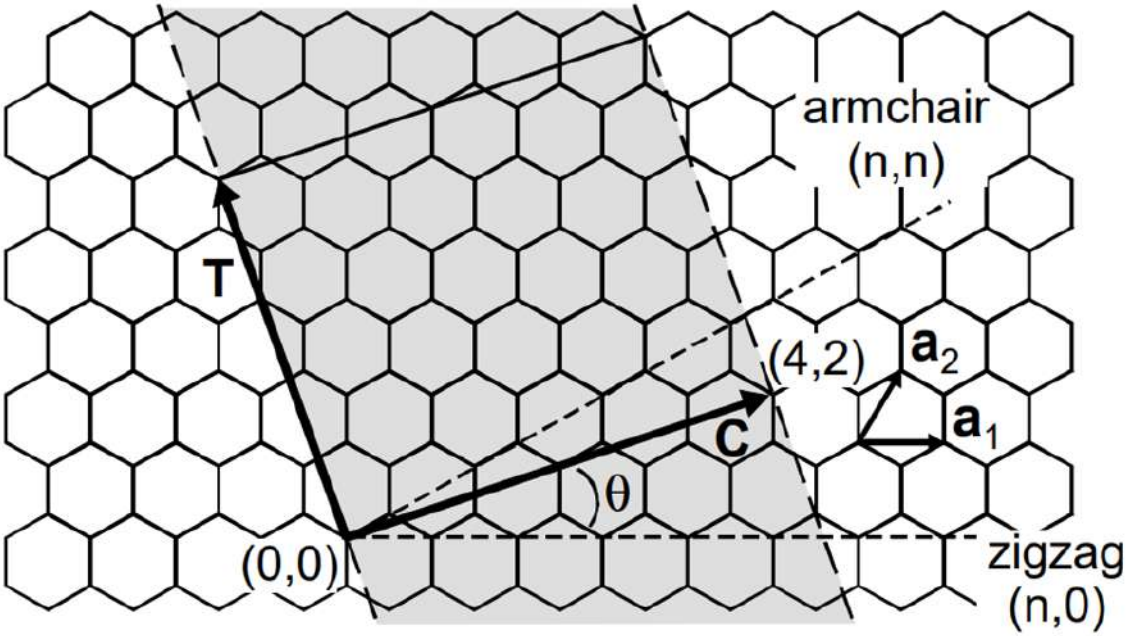

Figure 9: Starting with a graphene sheet, a carbon nanotube (CNT) is formed by wrapping the sheet so that the carbon atoms connect, creating a tube whose axis runs parallel to the vector, T. In the illustration, the grey area represents the CNT. Every nanotube can be defined by a pair of indices (n, m) that dictate its construction; here, (4,2) nanotube is used as an example. The unit vectors of the graphene lattice, labeled a_1 and a_2, are essential in this process. When the tube is formed by rolling along the dashed lines corresponding to the zigzag and armchair directions, the resulting nanotubes are non-chiral. [16]

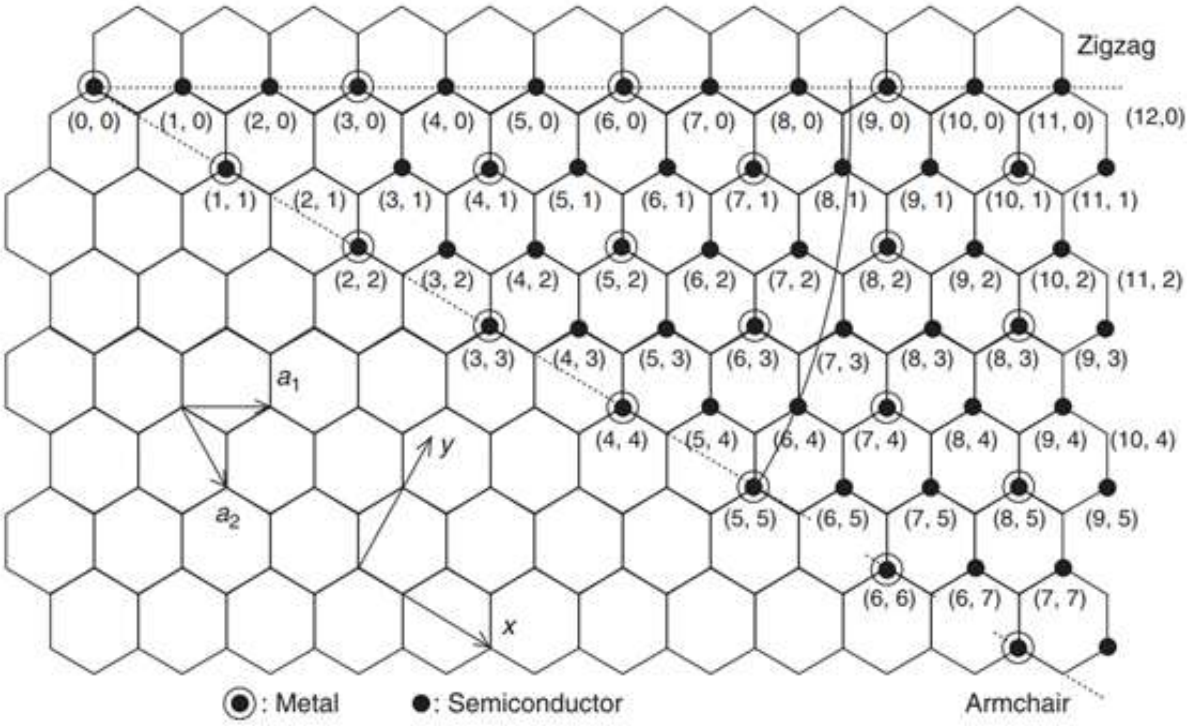

(a) Metallic or semiconducting behavior of chiral vectors

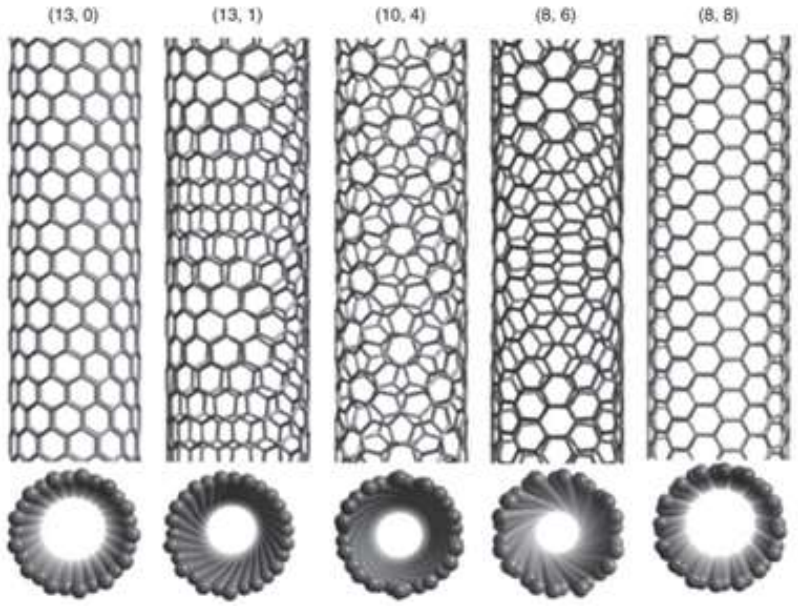

(b) Side view of chiral tubes

Figure 10: A comprehensive map is shown in (a), where many chiral vectors are listed and labeled according to the tube's electrical properties, indicating whether it is metallic or semiconducting. [17]

To comprehend how chirality influences the conductive properties of a carbon nanotube, we must first examine the electron band structure of graphene. In a graphene sheet, each carbon atom has four outer-shell electrons, three of which engage in sp^2 hybridization, forming covalent bonds with adjacent atoms through a combination of s, p_x, and p_y orbitals.

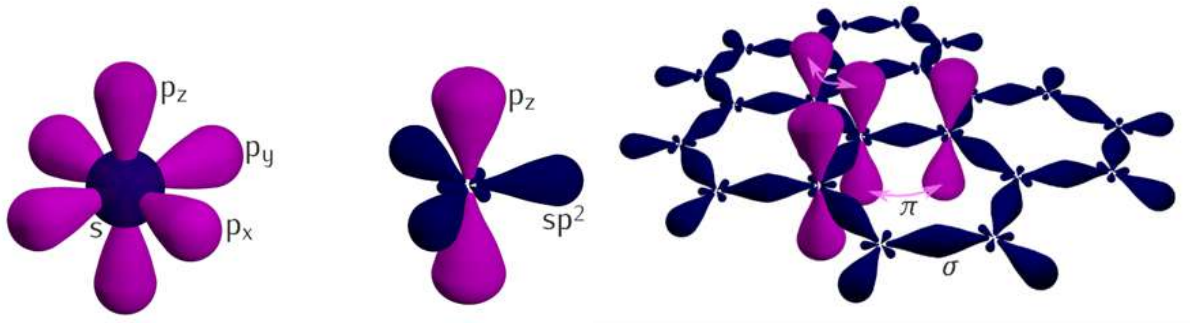

(a) 4 orbitals available for hybridization (b) Hybridized orbitals in Graphene lattice

Figure 11: σ bond is the hybridization between s orbitals and π bond is the hybridization between the s - p bonds. [18]

The remaining electron occupies a p_z orbital, which is oriented perpendicular to the graphene plane. These orbitals interact to generate two half-filled electron bands of free-moving electrons, π, which play a crucial role in graphene's remarkable electronic behavior.

Understanding this so called 'hybridization' is best possible in the context of tight binding formalism, which is a theoretical approximation performed to calculate the graphene electron bands. The idea of this calculation is to use the eigenstates of a single carbon atom to construct the hamiltonian of the graphene lattice. We then map the Hamiltonian to the vectors of each orbital of each carbon atom.

$$\hat{H}_{Tightbinding} = \sum_{m,n=\text{s and p orbitals at the positions of the atoms}} |n\rangle \langle n| \hat{H}_{Graphene} |m\rangle \langle m|$$

Important detail in this calculation is that due to the geometrical symmetry of the graphene lattice, for example 120 degrees of rotation and reflection, certain couplings of p_z to s, p_x and p_y are forbidden. Consider $\hat{R}$ as the reflection symmetry operator, with respect to the plane of graphene, which leaves graphene hamiltonian invariant. Keep also in mind that the p_z orbital is not invariant under this operation and receives a minus sign $\hat{R} |p_z\rangle = - |p_z\rangle$

$$\hat{H}_{Graphene} = \hat{R}\hat{H}_{Graphene}\hat{R}^{-1}$$

$$\langle p_z| \hat{H}_{Graphene} |s\rangle = \langle p_z| \hat{R}\hat{H}_{Graphene}\hat{R}^{-1} |s\rangle = - \langle p_z| \hat{H}_{Graphene} |s\rangle$$

Resulting expression $\langle p_z| \hat{H}_{Graphene} |s\rangle = - \langle p_z| \hat{H}_{Graphene} |s\rangle$ can only be satisfied when it is zero. Displaying the symmetry prevented coupling or hybridization of certain orbitals. Detailed analysis shows that p_z orbitals couple only to themselves, therefore the

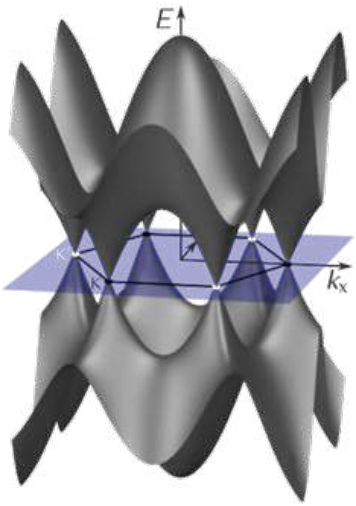

Figure 12: Plotting of graphene dispersion relation. [18]

p_z electrons, which form the π-bands, can be treated independently. Within this approximation, the dispersion relation for the energy of the electrons with wave vector k, considering only first-nearest-neighbor interactions, is given by:

$$E(k) = \pm\gamma_0 \sqrt{1 + 4\cos^2\left(\frac{ak_x}{2}\right) + 4\cos\left(\frac{ak_x}{2}\right)\cos\left(\frac{ak_y\sqrt{3}}{2}\right)}$$

In this model, the hopping energy between nearest-neighbor π-orbitals is $\gamma_0 \approx 2.8$eV, and the lattice constant is a ≈ 1.46 Angstrom. The conduction and valence bands correspond to different signs in the dispersion relation. With one p_z electron per atom, the valence band is fully occupied, while the conduction band remains vacant. As a result, the Fermi surface consists of only six discrete points. Due to this band structure, graphene is classified as a semimetal, or zero-band-gap semiconductor.

When periodic boundary conditions are applied in the circumferential direction, represented by the chiral vector C, the wave vector in that direction becomes quantized. However, the wave vector along the nanotube's axis, defined by the translational vector T, remains continuous for an infinitely long nanotube. This results in the formation of energy bands, which are one-dimensional slices of the energy dispersion relations seen in two-dimensional graphene. The allowed electronic states are those where the wave vector satisfies the condition $\vec{k} \cdot \vec{C} = 2\pi m$, meaning that the wave vector component along the circumference of the tube can only take values that are integer multiples of the tube's circumference. This simple periodic boundary condition explains how the chirality of a nanotube determines whether it behaves as a metal or a semiconductor.

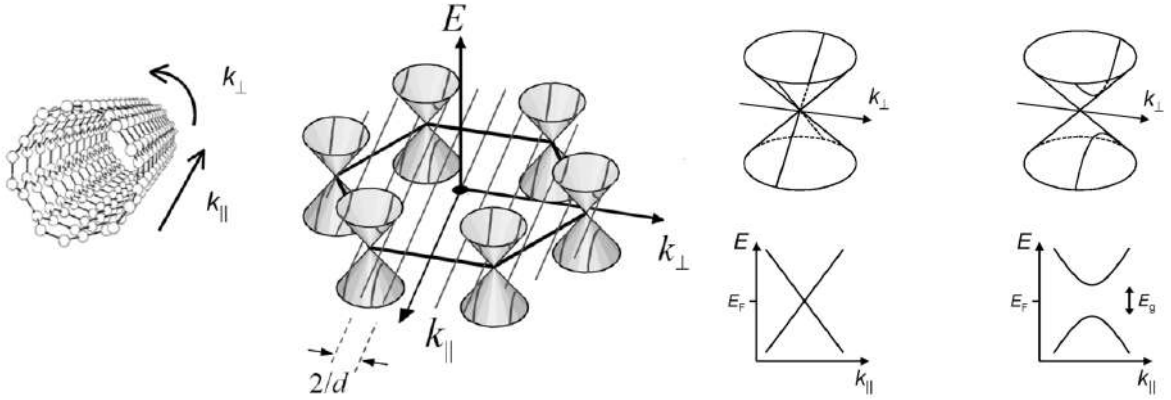

Figure 13: In picture (a), the solid lines represent the possible k values the eigenstate can have. The seperation of these lines are due to the quantization of the k vector around the circumference. In picture (b) we see how these solid lines slice the band around fermi energy level and cause a gap in the electron band, which is the essence of chirality determined conduction properties. [16]

Additionally, from the equation $\vec{k} \cdot \vec{C} = 2\pi m$, we see that any wave vector satisfying this condition also implies that the negative of the wave vector along the chirality vector will satisfy the same condition. This leads to clockwise and counterclockwise states around the nanotube. As a result, the inherent twofold degeneracy due to spin in systems with zero magnetic field is enhanced by another twofold degeneracy arising from the clockwise and counterclockwise states, resulting in fourfold degenerate states in carbon nanotubes.

Up until now, we have treated carbon nanotubes as two-dimensional graphene sheets with specific boundary conditions. However, carbon nanotubes are not simply strips of graphene—they are small cylinders, with carbon atoms placed on a curved surface. There are two key reasons why we should expect the curvature of the nanotube wall to affect its electronic properties. First, when a graphene strip is rolled into a cylinder, the distance between carbon atoms with different azimuthal angles is reduced. This effect is most noticeable for two atoms that are directly opposite each other on the wall (i.e., when the azimuthal angle is 180°). In the nanotube, their distance is d, while in the unrolled sheet, it is $\frac{d}{2}$. For two neighboring carbon atoms, the bond length along the circumference becomes smaller in the nanotube, though the change is minimal for typical nanotube diameters. Second, rolling the graphene sheet introduces changes in the angles of the hexagons. In the tight-binding model used to derive the electronic band structure of graphene, we relied on the equivalence of neighboring atoms at a given order. This assumption no longer holds when curvature is included. In addition to these geometric considerations, there are quantum-mechanical and symmetry arguments. In flat graphene, the p_z orbitals are strictly perpendicular to the plane, while other orbitals lie in the plane, meaning they cannot mix. However, on the curved surface of a nanotube, the p_z and the remaining orbitals can interact and form hybridized states that exhibit both sp^2 and sp^3 character. In fact, when the curvature of small-diameter tubes induces s-p hybridization, the expected metallic behavior alters into that of a narrow-bandgap semiconductor.Still the crude approximation of nanotubes as a graphene sheet with special boundary conditions is a well estimate.

2.2.1 Straining Effects On Carbon Nanotubes

Straining of carbon nanotubes, specifically uniaxially straining, is in previous works done mostly with AFM tips [9], [19]. This method introduces, effects such as local distortion of sp2 bonding where the nanotube is contacted with AFM tip [9] and large strain build-up at the point of contact [20], such that the nanotube breaks always at that point. Straining nanotubes using a comb actuator will not therefore have a large local strain nor disrupting local sp2 bonds.

Calculations using tight-binding and local-density approximation methods predicted that tubes should elongate elastically up to a critical strain that depends on the radius and chirality of the tube, and for larger strains, the introduction of topological defects, such as bond rotations, becomes energetically favorable. [20].

In the elastic regime of straining, typically no scattering centers are introduced. Only after a critical elongation the new scattering centers, which are defects, appears. This can be detected by the electrical conduction measurements. One theoretical work shows that straining causes CNT's to break their uniform bonding pattern and create double pentagon-heptagon defect pairs [21].They show that these defects are energetically preferred for uniformly stretched nanotubes after certain strain percentage. Formation of this defect also initiates plastic deformation and further disruptions to ideal graphite network build on these initial formations.

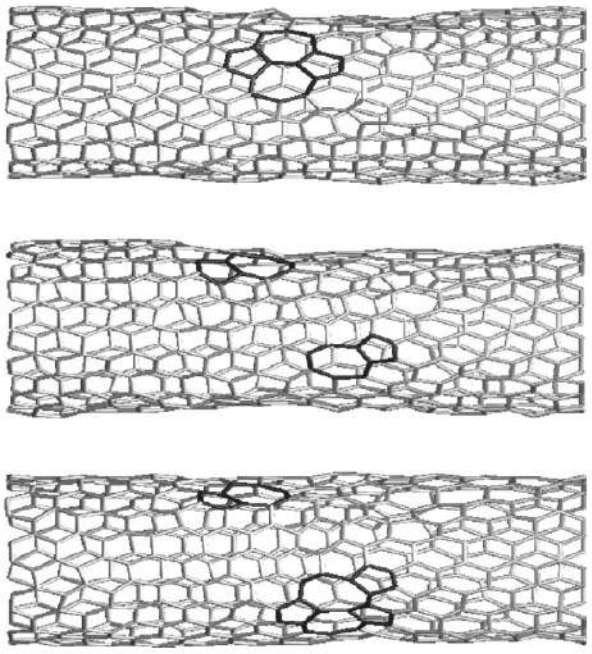

Figure 14: Simulation of a strained carbon nanotube. From top to bottom, the creation of a defect center, its diffusion and formation of further defects can be seen. [21]

It has also been shown that a carbon nanotube under uniaxial stress can change its metallic behavior. [22] In this work, a tight binding formulation is performed with revised transfer integral between atoms along the stress axis using the formula $t_{\alpha\beta} = t^{(0)}_{\alpha\beta}(\frac{d_0}{d})^2$, where d_0 is carbon π bond length before deformation and d is bond length after deformation, due to Harrison [23]. It is found that for zigzag tubules (n,0) the gap varies linearly with stress and independently of diameter: $\frac{dE}{d\sigma} = 10.7$ meV/GPa for σ <10 GPa.

Furthermore, upon applying stress, a semiconductor to metal transition is predicted and the armchair tubules remain metallic under all conditions studied.

2.2.2 Carbon Nanotubes As Quantum Dots

The quantum dot behavior of nanotubes emerge from the fact that these structures can have diameters on the order of couple nanometers and length varying from nanometers to micrometers. Due to the their small size, especially the size of diameter, the allowed k vectors around the circumference divide the energy spectrum into incremented 1 dimensional electron bands. Consider a zigzag nanotube with a diameter of 5nm which has $2\pi 5\text{nm} = 30\text{nm}$ circumference. Dividing this with the spacing between atoms around the circumference, which is $a\sqrt{3} \approx 2.4$ Angstrom approximately gives 125 atoms. This sets the chirality vector (125,0) and the equation $\vec{k} \cdot \vec{C} = 2\pi m$ gives us k = $\frac{2\pi m}{125}$. This tells us that the k vector will divide the energy spectrum into 125 segments. If we assume that the energy increases linearly from the band bottom 3·-2.8 eV to the fermi level which is zero, then the energy spacing of these 1 dimensional bands will be roughly $\frac{8.4eV}{125} = 67$ meV. If we instead consider a sphere of diameter 5nm, charging this sphere with electrons will cost us $\frac{Q^2}{2C} = \frac{e^2N^2}{2C}$, taking capacitance of sphere from classical considerations C = $4\pi\epsilon_0$R and N being the integer number denoting amount of electrons, gives us 795 meV to fill this sphere with 10 electrons. The filling of fermi levels in crystal structures is usually done by assuming non interacting electrons so that the eigenstates of the crystal don't change with each added electron. However this becomes a bad approximation when we start considering nanostructures, where the energy stored between electron-electron interactions exceeds the non-interacting hamiltonian's energy spacings, as it was seen in the Helium atom.

The motivation in using carbon nanotubes as quantum dots stems from couple of advantages. Carbon nanotubes can be ultra clean compared to semiconductor structures and can be grown to centimeters, due to their nano size diameters they are a one dimensinal system. The abitily to functionalize them with external organic molecules opens furthermore possibilites of creating advanced quantum dot systems [24].

So far, research has primarily focused on utilizing these properties in zero-dimensional single and double quantum dot systems. However, extending this to longer one-dimensional systems has been challenging due to disorder, which causes the electron system to break into localized, uncontrolled quantum dots at low temperatures. [25] The phenomenon responsible for this behavior is known as Anderson localization, which posits that in one-dimensional systems with random barriers, such as disordered semiconductors, the ability of electrons to tunnel through these barriers is exponentially suppressed, leading to insulating behavior. However, due to the ultra-clean nature of carbon nanotubes, disorder-induced exponential localization in one dimension is no longer a concern. Furthermore, researchers have demonstrated the creation of localized quantum dots along carbon nanotubes [26], demonstrating the ability of locally tuning the electrons on one dimension.

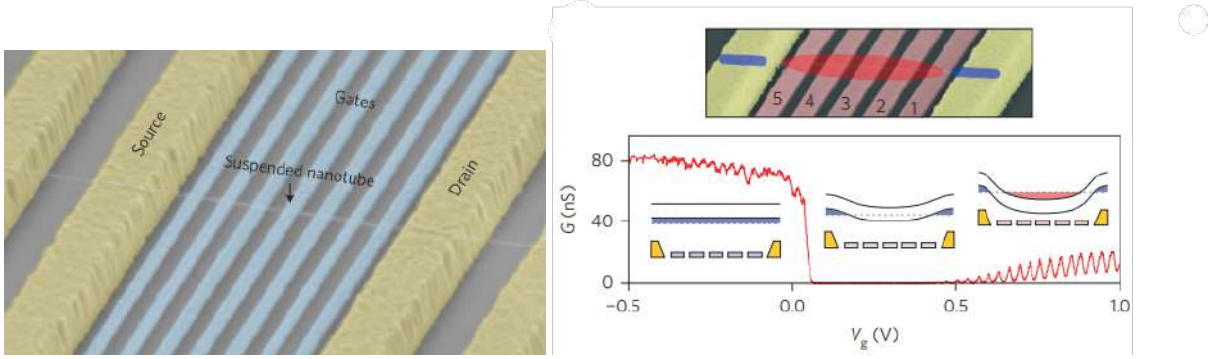

(a) (b)

Figure 15: In picture (b), The conductance, G, is measured as a function of the common gate voltage, V_g, applied to all five gates. Coulomb oscillations are observed at positive gate voltages, indicating the formation of a quantum dot that extends over the entire suspended nanotube. Insets show position-dependent nanotube band diagrams in the three distinct conductance regimes: a hole-doped 'nanotube wire', the nanotube bandgap, and electron Coulomb oscillations. [26]

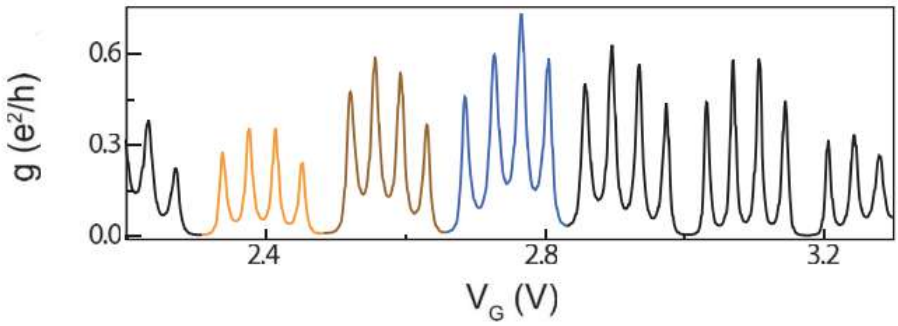

Figure 16: Conductance measurement of single carbon nanotube at low temperatures. The colored peaks indicate the 4 fold degenerate states of the non-interacting hamiltonian, where it is now seperated due to the required charging energy stored between electrons. [27]

2.2.3 Device - Carbon Nanotube Contact

A deep comprehension of the straining device also necessitates a solid grasp of the physical interactions occurring at the interface between the metal and the carbon nanotube. This interface plays a crucial role in the behavior and performance of Carbon Nanotube Field Effect Transistors (CNFETs). Thanks to their remarkable electrical properties—such as quasi-ballistic transport and high carrier mobility even under diffusive conditions—CNFETs have achieved performance levels that rival modern silicon-based MOSFETs. As a result, determining the optimal combination of nanotube diameter and metal type that ensures consistent and high-performing CNFET behavior is a key objective.

When a metal comes into contact with a semiconductor, an energy barrier—commonly known as a Schottky barrier—naturally forms at the interface. The magnitude of this barrier is determined by the relative positioning of the metal's Fermi level with respect

to the conduction and valence bands of the semiconductor. In the case of semiconducting carbon nanotubes (CNTs), this phenomenon is no exception; a potential barrier typically forms at the metal-CNT junction when the nanotubes are integrated onto a chip.

Studies such as [28] have demonstrated the presence of Schottky barriers at these interfaces. By fabricating CNT junctions using different metals like Palladium (Pd), Titanium (Ti), and Aluminum (Al), researchers confirmed that the barrier height is influenced by the electronic alignment at the contact point—consistent with classical Schottky behavior. Furthermore, experiments with nanotubes of varying diameters revealed that in the case of a Pd-CNT interface, no barrier was observed when the nanotube had a diameter of approximately 1.7 nm, indicating a unique electronic compatibility at this specific scale.

2.3 Physics of MEMS Comb Actuator

2.3.1 Comb Actuator

MEMS actuators are a specialized category of MEMS devices designed to transform energy into motion. This energy conversion can occur through physical or chemical mechanisms. The resulting motion enables various functions, including precise positioning, valve actuation, energy conversion analysis, switching operations, and material characterization at the micro- and nanoscale [29].The operation of microvalves, including their opening and closing, plays a crucial role in microfluidics and lab-on-a-chip technologies.

The comb actuators function based on interdigitated comb-like structures, where an applied voltage creates an electrostatic force between fixed and movable electrodes, leading to controlled displacement. Their design enables precise motion control with low power consumption, making them ideal for applications in micro-optics, RF MEMS, biomedical devices, and micropositioning systems. The simplicity of their fabrication, compatibility with semiconductor processes, and scalability further contribute to their extensive use in modern microsystems.

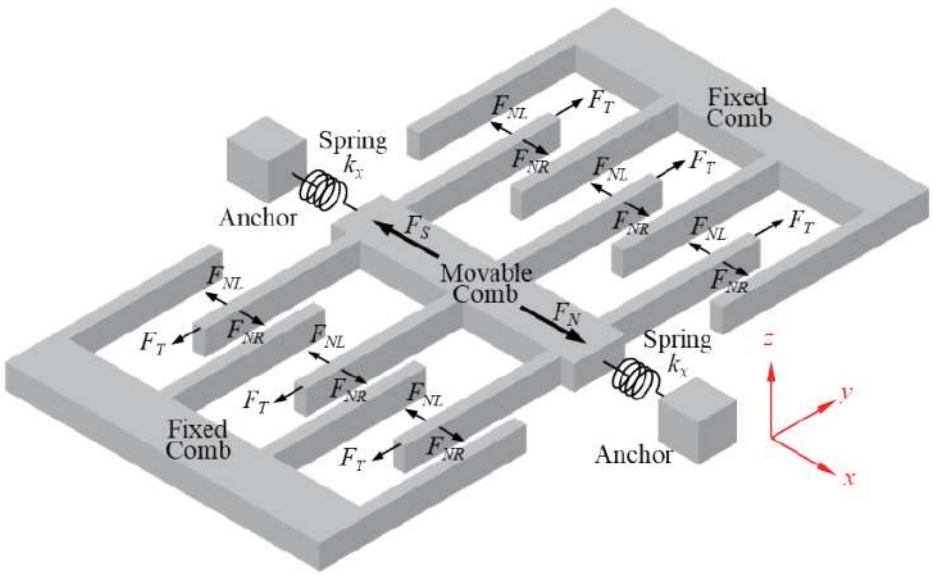

Figure 17: A schematic drawing of a typical comb actuator. [30]

2.3.2 Comb Capacitors

A widely used approach for generating force in MEMS actuators involves utilizing capacitive structures. Among the most common designs are parallel plate and comb capacitors. Parallel plate configurations, in particular, exhibit capacitance defined by the equation:

$$C = \frac{\epsilon_0 A}{d}$$

where ϵ_0 is permittivity of the material in between the plates, A is the area of the plate and d is distance between plates. The electrostatic energy is therefore $E = \frac{CV^2}{2}$ which if we differentiate by d after plugging in to the previous formula, we get

$$Force = -\frac{\epsilon_0 A V^2}{2d^2}$$

Hence it is seen that we gain a lot by fabricating combs with fingers very close to each other. However also note that when the voltage is applied and comb starts to move, $1/d^2$ factor also changes, which complicates the behavior of displacement from simple quadratic V^2 to a rather involved formula. To derive this consider a finger of the comb to have distance a to the finger on its left and b to its right. This can figuratively be seen from the figure and is needed in order to create a directionally unbalanced force which should pull the comb to desired direction. Assuming that the comb is connected to a linear spring with spring constant k and b is smaller than a so that the comb is pulled towards shrinking b, thus we have with amount of combs M,

$$M * (F_{pulltotheleft} + F_{pulltotheright}) + F_{spring} = 0$$

$$M * (-\frac{\epsilon_0 A V^2}{2(a+x)^2} + \frac{\epsilon_0 A V^2}{2(b-x)^2}) - kx = 0$$

$$V = \sqrt{\frac{2kx}{M\epsilon_0 A}(\frac{-1}{(a+x)^2} + \frac{1}{(b-x)^2})^{-1}}$$

This equation gives us the amount of voltage needed to set net force to zero at position x. Important thing to notice now is that the solutions of this does not mean they are also the points of equilibrium position. To understand this consider the figure below.

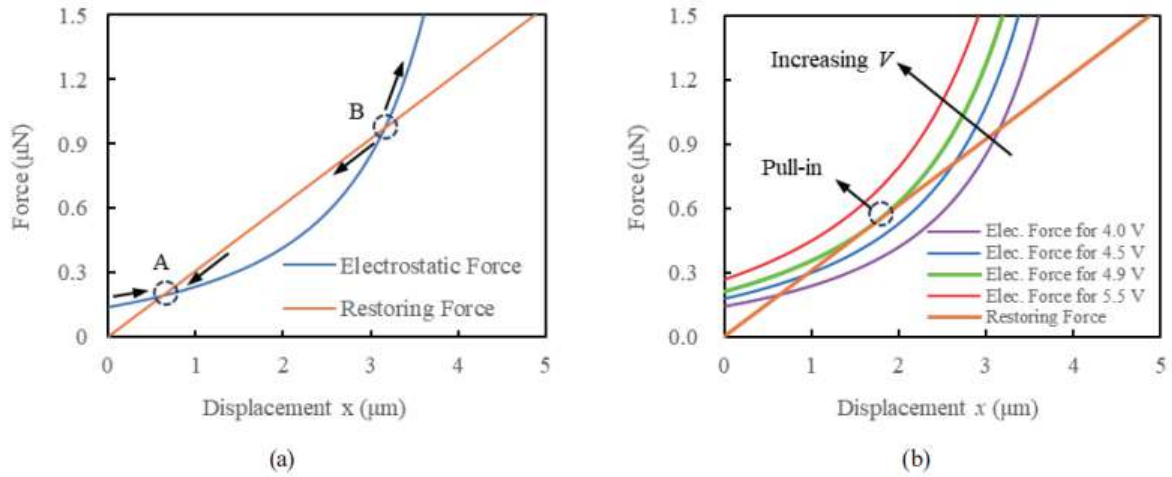

Figure 18: a) Electrostatic versus Spring restoring force plot. When a voltage is applied, the comb begins moving along the positive x-axis because the electrostatic force exceeds the restoring force of the spring. It comes to rest at point A, where the forces reach equilibrium. Even with minor disturbances, the system remains stable and does not deviate significantly. However if the system begins at position B, any slight disturbance to the position will yield a stronger pull towards higher or lower x due to force imbalance. Thus system will either diverge or approach A. b) Here the plot of effect of increasing voltage on electrostatic force can be seen. As the voltage increases, the points that intersect approach each other and at a certain threshold voltage there is not any force balance point. In that case the comb is pulled towards the electrode until it crashes or stopped by an auxiliary structure. This is called pull-in phenomenon. [30]

Hence we see that there exists a certain voltage threshold, after which the comb gets pulled as much as it can. We therefore also a need a way to calculate the pull-in voltage for a given design.

The way to find this is to note that the in the above figure on pane b), the electrostatic force and restoring force has the same slope at the point of contact. Therefore equating the derivatives with respect to x there gives us a formula.

$$\frac{\partial F_{electrosatic}}{\partial x} = -\frac{\partial F_{restoring}}{\partial x}$$

The minus sign is due to align the forces direction so that it appears as in pane a).

$$M\epsilon_0 AV^2\left(\frac{1}{(a+x)^3} + \frac{1}{(b-x)^3}\right) - k = 0$$

Plugging in the V from the equation of forces formula above

$$2x\left(\frac{-1}{(a+x)^2} + \frac{1}{(b-x)^2}\right)^{-1}\left(\frac{1}{(a+x)^3} + \frac{1}{(b-x)^3}\right) - 1 = 0$$

The solution, interestingly enough, is not dependent on the spring constant and is only dependent on the comb gaps. Approximate solution while b = 700nm and a = 1200nm gives us a pull in position $x_{pullin} = 207$ nm.

2.3.3 Comb Springs

The common types of spring designs are clamped-clamped beams, crab-leg flexure and folded-beam flexure. In our design we use folded flexure beam.

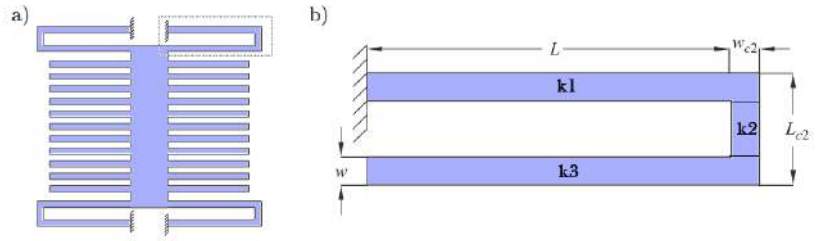

Figure 19: a) shows top view of a comb actuator. b) is the folded flexure beam structure. [31]

As it can be seen at the pane b) in the figure above, the spring can be divided into 3 components whose stiffness constants are k_1, k_2 and k_3. Upon application of a force, the components k_1 and k_3 flex and the k_2 elongate. Therefore the system can be thought of 3 springs connected in series. In that case the net constant is given as

$$\frac{1}{k} = \frac{1}{k_1} + \frac{1}{k_2} + \frac{1}{k_3}$$

The maximum displacements for the components k_1 and k_3 are caused by shear and bending.

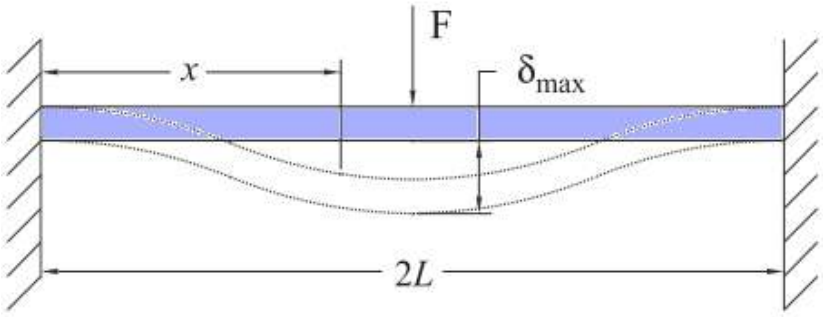

Figure 20: The flexing motion of the spring k_1 and k_3 can assumed to be as shown in the picture. [31]

For this movement the spring constant is given as

$$k = \frac{24EI}{L^3}$$

where the I is second moment of cross sectional area. In the case of a rectangle of width w, which is perpendicular to the beams direction of motion, and thickness t we have

$$k = \frac{12Ewt^3}{3L^3}$$

taking into account the k we are considering is for the half of the structure in above figure, thus an extra 1/2.

Hence k_1 and k_3, the stiffness due to bending, is given as [32]

$$k_{bending} = \frac{4Ewt^3}{L^3}$$

where E is Young's modulus, L is lenght. The stiffness due to shear of components 1 and 3 is given as [32]

$$k_{shear} = \frac{5wtG}{3L}$$

where w is width, t is thickness and G is shear modulus. Therefore,

$$\frac{1}{k_1} = \frac{1}{k_3} = \frac{1}{k_{bending}} + \frac{1}{k_{shear}}$$

The stiffness of the second component can be assumed to have only elongation component due to strain. Therefore

$$k_2 = \frac{Ewt}{L_2}$$

.

By using $G = \frac{E(1+\mu)}{2}$ and taking into account the 4 springs connected to the mass, where μ is Poisson's ratio, total spring constant then can be found to be

$$\frac{1}{k_{onespring}} = (2 \cdot (\frac{L^3}{4Ewt^3} + \frac{3L}{5wtG}) + \frac{L_2}{Ewt})$$

as mentioned by [33]. Considering that we have 4 of these springs, $k_{Total} = 4k_{onespring}$.

This way of adding up the spring constants is in Structural mechanics is called superposition method and is generally valid for small deflections within linear regime. Since in our comb actuator structure we are aiming for nanometer range deflections this assumption is reasonable. Since the spring constants of bending and shear are added in series, neglecting shear effects as it is much stiffer than bending is plausible. We then arrive at a simpler formula

$$k_{Total} = 4 \cdot \frac{2Ewt^3}{L^3}$$

3 Chapter 3 - Experimental Methods

3.1 MEMS Simulation with COMSOL Multiphysics

3.1.1 Comb Actuator Displacement Behavior

To analyze the displacement of the comb actuator, a simulation was conducted to observe its response to applied voltage. In the simulation model, red regions indicate areas of high displacement, while purple regions represent stationary parts. A closer inspection of the comb's spring structures reveals noticeable bending in the anchoring springs. The displacement exhibits nonlinear behavior because the electrostatic pulling force acting on the combs depends not only on the square of the applied voltage but also on the extent of the displacement itself, as discussed in Section 2.4.2.

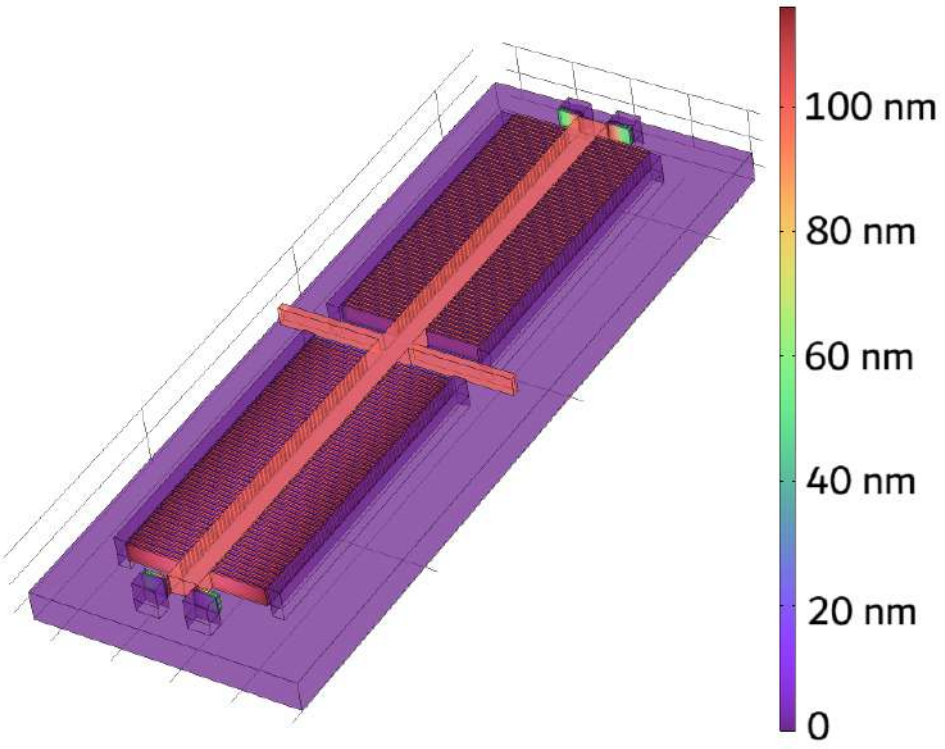

(a)

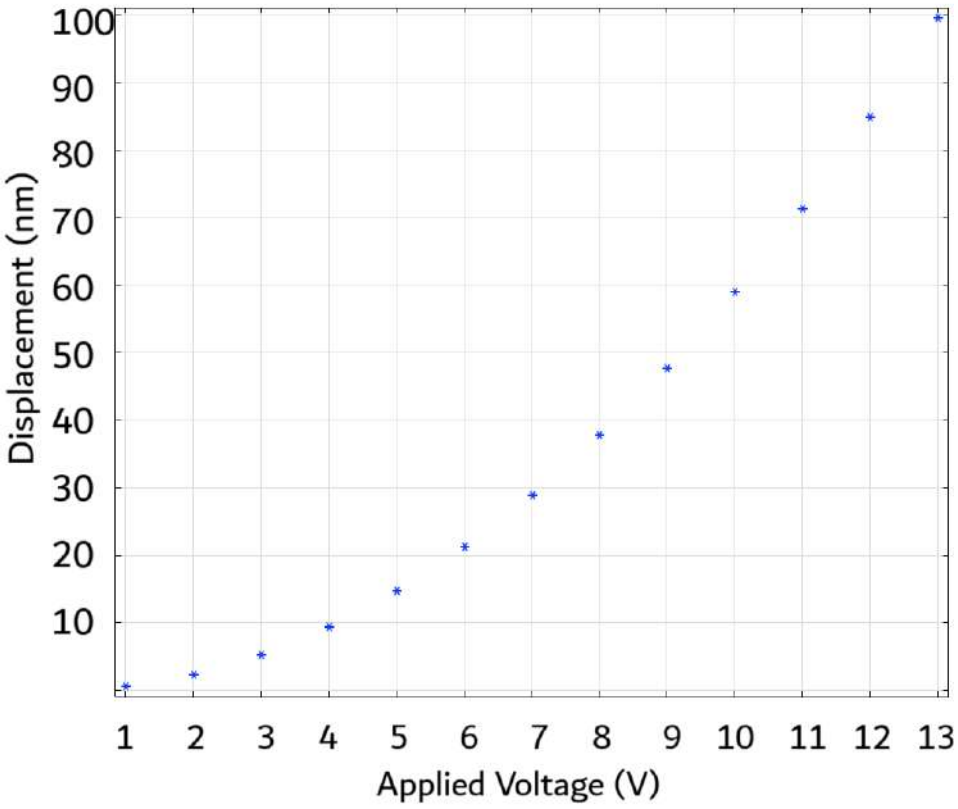

(b)

Figure 21: a) Comb model with applied voltage at 13 volts. b) Voltage - Comb displacement sweep simulation.

Figure a) shows the detailed model of the device. The red region represents the actuated component, which is suspended in air and supported by springs connected to fixed blocks at both ends of the actuator. These blocks, along with the electrode combs, are anchored to the handle layer via a silicon oxide layer and therefore remain stationary. Although the tips of the electrode actuators also experience slight bending, it is only on the order of a few nanometers and not visible in the figure. The simulation indicates that the combs can achieve a displacement of up to 100nm. Assuming the device is designed to suspend a 1µm section of a nanotube, a 100nm displacement corresponds to a 10% strain, approximately the maximum strain the nanotube can withstand.

In this simulation, the device layer consists of silicon, with a silicon oxide layer beneath it, and a silicon handle layer at the bottom. The electrical conductivity of silicon is set to $0.02\Omega\cdot$cm, based on the specifications provided in the silicon wafer datasheet. Young's modulus is defined as 170 GPa, and the relative permittivity is set to 10^9 to approximate conductive behavior. In the Solid Mechanics module, the only Fixed Constraint is applied to the surface of the handle layer. All materials are modeled as linear elastic and isotropic. For all other material properties, COMSOL's default values are used.

3.1.2 Evaluation Using The Parallel Plate Approximation

To evaluate whether the parallel plate approximation is reasonable, a parametric sweep is performed over the area of the comb faces that oppose each other and form the effective parallel plates. In this sweep, both the device thickness and the comb length are varied. In this approximation, the facing surfaces of the combs are modeled as forming a parallel plate capacitor, completely neglecting fringing fields. The effective area of these surfaces is given by the product of the comb length and thickness. To evaluate whether the capacitance indeed scales linearly with both parameters, a series of sweep simulations is performed.

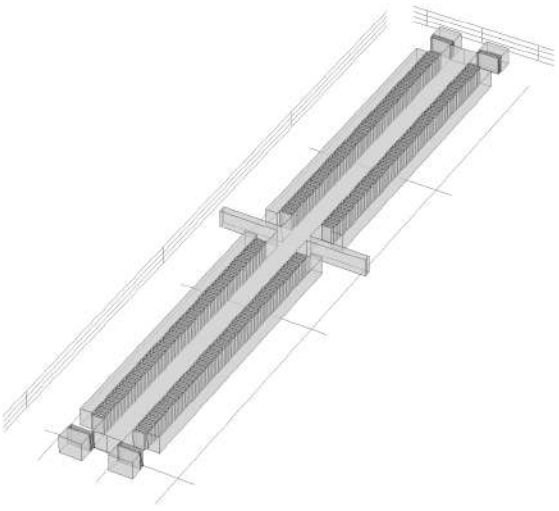

(a) Comb length 10 um

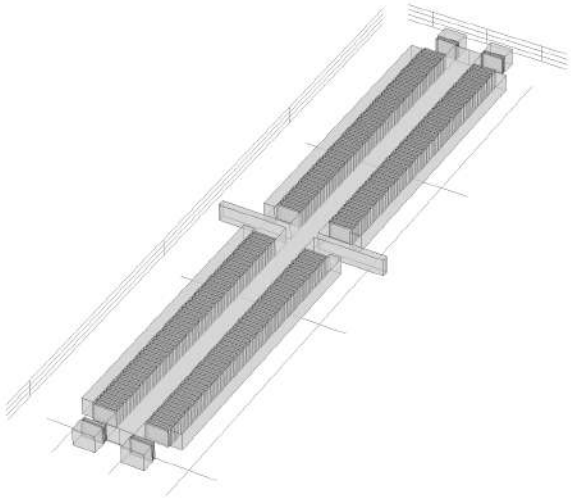

(b) Comb length 20 um

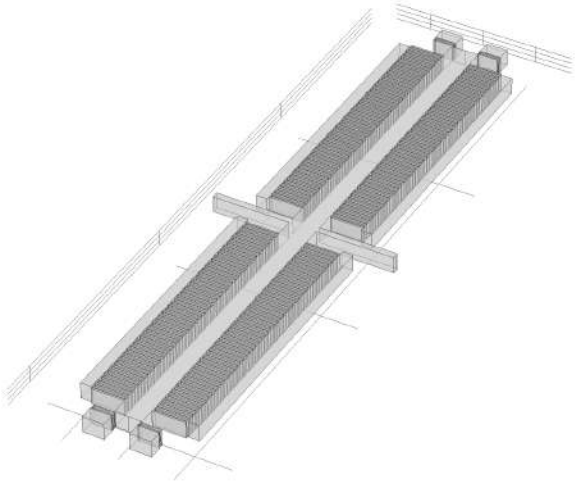

(c) Comb length 30 um

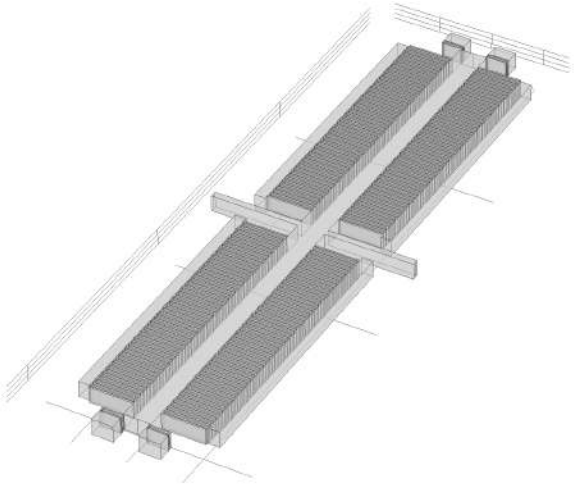

(d) Comb length 40 um

Figure 22: Four representative cases from the comb length sweep simulation.

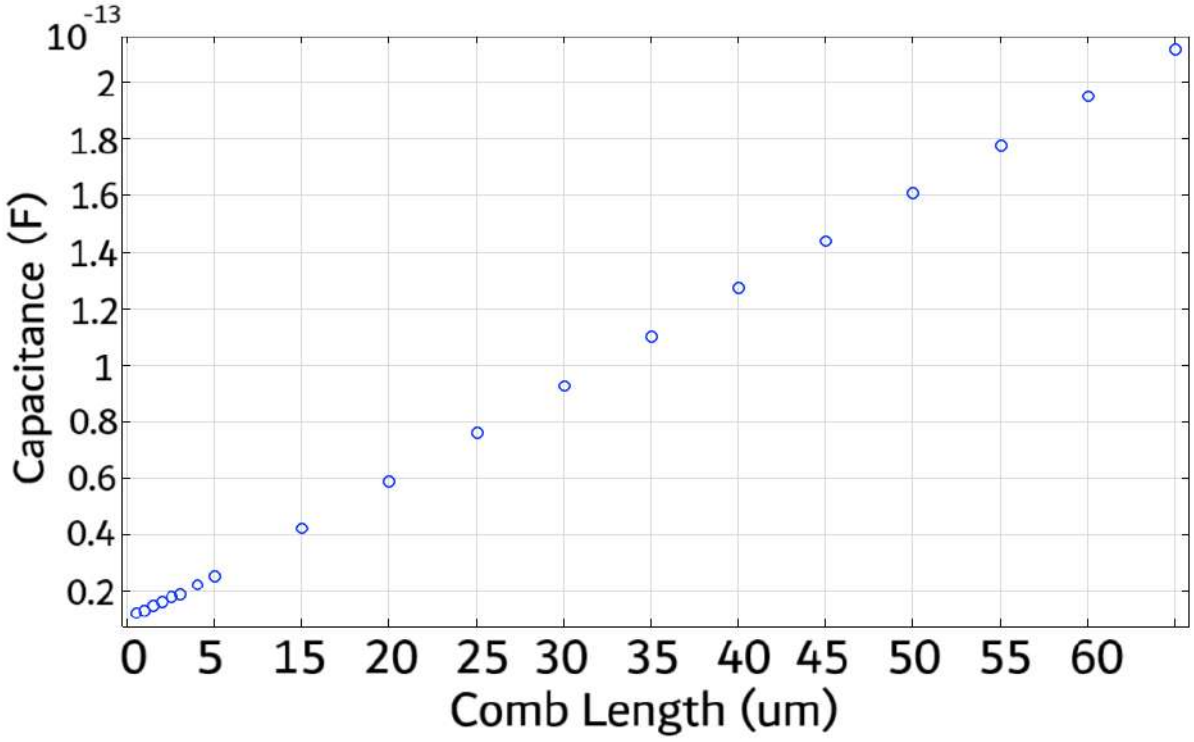

(a) Capacitance (10^{-13}F) - Comb Length (um) simulation. The higher density of points at shorter comb lengths results from the specific simulation parameters we selected.

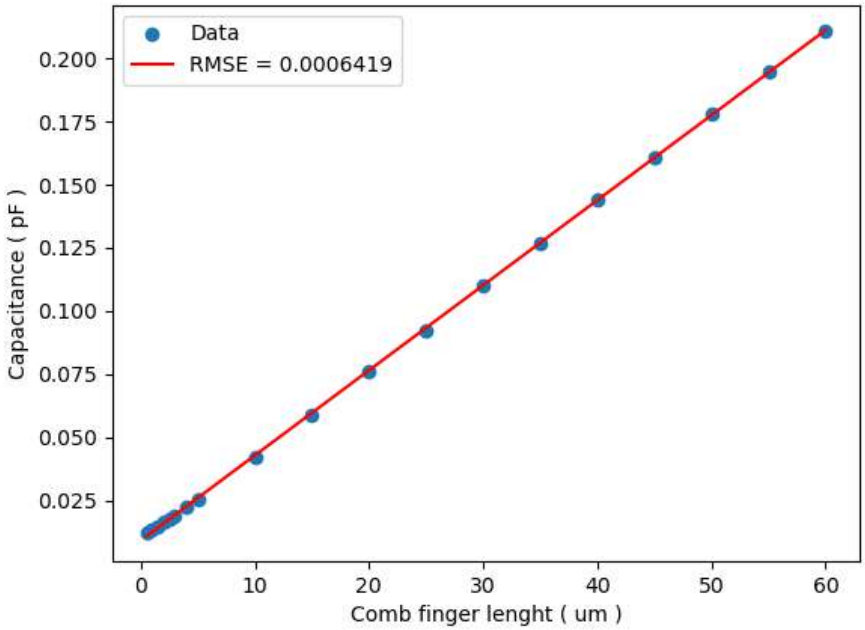

(b) Linear function fit to Capacitance (pF) - Comb Length (um) simulation

Figure 23

It is clearly seen that the capacitance of the comb actuator model increases linearly with comb length of the structure.

This result is supportive of the relation $Capacitance \propto Comblength$.

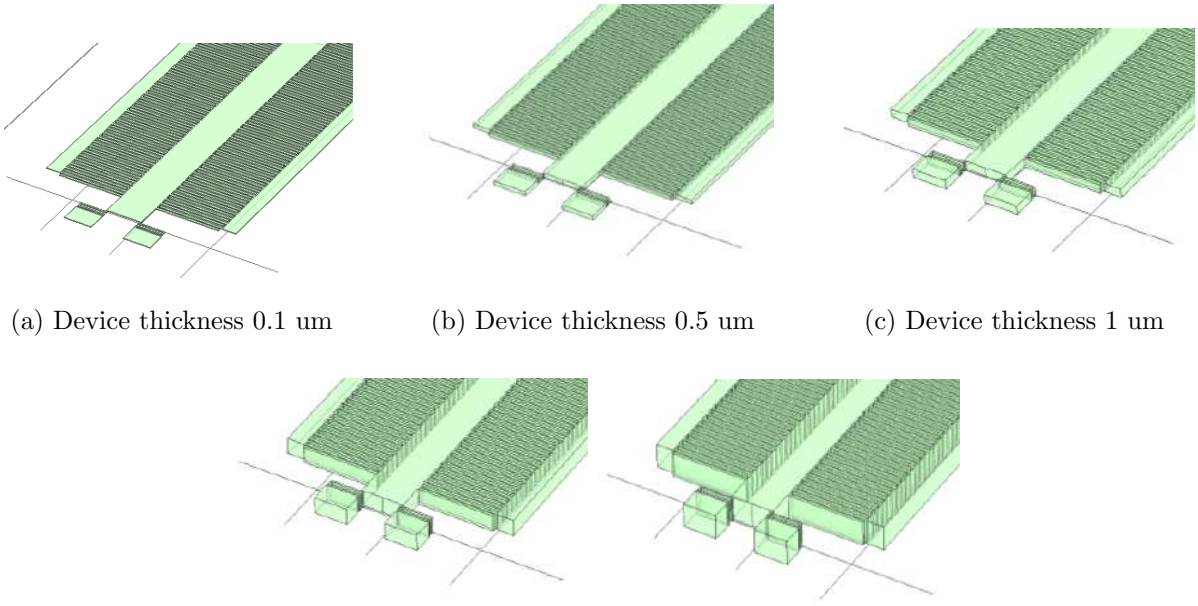

(a) Device thickness 0.1 um (b) Device thickness 0.5 um (c) Device thickness 1 um

(d) Device thickness 2 um (e) Device thickness 3 um

Figure 24: Five examples from Capacitance – Device Thickness Simulation. In these images, the z-axis (representing device thickness) is exaggerated by a factor of five for better visualization.

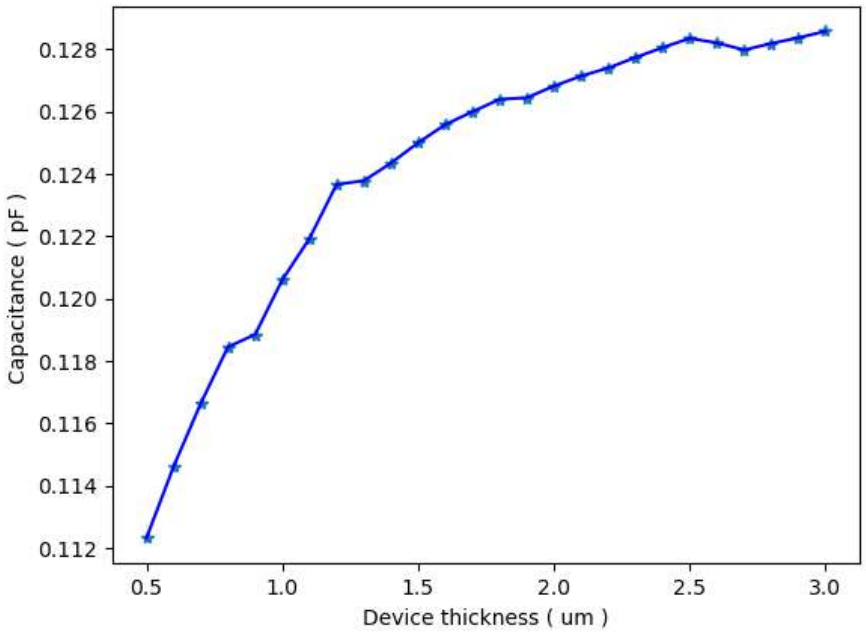

Figure 25: Plot of Device Thickness (um)- Capacitance (pF) simulation

It is seen in this plot that device thickness nonlinearly increases the capacitance. This solely renders the formulation Capacitance $\propto$ Comb lenght $\cdot$ Comb Thickness inaccurate.

Simulating comb length and device thickness independently, while keeping the other parameter constant—only reveals their behavior at specific fixed values, resulting in just two lines within the three-dimensional parameter space of comb length, device thickness, and capacitance. To capture the full dependence of capacitance on both variables simultaneously, a 2D sweep over a range of comb length and device thickness values is performed. If both parameters influence capacitance linearly, the resulting data in 3D space should form a flat plane.

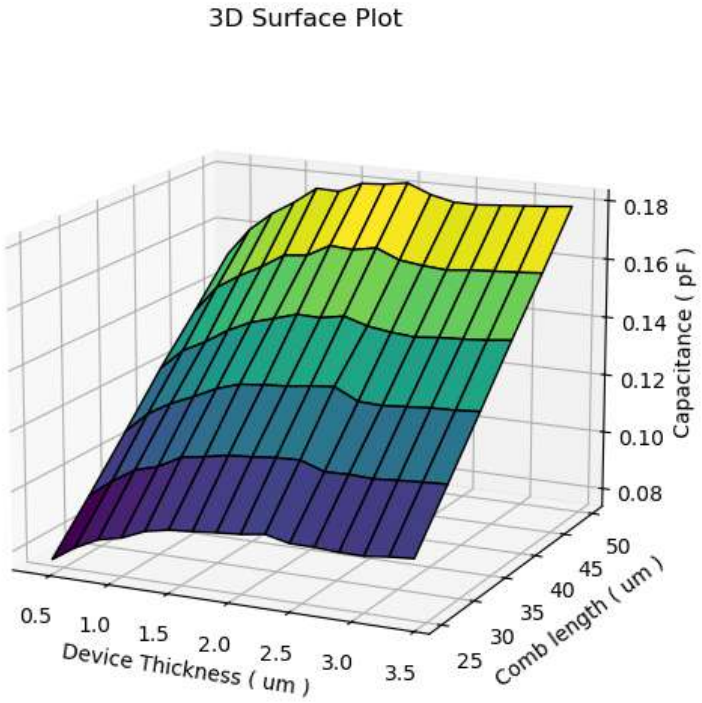

Figure 26: Simulation of capacitance while sweeping Comb length (um) and Device thickness (um).

The increase in capacitance with comb length remains linear across all values of device thickness. A similar trend is observed for device thickness; however, the capacitance retains a nonlinear relationship with it. This indicates that the parallel plate capacitor approximation is not particularly accurate due to the influence of thickness, while the comb length behaves in line with the linear assumption.

3.1.3 Spring Design

In order to assist our understanding of how folded beam flexure spring works, separate simulation on the spring is performed. We have built a separate model for the spring with same device dimensions. After applying a Fixed Boundary Condition to the face of the spring where it is attached to the anchor, a Definite Displacement is applied to the opposite face, where the spring connects to the comb actuator.

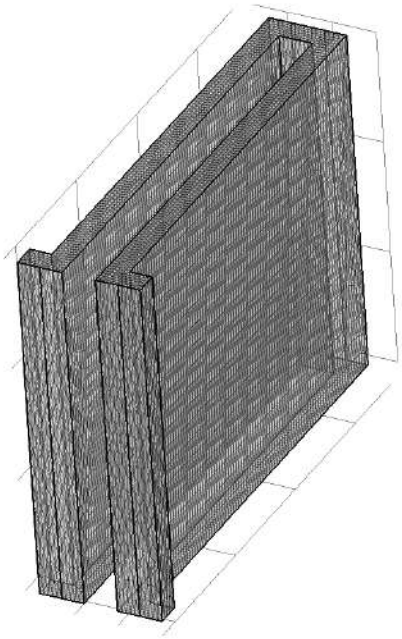

(a) Spring model with Extremely Fine mesh

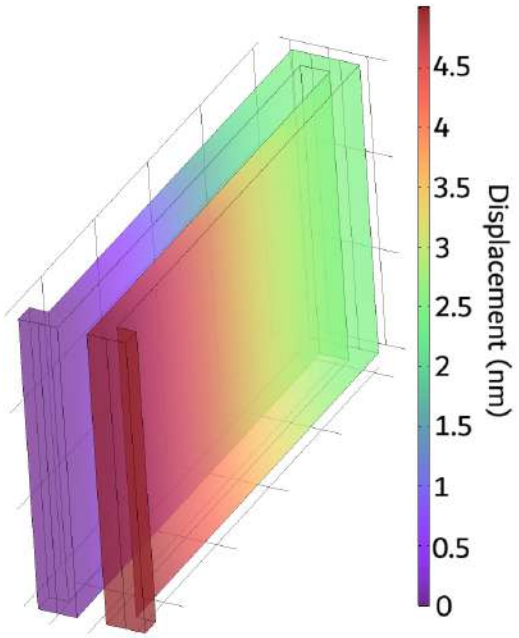

(b) Image of the bent spring.

Figure 27: Spring model before and after displacement. In these figures, the z-dimension is scaled by a factor of five for better visualization.

To evaluate whether the spring behaves linearly within the target strain range, on the order of tens of nanometers, a prescribed displacement sweep from -50nm to +50nm is applied. After each solution converges, the resulting reactive force is calculated and divided by the corresponding displacement to assess the spring's stiffness and linearity. The spring constants calculated at each displacement are plotted in the figure below.

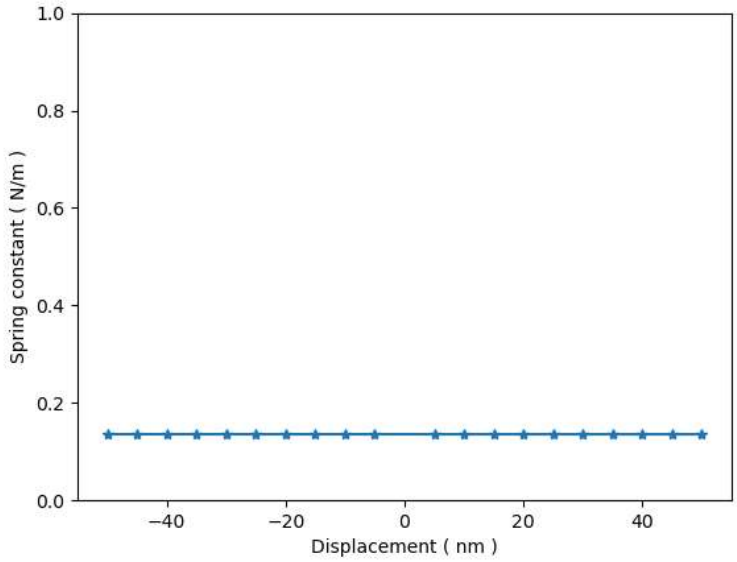

(c)

Figure 28: Plot of simulated Spring Constant (N/m) - Displacement (nm).

Based on the calculations, each spring in the actuator should have a spring constant of approximately 0.17 N/m, considering that the device includes four springs. The flat profile of the spring constant across the displacement range further confirms that the spring operates within its linear regime.

3.1.4 Natural Frequencies of the Model

Simulation of the device's eigenfrequencies provides insight into its oscillation modes and resonance frequencies. This information is critical for refining the design to ensure the structure is resistant to environmental acoustic disturbances or other oscillations. One key design goal is to maximize the lowest mode frequency, as resonance frequencies within the audible range (20 to 20,000 Hz) are susceptible to environmental noise that can cause device malfunction or damage.

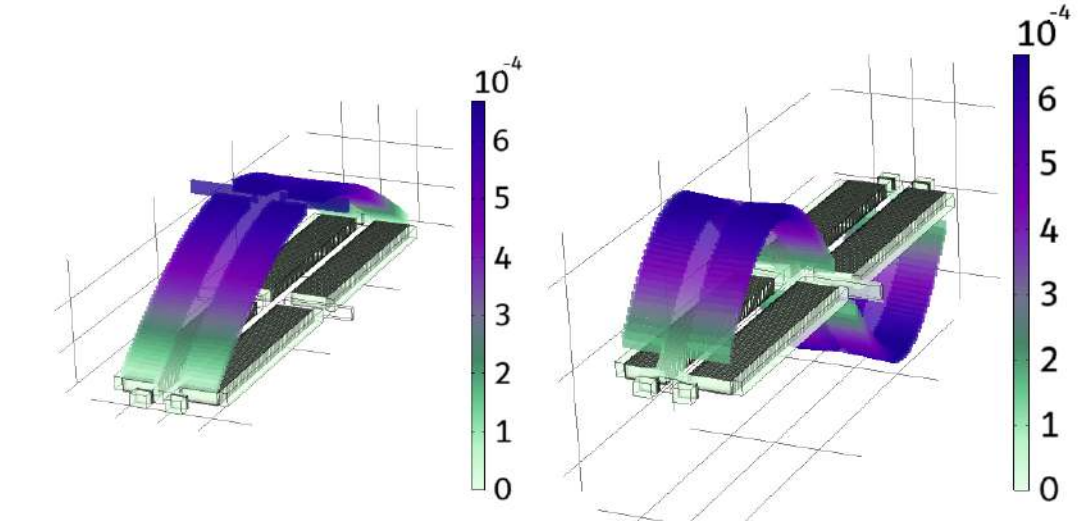

(a) 1st mode of resonance of the device at 26,259 Hz

(b) 2nd mode of resonance of the device at 100,140 Hz

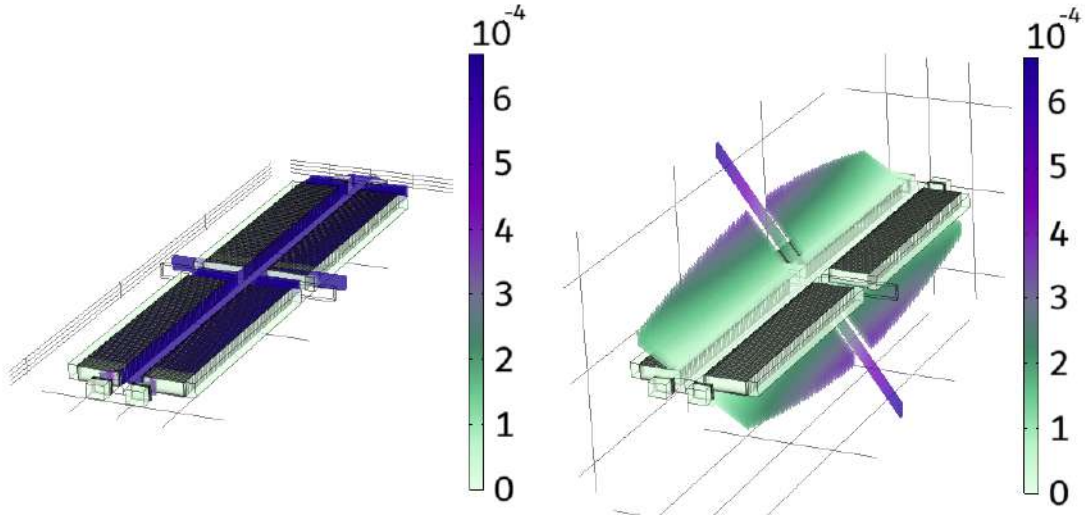

(c) 3rd mode of resonance of the device at 126,960 Hz

(d) 4th mode of resonance of the device at 128,140 Hz

Figure 29: Eigenmodes of the actuator. Colorbar indicates displacement given in m.

A lowest eigenfrequency of 26,000 Hz is sufficiently high to withstand typical environmental noise. This allows the chip to be handled and transported with confidence, without the need for special sound isolation measures. It also contributes to a higher survival rate in the event of accidental drops.

3.2 Fabrication

3.2.1 Design

The design of the MEMS actuator chip is clearly illustrated in the figures below. The dimensions shown are directly extracted from the GDS file used for electron beam lithography. The fabricated features closely matched the design specifications, with no significant deviations observed when verified using a scanning electron microscope (SEM).

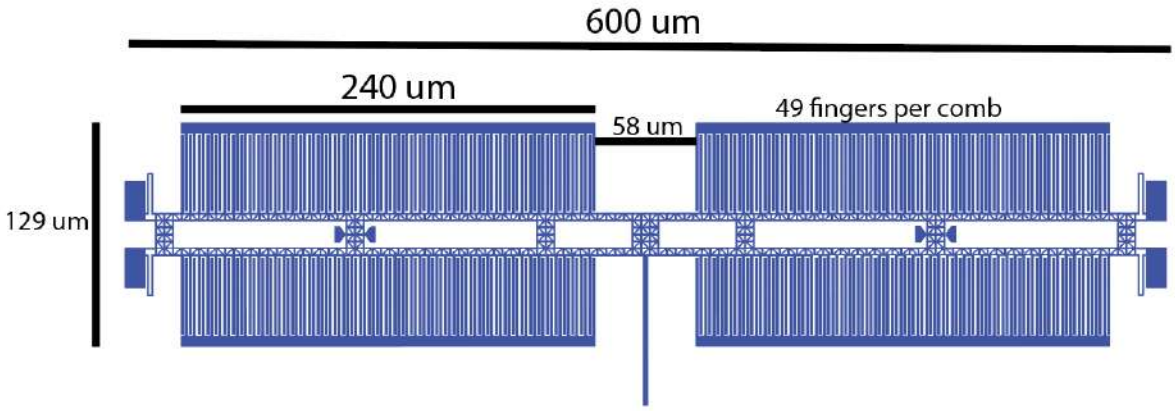

(a) The overview of the entire MEMS actuator.

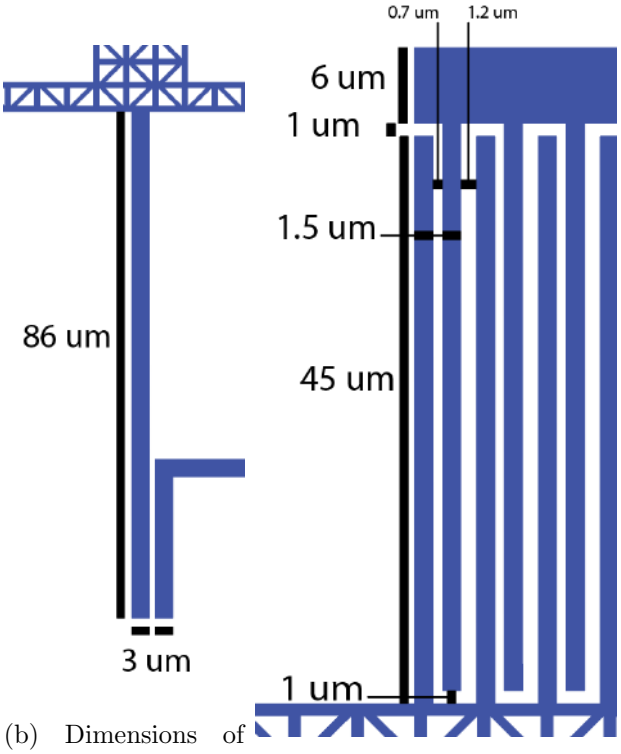

(b) Dimensions of the bar to be placed the nanotube.

(c) Dimensions of the comb fingers.

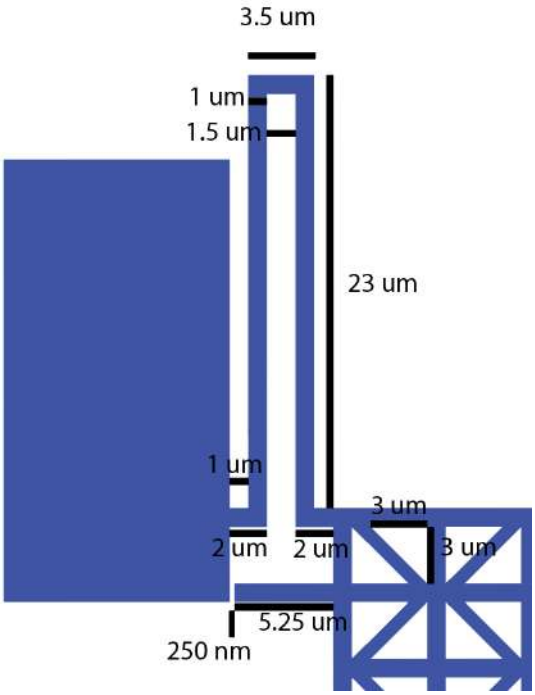

(a) Dimensions of the MEMS spring.

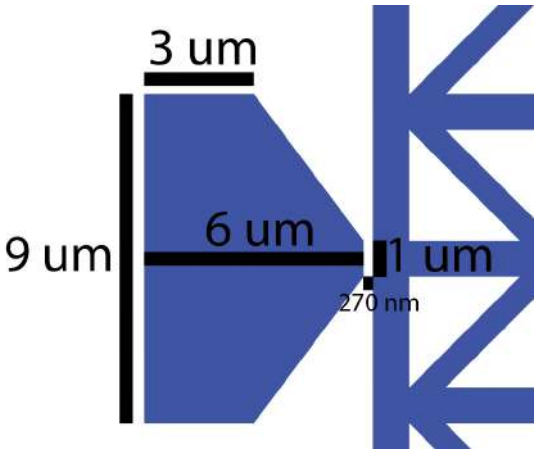

(b) Dimensions of the stopper.

3.2.2 Recipe

The following figures use 2D shapes to illustrate the recipe. For simplicity, steps such as coating the chips with resist, exposure to the electron beam, and development of the patterns are omitted.

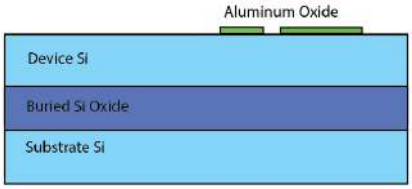

Aluminum oxide layer Utilizing the Atomic Layer Deposition method, selected area is coated with 25 nm Aluminum oxide. This step is crucial for the separation of gate electrode with the MEMS bar. As our chip is p-doped silicon, it is conductive and without an insulating barrier any voltage applied to the gate electrode and the MEMS bar will be short circuited from below.

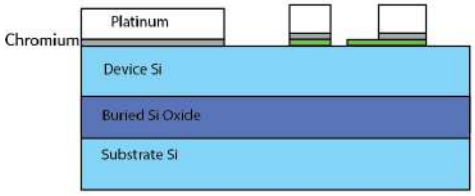

Deposition of MEMS After the aluminum oxide layer is created, the MEMS structure is deposited with 3nm Chromium + 130nm Platinum.

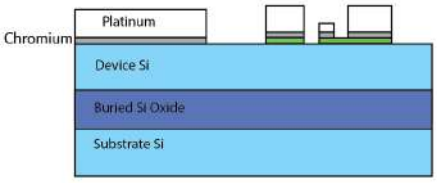

Deposition of gate After the deposition of MEMS structures, gate electrode is once more deposited with evaporation using 3nm Chromium + 35nm Platinum. Notice the 130-35=95 nm gap will be the distance of the gate electrode to the cnt bar suspended above the gate.

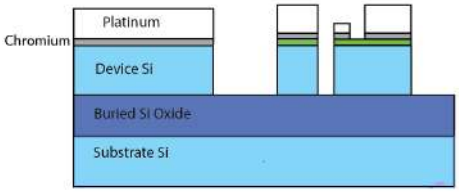

Deep silicon etching. The use of Reactive Ion etching and Deep Reactive Ion Etching (Bosch process), the device layer ,which is 3 um, is etched to reach the silicon oxide layer.

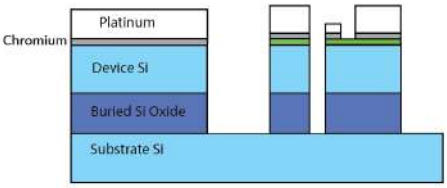

Buried Oxide Etching ICP-RIE etching to reach the substrate Si layer.

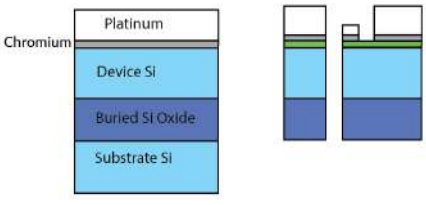

Etching of substrate level. This step is in order to increase the heigh between the top of the MEMS bar and the surface. This is needed due to the additional gap required for the automated CNT transfer, which brings the CNT to the chip with an approaching tip.

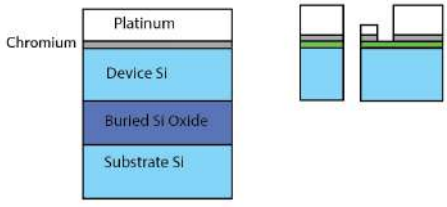

MEMS release The Vapor HF tools is used in order to etch the buried oxide layer using hydrofloric acid in gas form. This step prevents any liquid buildup, thus it is safe from stiction due to liquid surface tension effects.

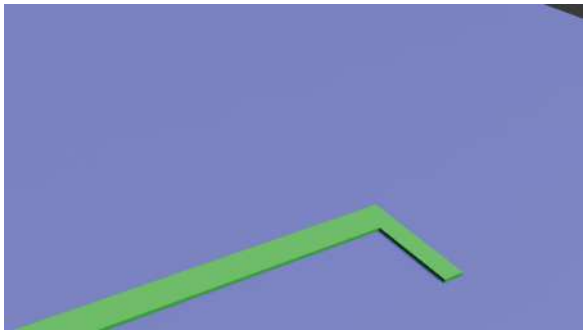

(a) Aluminum Oxide layer is fabricated.

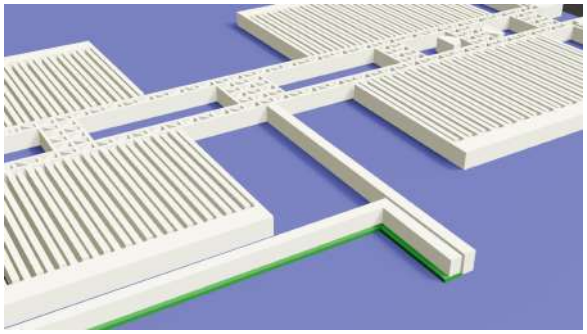

(b) 3nm Chromium + 130nm Platinum MEMS structure layer is fabricated, which is the white layer.

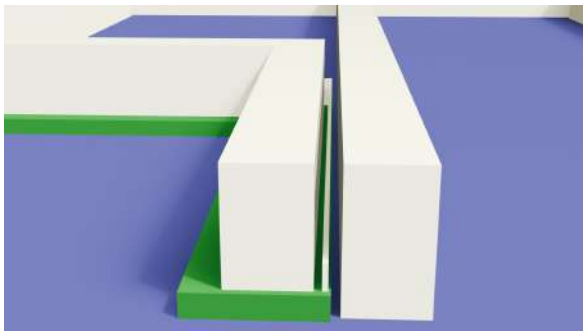

(c) Gate electrode between the MEMS bar is fabricated.

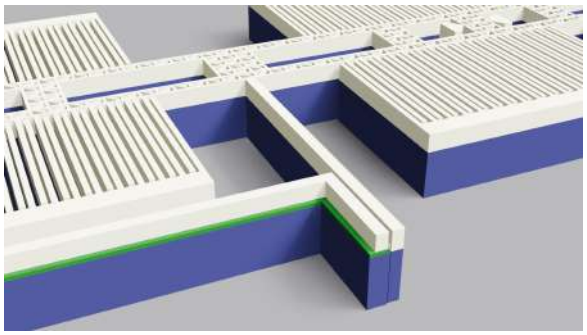

(d) Device layer silicon, which is the purple layer, is etched until the oxide layer.

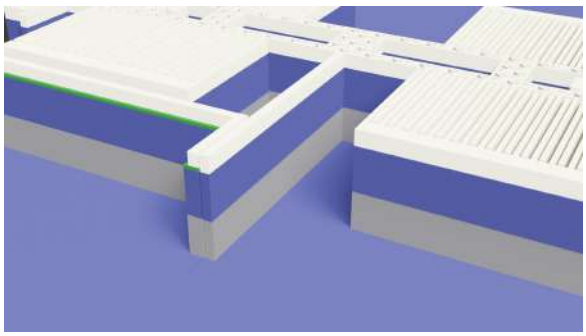

(e) Silicon oxide layer, which is the grey layers, is etched until the handle layer.

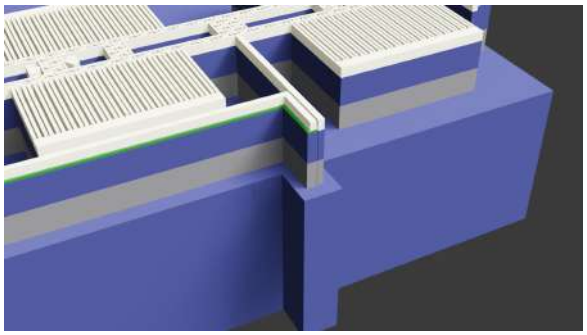

(f) Handle layer silicon is etched to create a trench in order to place the carbon nanotube on the chip using an nano actuated external device.

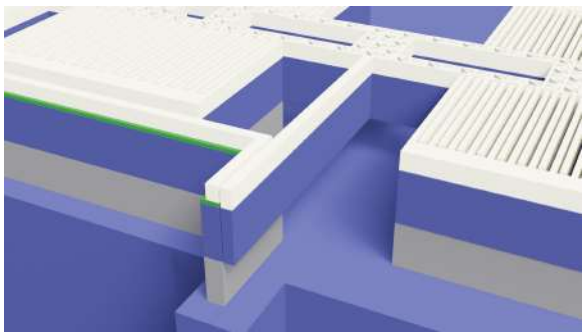

(g) Using vapor HF, the oxide layer under the MEMS is etched to suspend it in air.

Figure 32: The fabrication steps. The dimensions shown in the figures are accurate, except for the thicknesses.

3.3 Encountered Errors

Removal of triangles In this context, the term triangles refers to the structural, grid-like triangular patterns visible in the design section. These shapes are essential for the release of the MEMS actuator, as the RIE and DRIE processes must etch holes within these triangular regions to expose the oxide layer for the subsequent vapor HF release step. During vapor HF etching, the chip must be exposed long enough to fully release the movable structures, but not so long that the fixed regions are also etched away. The triangular design helps achieve this balance by creating areas with reduced oxide thickness beneath the platinum (Pt) layer of the MEMS, facilitating controlled and selective release. The problem encountered during the fabrication regarding this is the effective removal of these structures.

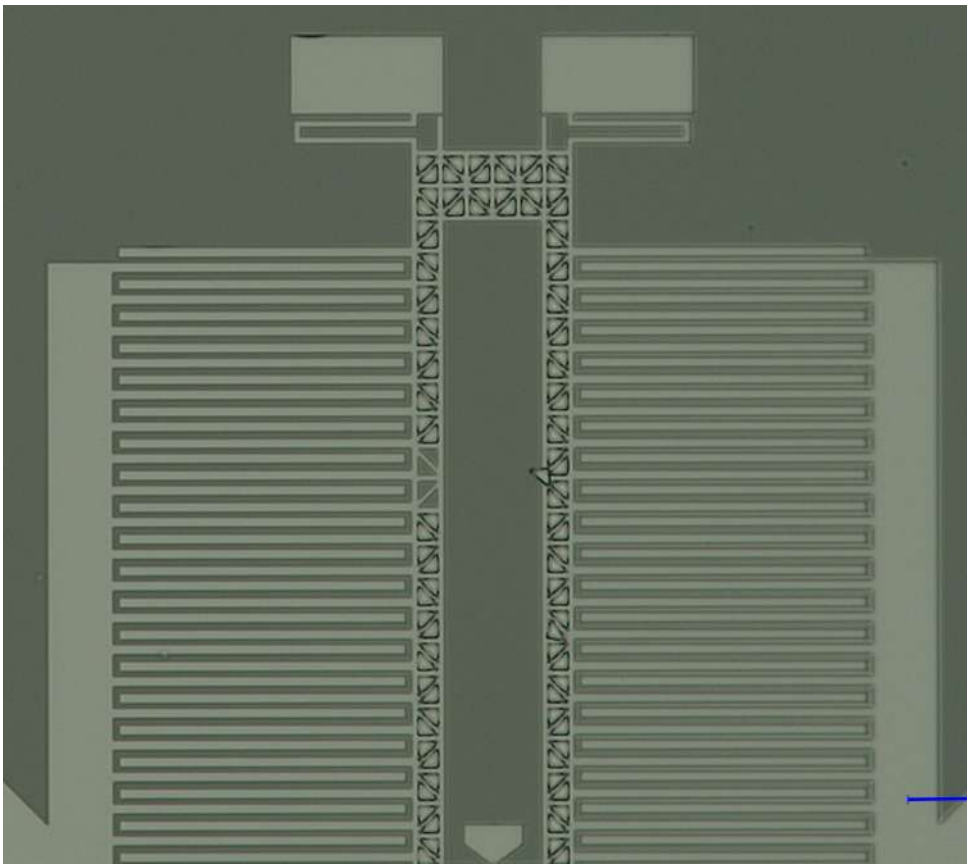

Figure 33: It can be seen in this microscope picture that after the liftoff, there are still triangles remaining.

To begin, the effects of ultrasound were tested on the MEMS chips. Two test chips were prepared up to the metal evaporation stage. Following this, the chips were placed in a DMSO solution on a 110°C hot plate to perform the liftoff process. After liftoff, triangular structures remained on the surface, indicating incomplete removal. To address this, one chip was placed in an ultrasonic bath filled with IPA for 3 minutes, and the other for 5 minutes. In both cases, the ultrasound device was operated at low power. After the microscope pictures are taken, both of the test chips were put in ultrasonic bath with IPA for 1 minute at maximum power. Below are the compared pictures through the process.

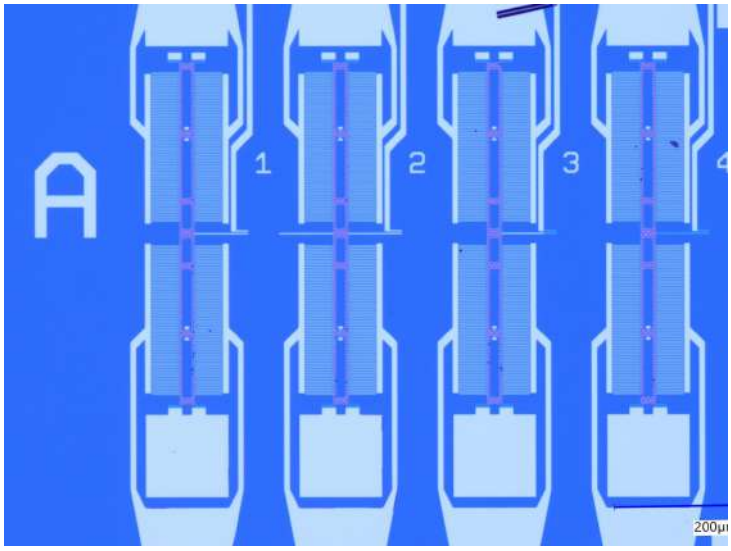

(a) After liftoff with DMSO

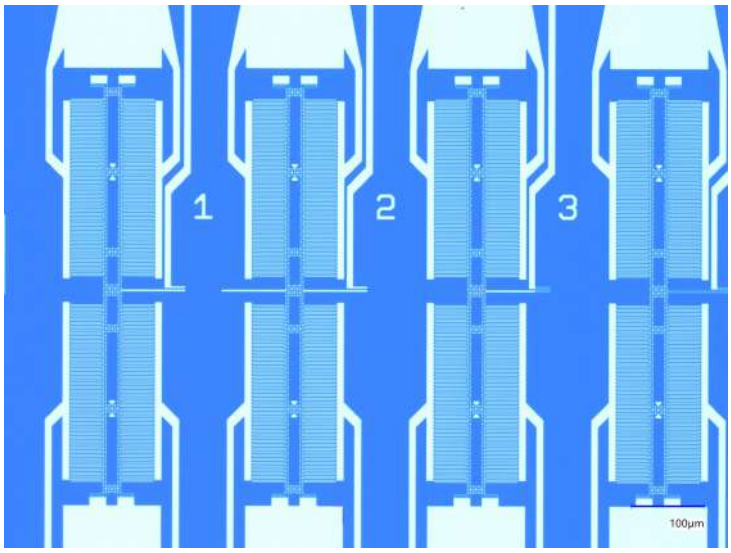

(b) After 3 minute ultrasound bath.

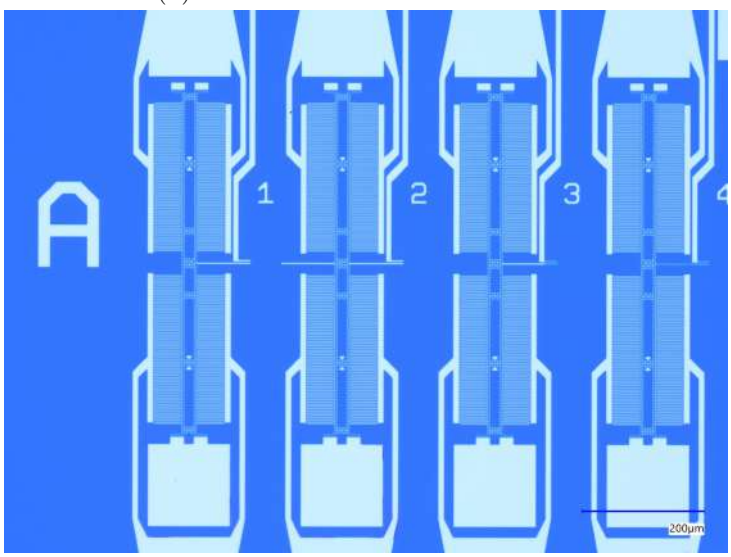

(c) After additional 1 minute ultrasound bath.

Figure 34: Here it is clearly seen that the first ultrasound step helps but is still insufficient to address complete removal of the triangles. The last ultrasound however seems to have removed all the triangles.

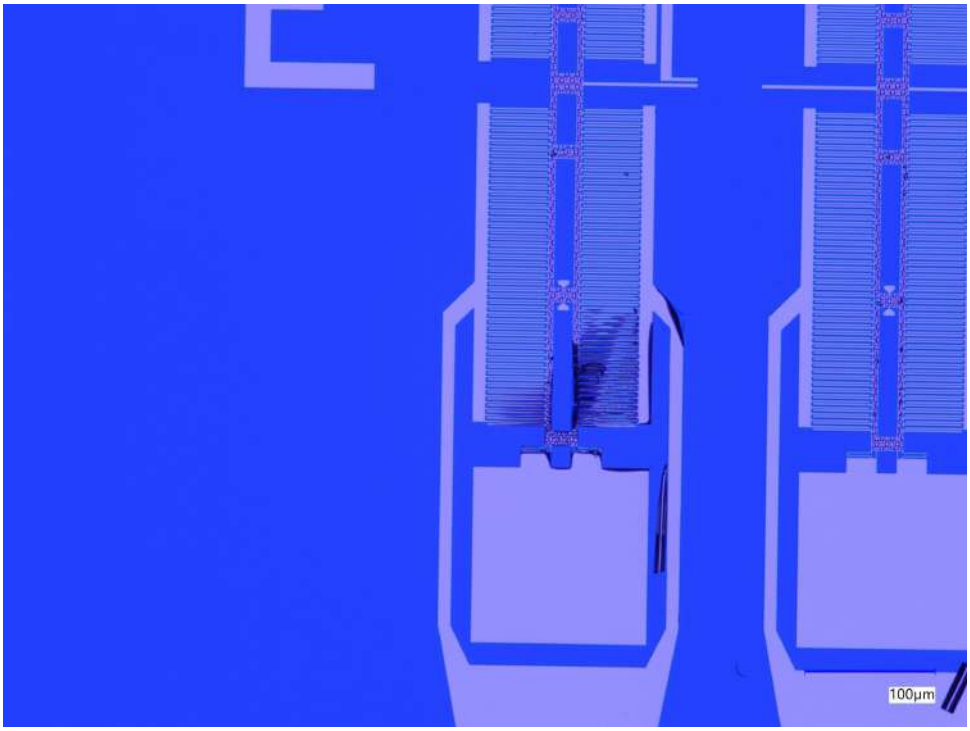

(a) After liftoff with DMSO

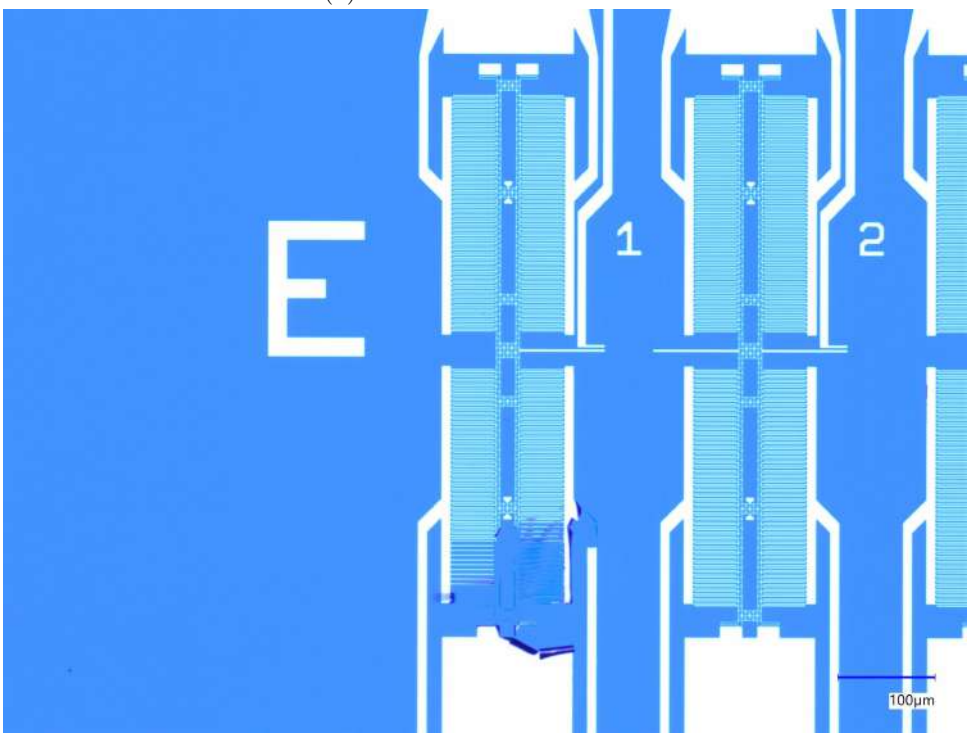

(b) After 3 minute ultrasound bath.

Figure 35: It is also important to see other effects of the ultrasound which is to destroy weak structures. Due to contamination the region E was defective and the structures were not deposited strongly. The black lines around the structures on image a) is due to the curving of platinum metal strip such that the microscope light is not reflected back. On the image b) one can clearly see the damage done on the chip after the 3 minute ultrasound at low power.

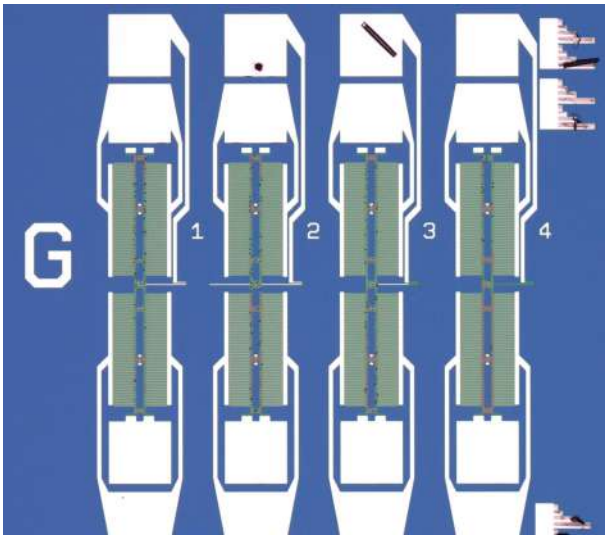

(a) After liftoff with DMSO

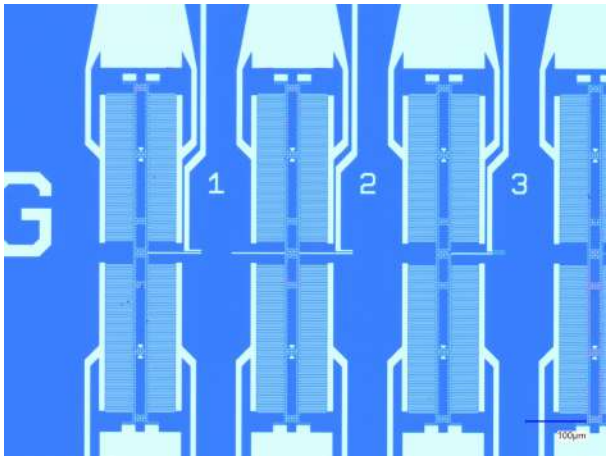

(b) After 5 minute ultrasound bath.

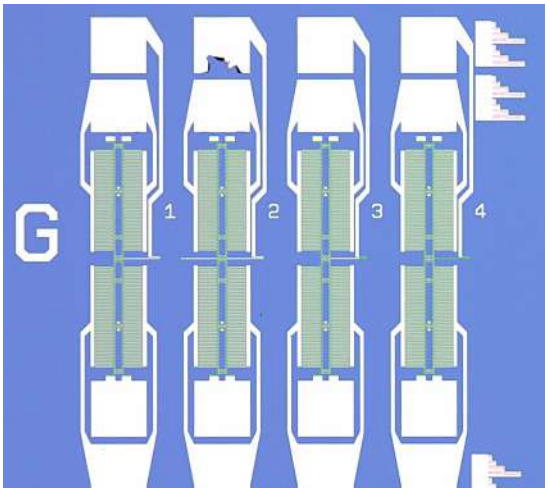

(c) After additional 1 minute ultrasound bath.

Figure 36: On the image a) the purple dots are the triangles. It can be seen that 5 minute ultrasound bath was also not sufficient to completely remove structures. The additional 1 min ultrasound appears to have cleared the triangles but know the debris from the previous step seems to have damaged the electrode. The step like structures on the side are irrelevant for this discussion.

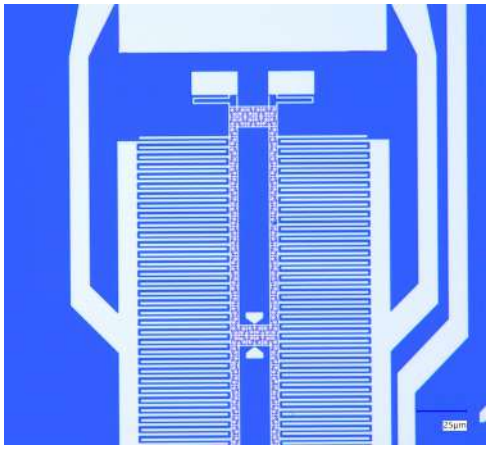

(a) After liftoff with DMSO. Close up on 1st structure on J block.

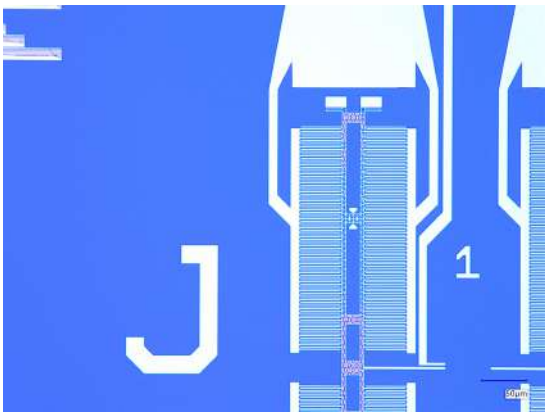

(b) After 5 minute ultrasound bath.

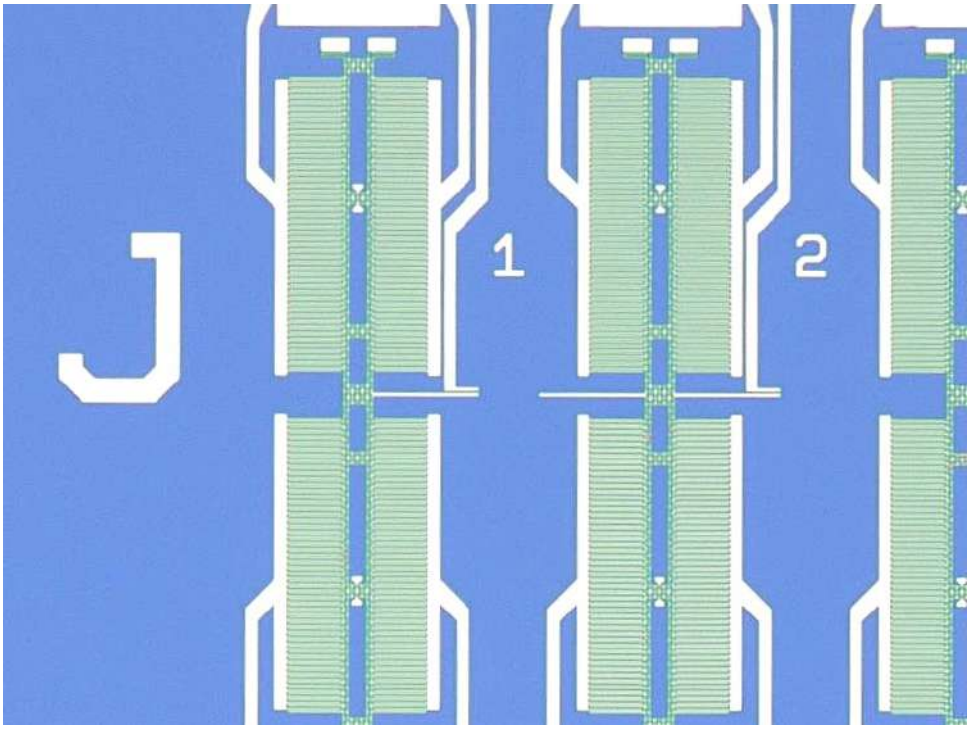

(c) After additional 1 minute ultrasound bath.

Figure 37: The triangles can be clearly seen in the image a). 5 minute ultrasound bath had effects but was not sufficient. Additional 1 minute bath seems to have a stronger effect.

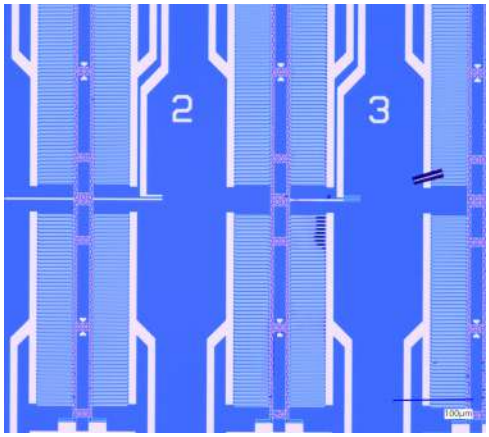

(a) After liftoff with DMSO. Close up on 2nd structure of C block.

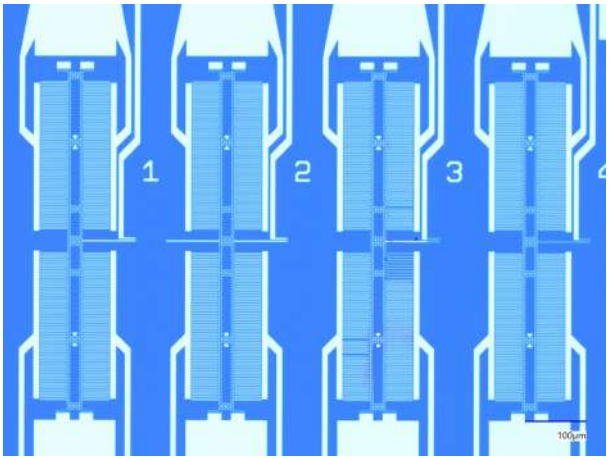

(b) After 3 minute ultrasound bath.

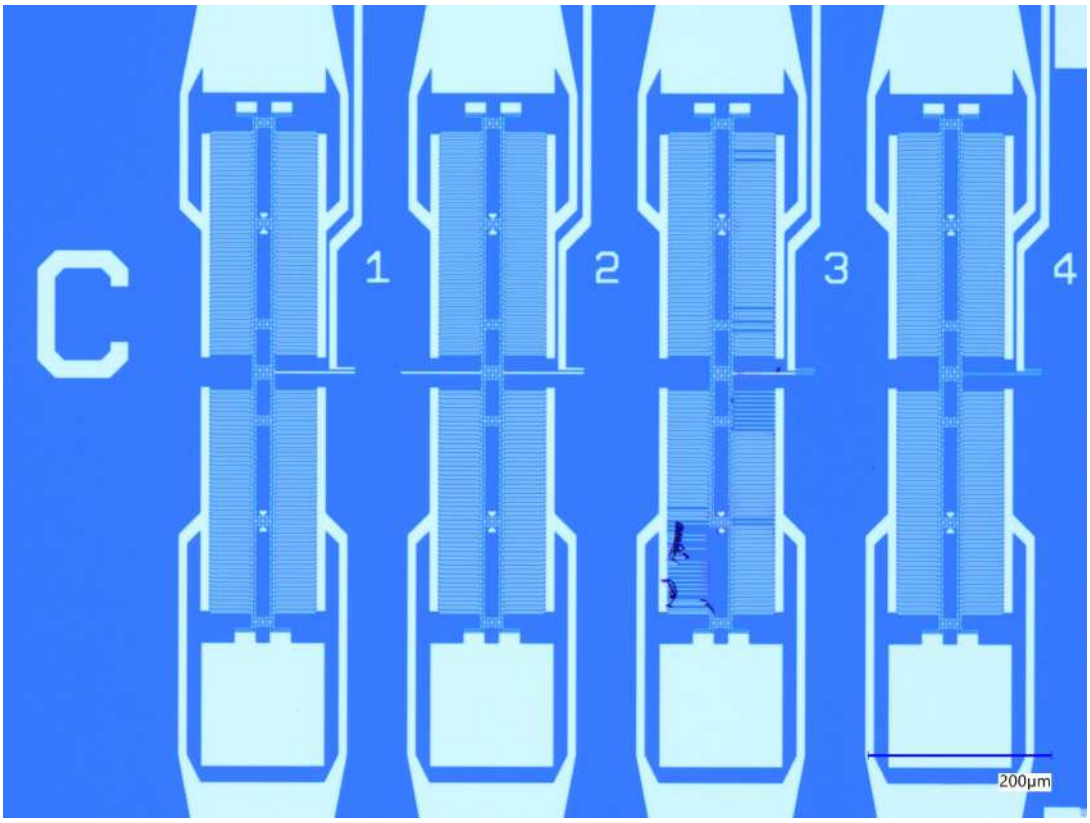

(c) After additional 1 minute ultrasound bath.

Figure 38: The damage ultrasound causes can be clearly seen in this line of trial. Careful examination shows that the metal in 2nd structure has black edges at the tip of the fingers which indicates ineffective deposition and thus bad adhesion. The following ultrasound steps therefore easily lift the metal more and more causing it to bend, break and tear.

Therefore, the use of ultrasound after liftoff is not a particularly reliable method for cleaning or post-processing. During the ultrasound treatment, debris may be dislodged and pose a risk of damaging sensitive structures. Furthermore, ultrasound can potentially disrupt or completely remove regions that were imperfectly deposited, leading to further degradation of the device. In addition, the process might leave behind unwanted residual features, such as triangular structures, which can affect the device's functionality or integrity. These issues highlight the limitations of relying on ultrasound as a final step

in the fabrication process, particularly when precision and surface quality are critical.

In order to understand the issues regarding these triangles the Scanning Electron Microscope pictures are taken for further analysis.

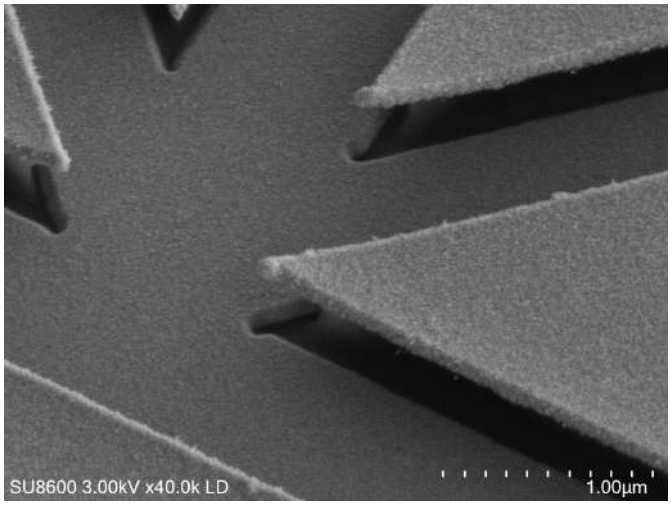

(a) SEM picture of the structures right after metal evaporation. The seen structures are the Platinum metals. The triangles that seem to float sit on top of the e-beam resist which is invisible to SEM.

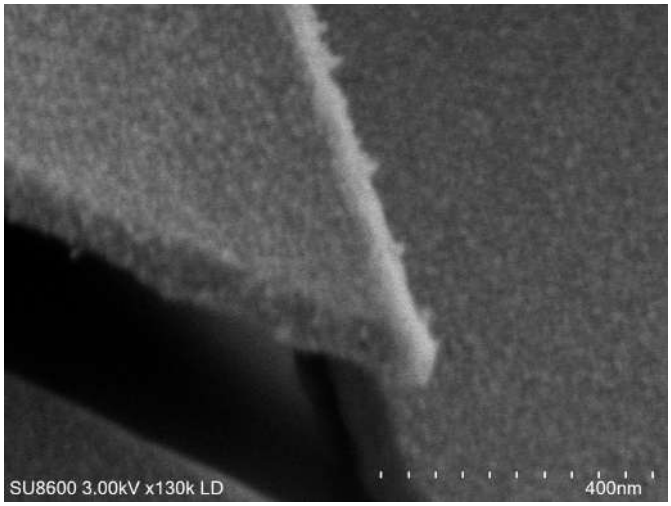

(b) More close up image of the edge of a triangle.

Figure 39: A thorough investigation into the metal evaporation process was conducted to determine whether any artifacts could be responsible for the unexpected removal of the triangular features during the liftoff step. The analysis revealed no evidence of anomalies or irregularities in the metal deposition that could account for this issue. In particular, the deposition was confirmed to be highly directional, as intended, which minimizes the risk of unwanted sidewall coating. Furthermore, no significant accumulation of metal was observed on the vertical walls of the resist structures, which could have otherwise caused mechanical binding between the deposited layer and the resist pattern. These findings suggest that the evaporation step itself is not the source of the problem, and that other factors in the process may be contributing to the detachment of the triangles during liftoff.

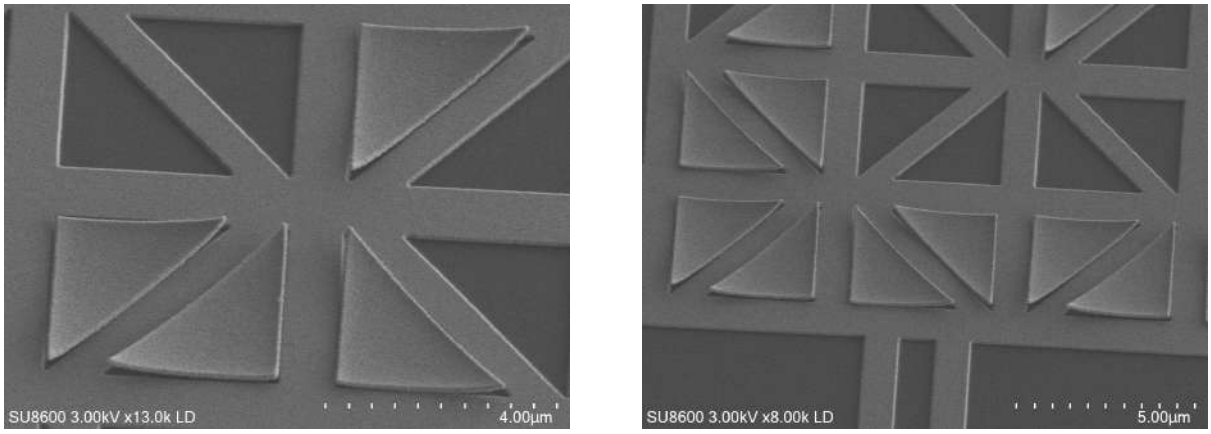

(a) SEM picture, right after liftoff in DMSO.

(b) Same chip different region.

Figure 40: An additional test chip was fabricated and processed up to the liftoff stage using dimethyl sulfoxide (DMSO). Photographs were taken immediately after the chip was removed from the DMSO to capture the immediate results of the liftoff process. Following the DMSO treatment, the sample was sequentially rinsed in acetone and isopropyl alcohol (IPA), with gentle pipetting applied to avoid introducing any mechanical stress that might affect the integrity of the delicate features. The resulting images revealed that the triangular metal features had largely settled below the surface, suggesting that the DMSO successfully penetrated beneath the structures and dissolved the underlying resist layer. Interestingly, the triangles visible in the post-liftoff images are likely those that remained only partially adhered, as they could not be fully removed even when subjected to ultrasonic agitation in previous tests. Notably, these remaining triangles exhibited a distinct deformation pattern: their edges were visibly bent upwards and away from the substrate surface, while the central region remained in contact with the silicon. This deformation strongly suggests the presence of a residual adhesive or cohesive force acting between the central portion of the triangles and the silicon substrate. The geometry of the bending implies that while the resist beneath the perimeter was effectively removed, the central area of the triangle may still be subject to interactions—possibly van der Waals forces or surface tension effects—that hinder complete detachment. These observations offer valuable insight into the nature of the adhesion mechanism and provide a direction for further investigation into improving the liftoff process for such fine structures.

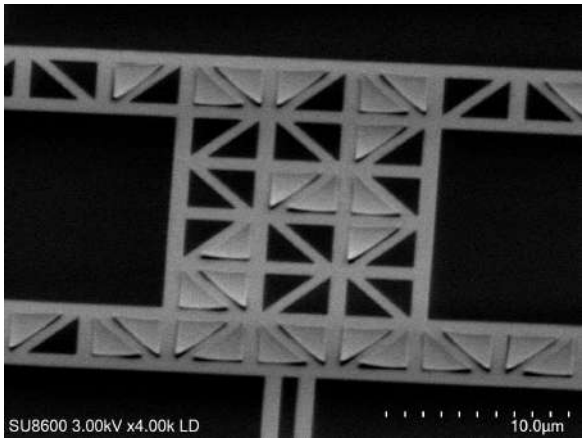

(a) Same chip different region.

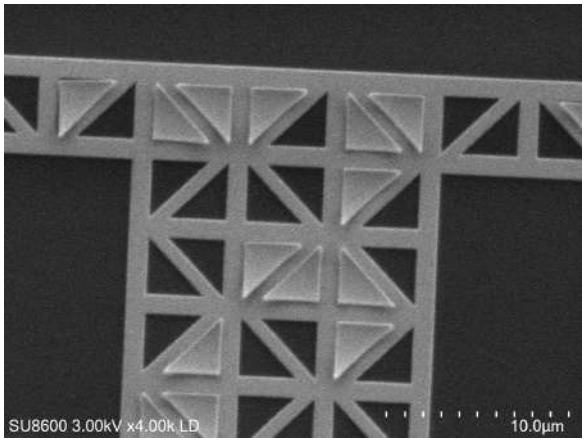

(b) Close up on upper part.

Figure 41: Another examined region of the sample provides further insight into the behavior of the triangular structures during the liftoff process. In this area, it becomes clearly evident how significantly the triangles were deformed, with their edges visibly lifted and bent upward while only the central portion remains in contact with the substrate. This distinct bending pattern reinforces the hypothesis that the triangles experience a localized adhesion force concentrated at their center, which prevents them from detaching fully during the resist removal stage. Moreover, careful observation reveals that the triangles appear to descend in a largely vertical manner during the DMSO liftoff process, showing minimal lateral displacement or rotational movement. This behavior suggests that the dissolution of the resist beneath the metal structures occurs relatively uniformly, allowing the features to settle downward without being swept away or misaligned by fluid currents. The lack of horizontal drift also implies that the triangles are not being mechanically dragged or influenced by strong surface tension gradients during the transition from resist-bound to free-floating. Together, these observations indicate a controlled and consistent resist dissolution process, but also point to the existence of a persistent adhesion mechanism at the center of the triangles.

Up to this point, we have observed that the rearrangement of triangles on the surface leads to adhesion issues, making them more difficult to remove during the liftoff process. To address this, two alternative methods were proposed: (1) performing an extended oxygen plasma etching before liftoff, allowing the use of a tape-peeling method instead of DMSO; and (2) conducting the DMSO liftoff process with the sample oriented upside down.

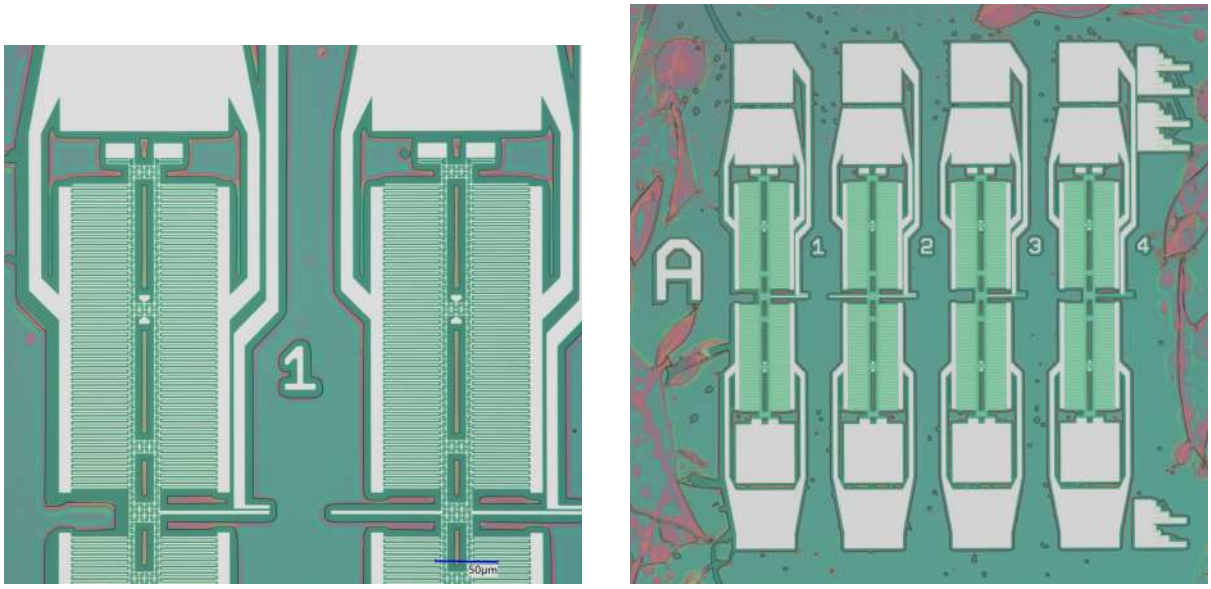

(a) Test chip for tape peeling.

(b) Same chip, A block.

Figure 42: In image (a), the thick line surrounding the white metal structures indicates the area of the resist that was etched by oxygen plasma. After metal evaporation, the device was exposed to 600 watts of oxygen plasma for 7 minutes to weaken these structures and facilitate easier removal via tape peeling. Tests confirmed that this method was highly effective.

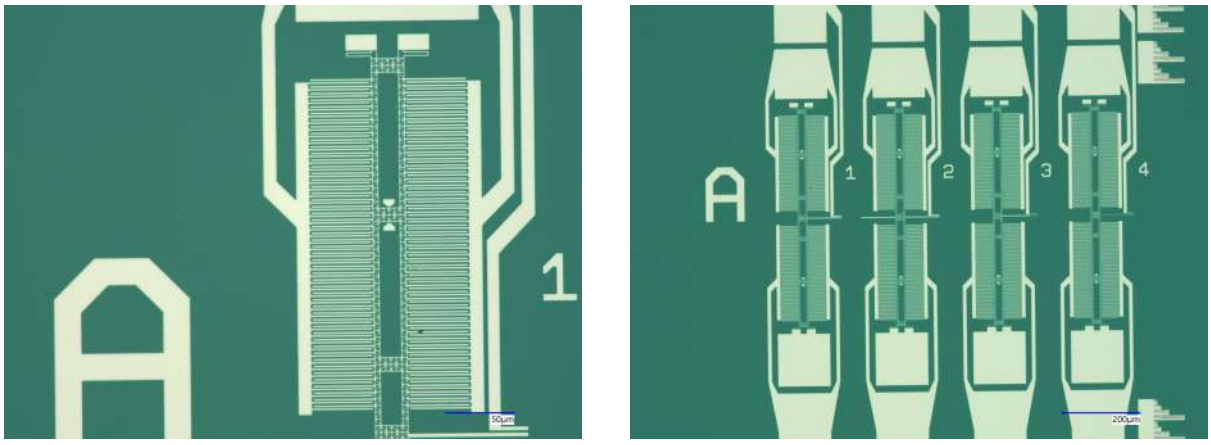

(a) Test chip for liftoff while upside down.

(b) Same chip, A block.

Figure 43: In this method, the test chip was first placed in DMSO and then subjected to an ultrasonic bath for 30 seconds at minimum power. Without removing the chip from the solution, it was flipped upside down and placed on a hot plate at 110°C for one hour. This approach also proved to be highly effective in removing the triangles.

In conclusion, the use of oxygen plasma treatment prior to tape peeling significantly facilitates the removal of resist structures, including the previously problematic triangular features. The plasma etching weakens the adhesion of these structures to the resist layer below, making them much easier to detach using a simple mechanical method like tape. Additionally, performing the liftoff process upside down in DMSO has proven to be an effective strategy for removing triangles. By inverting the chip during the DMSO bath and

subsequent heating, gravity works against the reattachment of the triangles to the surface, preventing them from settling and sticking due to adhesive contact. This orientation minimizes the chances of the triangles re-establishing contact with the substrate, thereby enhancing the overall efficiency of the liftoff process. Together, these methods represent promising improvements for simplifying the removal of delicate microstructures in device fabrication.

3.3.1 Displacement Test

To test the displacement of the MEMS comb actuator, a complete chip with comb actuator structure was fabricated. The central movable part was grounded, while the two opposing electrode combs were supplied with a constant voltage. The voltage was gradually increased from 0V to 9V in 1V increments. The corresponding images and analysis are presented below.

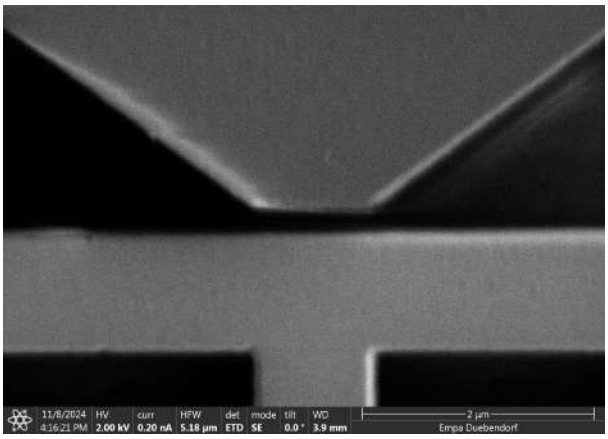

(a) SEM image of the stopper at 0 voltage applied to the combs.

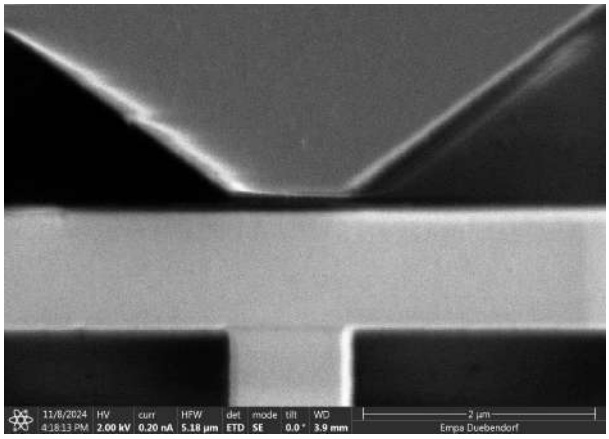

(b) SEM image at 7 volts.

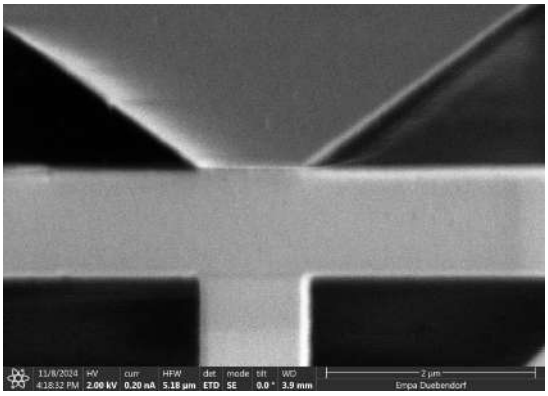

(c) SEM image at 9 volts.

Figure 44: Three images show the displacement of the MEMS actuator as voltage is applied to the side combs while the central actuator remains grounded. At 9 volts, the structure reaches its maximum displacement, limited by the stopper structures.

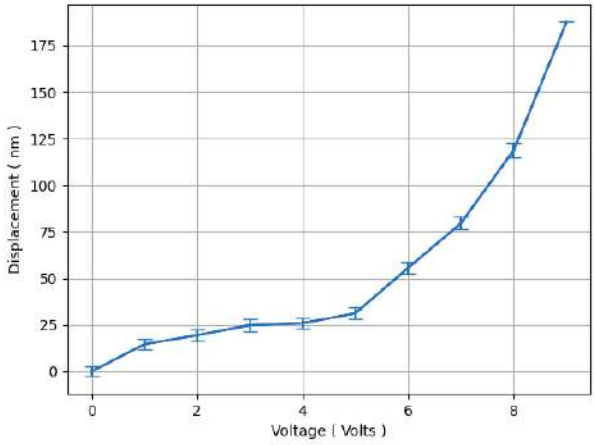

Voltage	Displacement	Standard Deviation
0 Volts	0 nm	2.52 nm
1 Volts	14.64 nm	2.94 nm
2 Volts	19.44 nm	3.05 nm
3 Volts	24.90 nm	3.31 nm
4 Volts	25.97 nm	2.91 nm
5 Volts	31.28 nm	2.93 nm
6 Volts	55.67 nm	3.13 nm
7 Volts	79.64 nm	3.32 nm
8 Volts	118.87 nm	3.87 nm
9 Volts	187.71 nm	0 nm

Figure 45: The data clearly shows a trend of linear displacement increase, followed by a characteristic pull-in behavior. At 9 volts, the comb structure is fully pulled into the stopper, indicating that the pull-in voltage lies between 8 and 9 volts.

To assess whether our device design was properly fabricated, SEM images were taken to measure the device dimensions. The results showed that the fabricated structures matched the initial design within a few tens of nanometers.

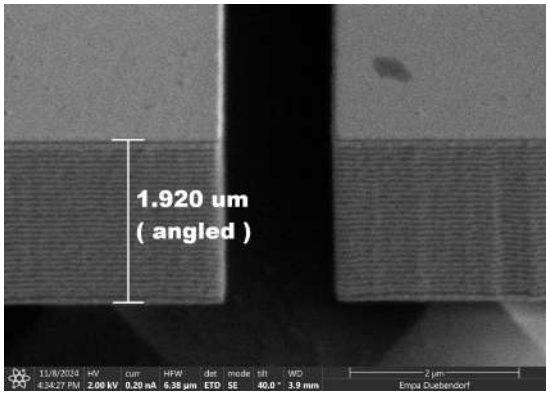

(a) Thickness of the bar to be placed the CNT.

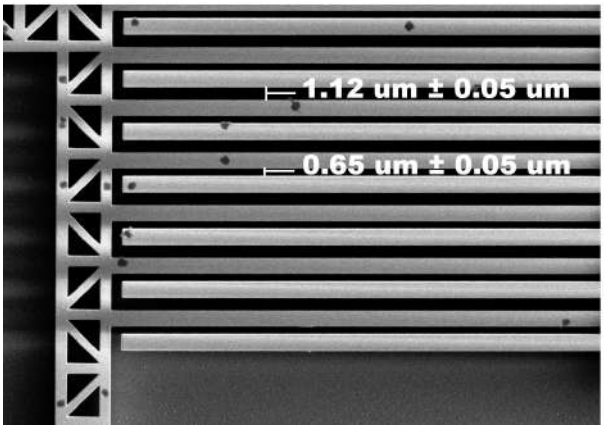

(b) Distances in between the combs.

Figure 46: In a), the thickness of the chip was measured using a scanning electron microscope (SEM) image taken at a 40° tilt where the angle is between the electron beam and the surface normal of the chip. The apparent thickness observed in the image was 1.920 µm. To obtain the true thickness, the measured value was divided by cos(50°), yielding a corrected thickness of approximately 2.98 µm. From these two measurements we obtain chip thickness 2.98 um and comb distances 0.65 um and 1.12 um.

3.3.2 Etching Test

To test the possible ranges of etching aspect ratios, a bar shaped test structures with increasing lengths and decreasing bar spacings are fabricated. These structures were on the same chip as the movement test chip, therefore they endured the same metal evaporation, RIE (Reactive Ion Etching) and DRIE (Deep Reactive Ion Etching - Bosch process) steps as the MEMS actuator.

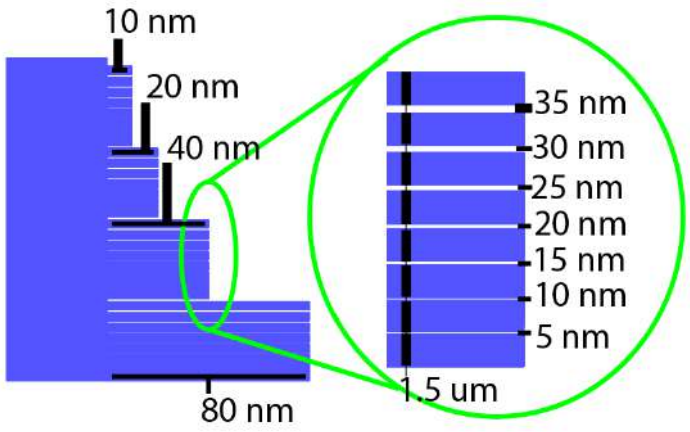

Figure 47: The design of the test structure can be seen from the figure. Increasing lengths from 10 to 20, 40 and 80nm bars with spacings in between them from 35 to 30 ,25 ,20 ,15 ,10, 5 nanometers. The bar widths are kept at 1.5 um which is small enough for vapor HF etching to remove the oxide layer below them and suspend them.

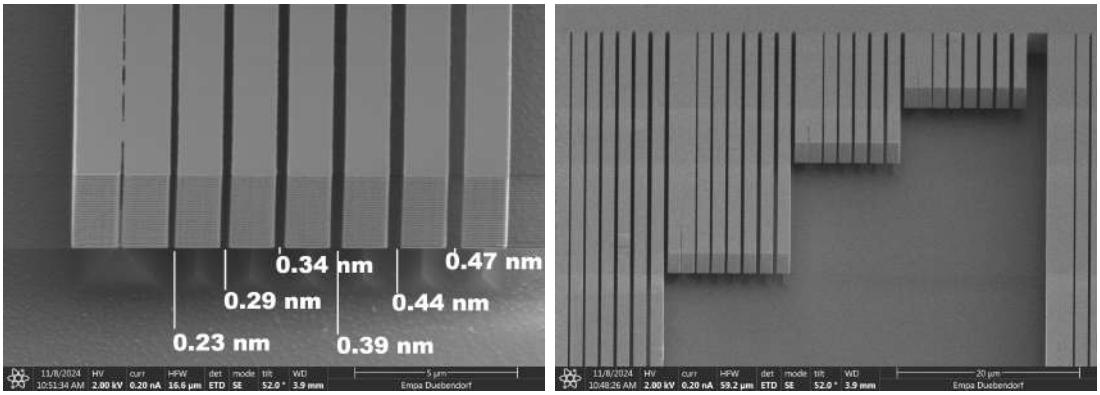

Figure 48: The measurements clearly show that all slits were successfully etched, except for the smallest one with a 5 nm gap. Additionally, the observed etching exceeds the intended design, indicating that even in the case of over-etching—which typically causes structures to widen—the smallest gap experienced minimal etching, and in some regions, it remained unetched. Close inspection beneath the narrowest slit reveals a large pyramid-shaped region, indicating the weakest etching of the oxide layer below. This is likely because, in this case, HF gas could only access the oxide from the sides, unlike in wider slits where it can also diffuse from above. Another point to consider is the lack of bending the these structures. The beam shaped silicon even with 80 um in length and 1.5 um is strong enough to carry its own weight and not bend downwards.

3.3.3 Burning resist

The issue encountered is the burning of the photoresist layer during the DRIE process used to etch trenches in the handle layer. Prolonged etching and inadequate chip cooling led to thermal damage, causing the resist to undergo chemical changes that made it highly resistant to further etching. This phenomenon is commonly referred to as reticulation in the literature.

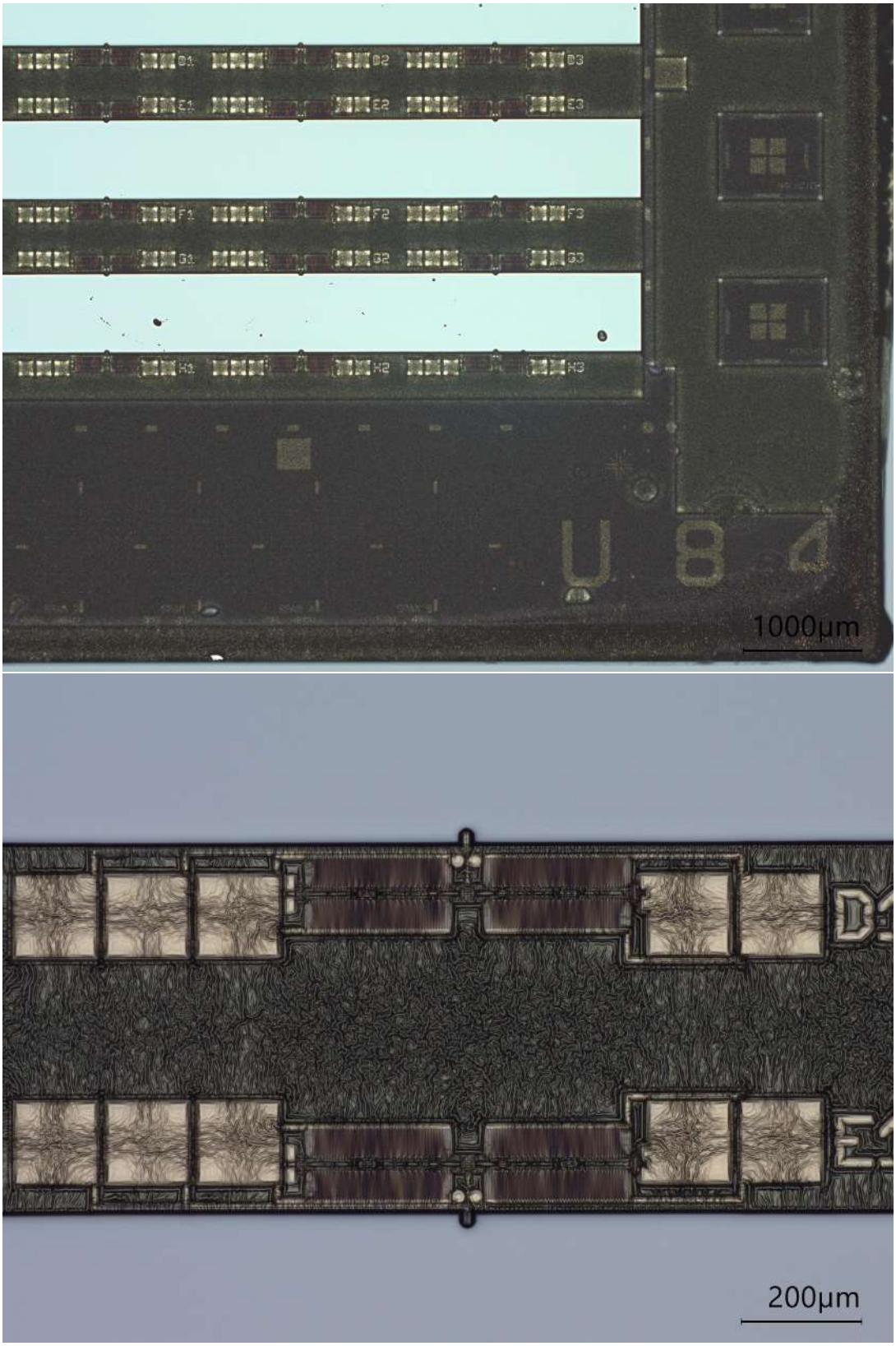

Figure 49: The chip after the DRIE step in order to etch the handle layer to create the trench structure for carbon nanotube placing nano actuator to approach. The darkened layer of photoresist clearly shows the burnt resist.

To reduce heat buildup in the resist layer caused by ion bombardment during the

etching process, a helium backside cooling system is used during the DRIE step to conduct heat away from the chip. To enhance thermal conductivity, thermal paste is applied to the back of the chip. The increased darkness around the corners of the chip is possibly due to bad smearing of the thermal paste, which didn't reach to corners when the chip was stuck to the wafer by pressing it onto a thermal paste drop.

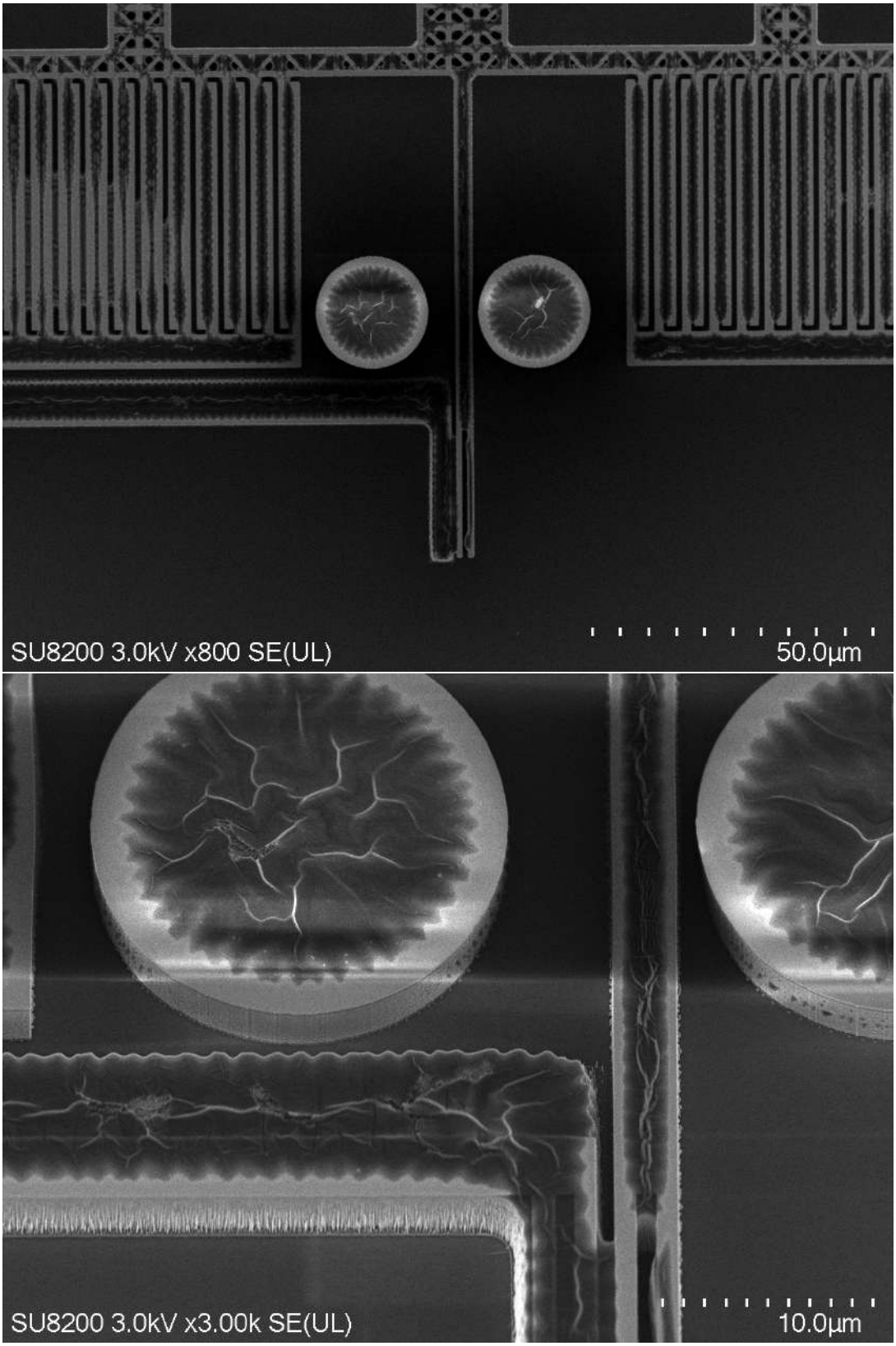

Figure 50: SEM pictures of the chip after extensive resist cleaning steps. The remaining resist residue indicates that the resist was chemically altered to be able to resist strong etching attempts.

Due to their organic and polymer-based composition, photoresist coatings are partic-

ularly vulnerable when subjected to plasma environments such as those found in glow discharge systems. Exposure to these conditions can cause various forms of physical and chemical degradation to the photoresist material. This degradation may present as hazing (a whitish or cloudy appearance), reticulation (a wrinkling or patterning effect due to overheating), general chemical breakdown, or creeping (distortion or flow of the resist layer). These forms of damage are not merely cosmetic—they significantly affect the subsequent stages of microfabrication. In particular, they can interfere with the reactive ion etching (RIE) process, often leading to undesirable outcomes such as etch lag (a slowdown in etch rate in certain regions) and microloading (variation in etch rates depending on feature density). These issues can compromise etch uniformity and pattern fidelity, ultimately impacting device performance and yield. [34]

In our case, the chip was subjected to a cleaning sequence consisting of immersion in DMSO at 110°C for 24 hours, followed by 24 hours in acetone, and finally an oxygen plasma treatment at 100W for 20 minutes. Despite this extended procedure, complete removal of the photoresist could not be achieved. This suggests that significant cross-linking occurred within the resist material, leading to the formation of a chemically inert surface layer resistant to conventional stripping methods.

Once cross-linked, unexposed photoresists become nearly insoluble and remain thermally stable at temperatures ranging from 150°C to 250°C. [35] This appears to be our case where excessive heating caused the resist to cross-link and become insoluble in organic solvents.

3.3.4 Defective Etching

Issue encountered here is the defective etching during first DRIE step in order to etch the device layer silicon.

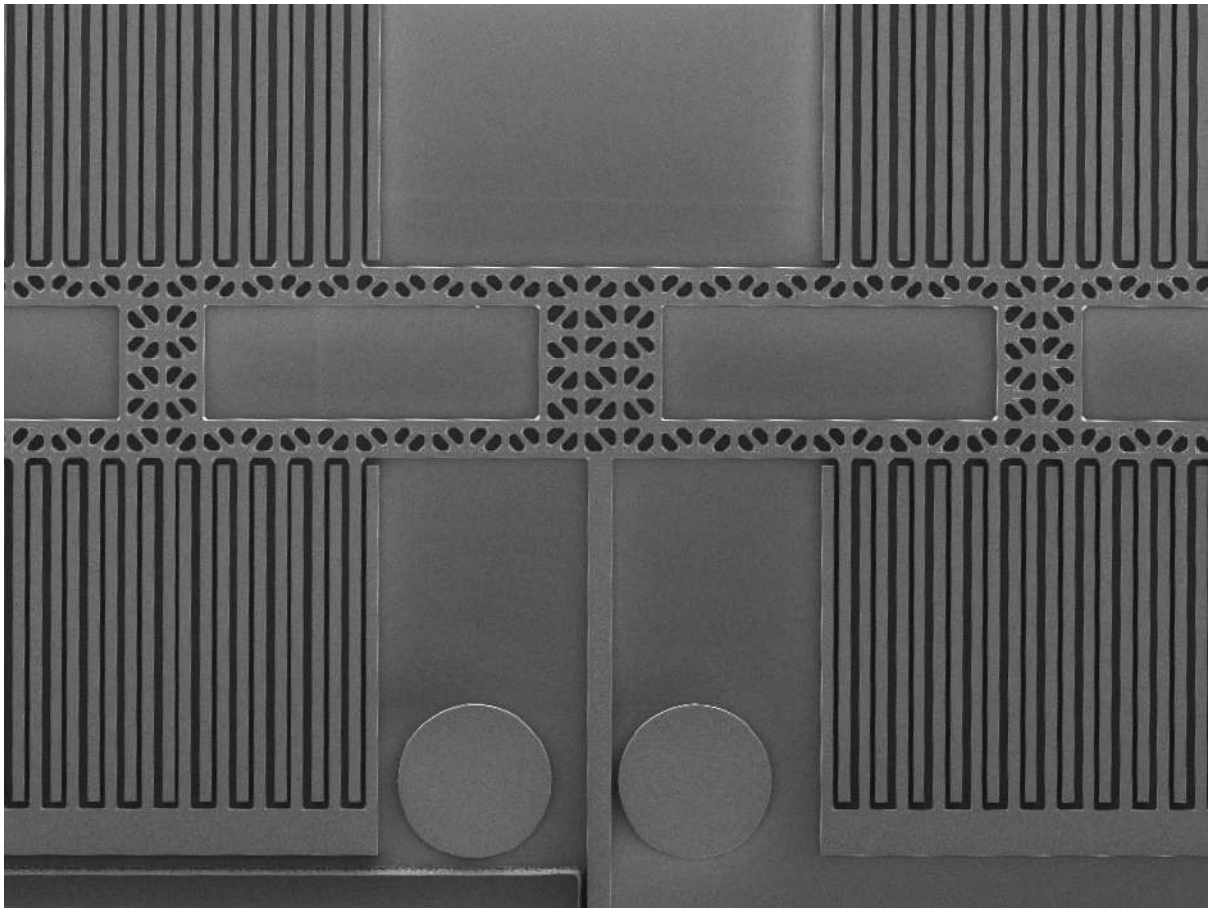

Figure 51: Upon inspection, it is evident that the triangular structures exhibit noticeable defects. Specifically, the sharp corners of the triangles appear underdeveloped, resulting in incomplete or inaccurate etching during the Deep Reactive Ion Etching (DRIE) process. This deficiency in corner formation suggests that the etching did not proceed as intended in these regions, potentially due to limitations in pattern transfer or resist performance. What is particularly significant is that this issue is consistently observed across all triangular features on the sample, rather than being isolated to a few locations. This uniformity indicates that the problem is not the result of a localized defect, such as particulate contamination or random photoresist failure. Instead, it points to a systematic issue in the fabrication process—likely stemming from the development of resist, which must be addressed to ensure reliable pattern fidelity in future iterations.

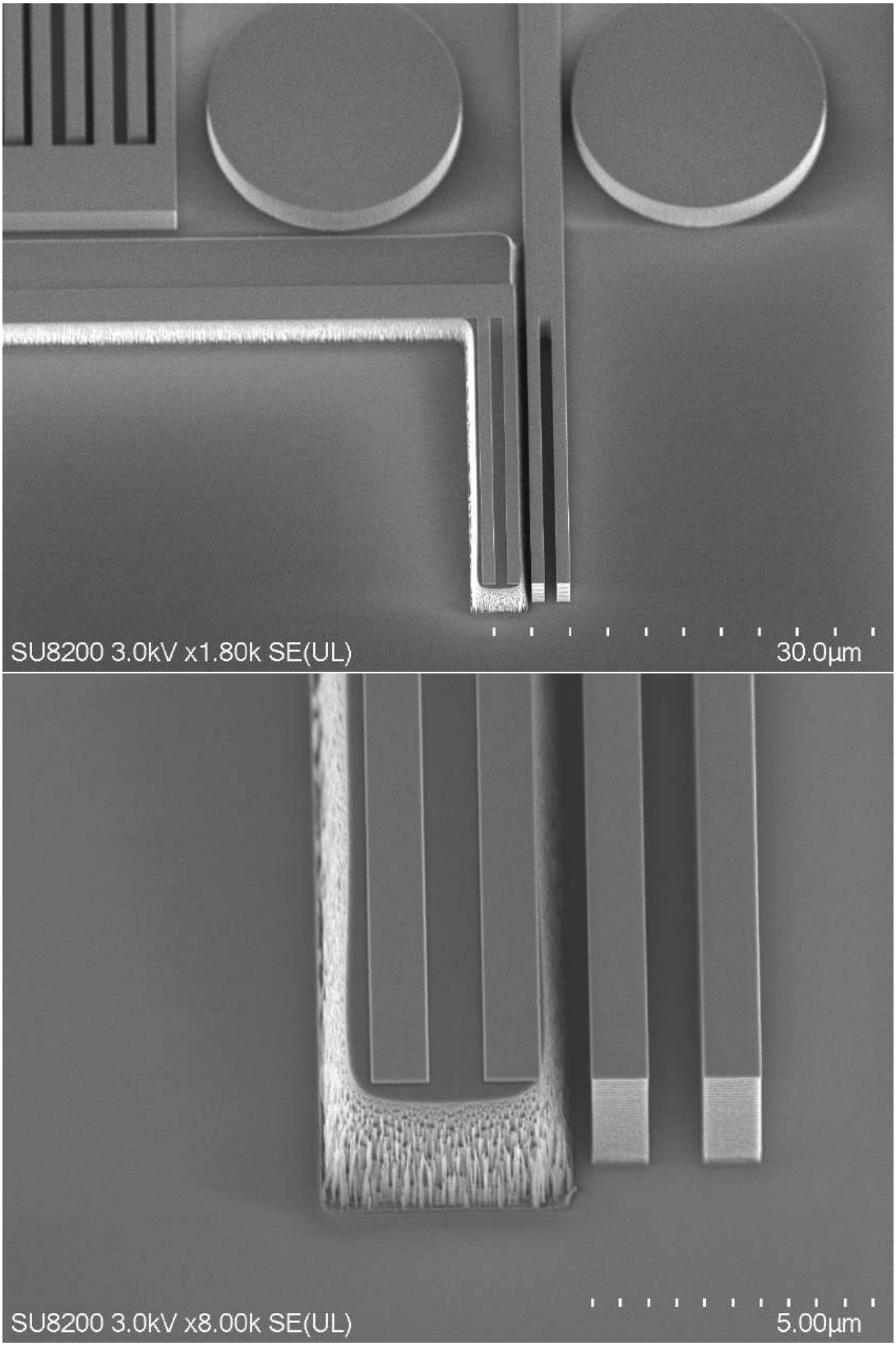

Figure 52: SEM pictures of the bar structure after removing resist by solvents.

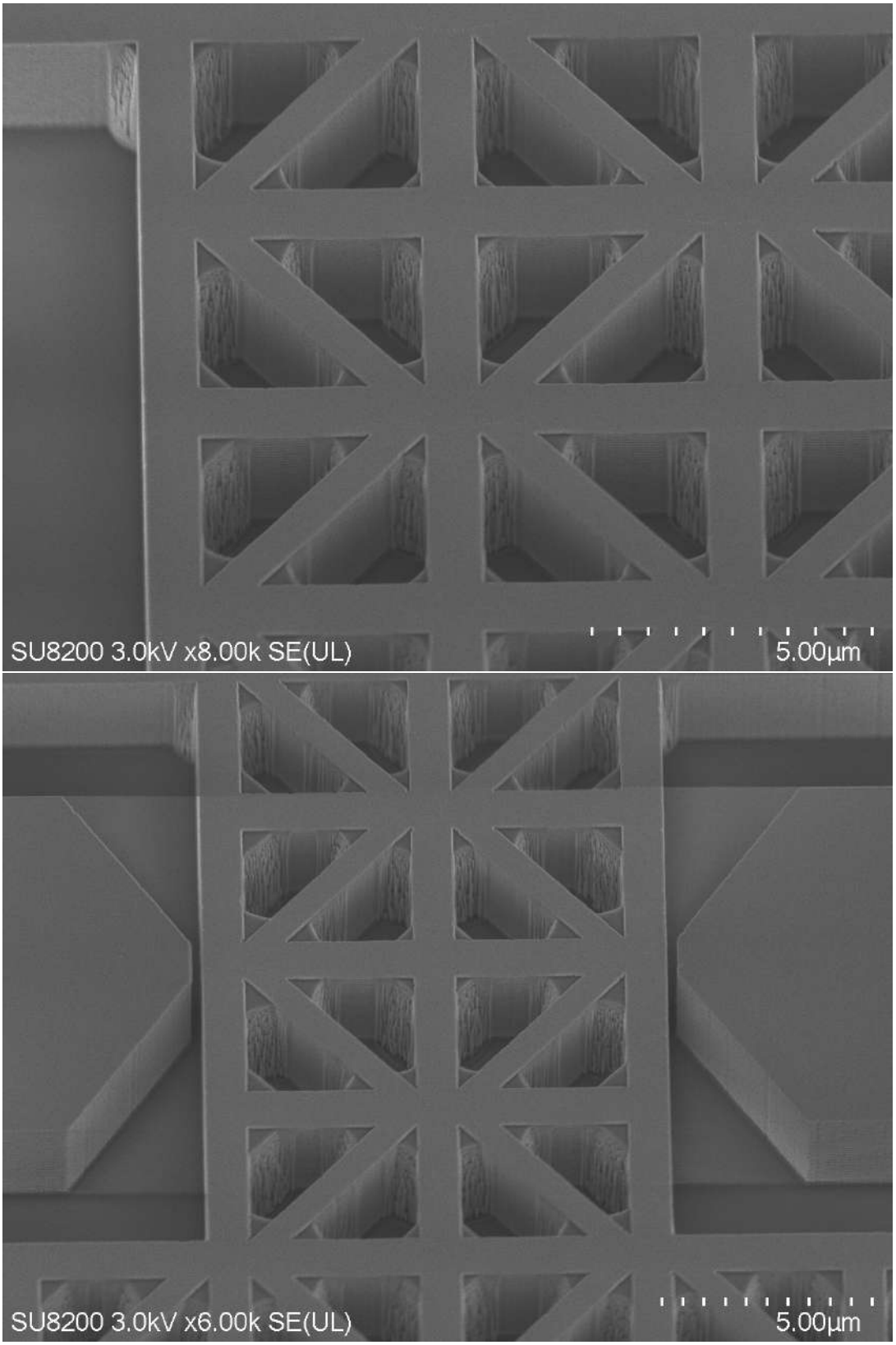

Figure 53: A close-up examination of the triangular regions.

SEM image reveals distinct anomalies in the etching behavior, particularly at the sharp corners of the structures. It appears that the silicon in these corner regions was partially shielded or inadequately exposed during the DRIE process, leading to incom-

plete etching. This suggests that either the photoresist coverage in these high-curvature areas was uneven, or the plasma etch chemistry did not effectively reach these zones due to aspect ratio-dependent effects or local charging. In addition to the unetched corners, the sidewalls of the triangular features exhibit irregular textures and protrusions, indicating further complications during the etch. These undesired formations on the sidewalls are known as "grass" or "grass-like structures" in the microfabrication literature. They are typically caused by micro-masking effects, where small residues or redeposited materials shield localized regions of the silicon from the plasma, allowing narrow, needle-like features to remain after etching. The presence of grass not only compromises the structural fidelity of the patterns but can also interfere with subsequent process steps, such as bonding or coating. These observations collectively point to a broader issue with the etch uniformity and resist performance, particularly in high-aspect-ratio and geometrically complex features like sharp corners.

It is worth noting that grass formation is caused by many effects. One study shows that the grass formations happens at certain mixings of SF_6 and C_4F_8. In the study [36], it was observed that increasing the SF_6 gas flow rate leads to a noticeable rise in surface roughness at the bottom of etched trenches. Additionally, the formation of silicon "grass" structures—long, needle-like protrusions—was reported on the trench floors. This phenomenon is attributed to the reduced etch cycle duration, which prevents the complete removal of the polymer passivation layer at the bottom surface. The residual polymer effectively acts as a secondary mask, shielding portions of the silicon substrate from the etching plasma. As a result, the unetched silicon remains as filamentous structures, commonly referred to as "grass" in the microfabrication literature.

Since grass formation is absent from the flat bottom regions of the chip and is instead localized around areas with sharp corners, this suggests that the issue does not stem from the DRIE recipe itself—including parameters such as the SF_6 flow rate—but rather from inadequate photoresist development. In these sharply angled regions, residual organic material likely remained due to poor resist processing, acting as a secondary mask during the etch. This residual layer facilitated the accumulation of polymer films generated by C_4F_8 during the passivation phase of the DRIE process, which in turn inhibited uniform silicon etching and led to the formation of needle-like structures in those localized regions.

3.3.5 Defects After HF Release

Once all DRIE and RIE etching steps are completed, the MEMS structure must be released by removing the underlying silicon oxide layer to allow it to become suspended. This release process is typically carried out using vapor-phase hydrofluoric acid (HF) etching, which isotropically etches the silicon oxide.

In this method, HF—normally a liquid at room temperature—is converted into a vapor and introduced to the chip. Vapor-phase etching is preferred over liquid HF etching because the presence of liquid droplets can cause severe damage to fragile MEMS structures due to surface tension forces. In contrast, vapor HF avoids these destructive capillary effects, making it much safer for delicate features.

Moreover, vapor HF etching eliminates the need for post-etch rinsing and drying steps, which are often complex and can introduce further risk of damage. Another key advantage of vapor-phase etching is its finely tunable etch rate, which can range from 5 to 1200 Å/min. This precise control is critical to ensure that only the sacrificial oxide is removed without compromising the structural anchors that support the suspended

components.

The vapor HF release process is carried out using the Primaxx uEtch System, and the chemical reactions involved in this dry etching method are as follows [37]: The process begins with the introduction of a gaseous mixture of hydrofluoric acid (HF) and ethanol into the etching chamber. Once these vapors are adsorbed onto the chip's surface, they undergo chemical ionization, generating the reactive species responsible for etching:

$$HF(ads) + C_2H_5OH(ads) \rightarrow HF^{-2}(ads) + C_2H_5OH^{+2}(ads)$$

The interaction between the reactive species and the sacrificial silicon dioxide layer on the wafer surface leads to the formation of silicon tetrafluoride gas and water vapor as byproducts.

$$SiO_2(ads)+4HF^{-2}(ads)+4C_2H_5OH^{+2}(ads) \rightarrow SiF_4(ads)+2H_2O(ads)+4C_2H_5OH(ads)$$

Ethanol serves as a crucial catalyst in the etching process, facilitating the reaction without being consumed. In its absence, the etching of SiO_2 simply will not take place. Additionally, ethanol helps maintain a dry wafer surface, enabling the efficient removal of reaction byproducts through pumping.

However, since water vapor is produced during etching, careful optimization of the process parameters is essential. These conditions must be tailored to the specific device to prevent stiction a common issue caused by the presence of water—that can compromise the release and integrity of the delicate MEMS structures. In this section, our recipe used titanium instead of chromium meaning that the Platinum layer had Titanium under it. We have later adopted Chromium as the adhesion layer after encountering the issues described below.

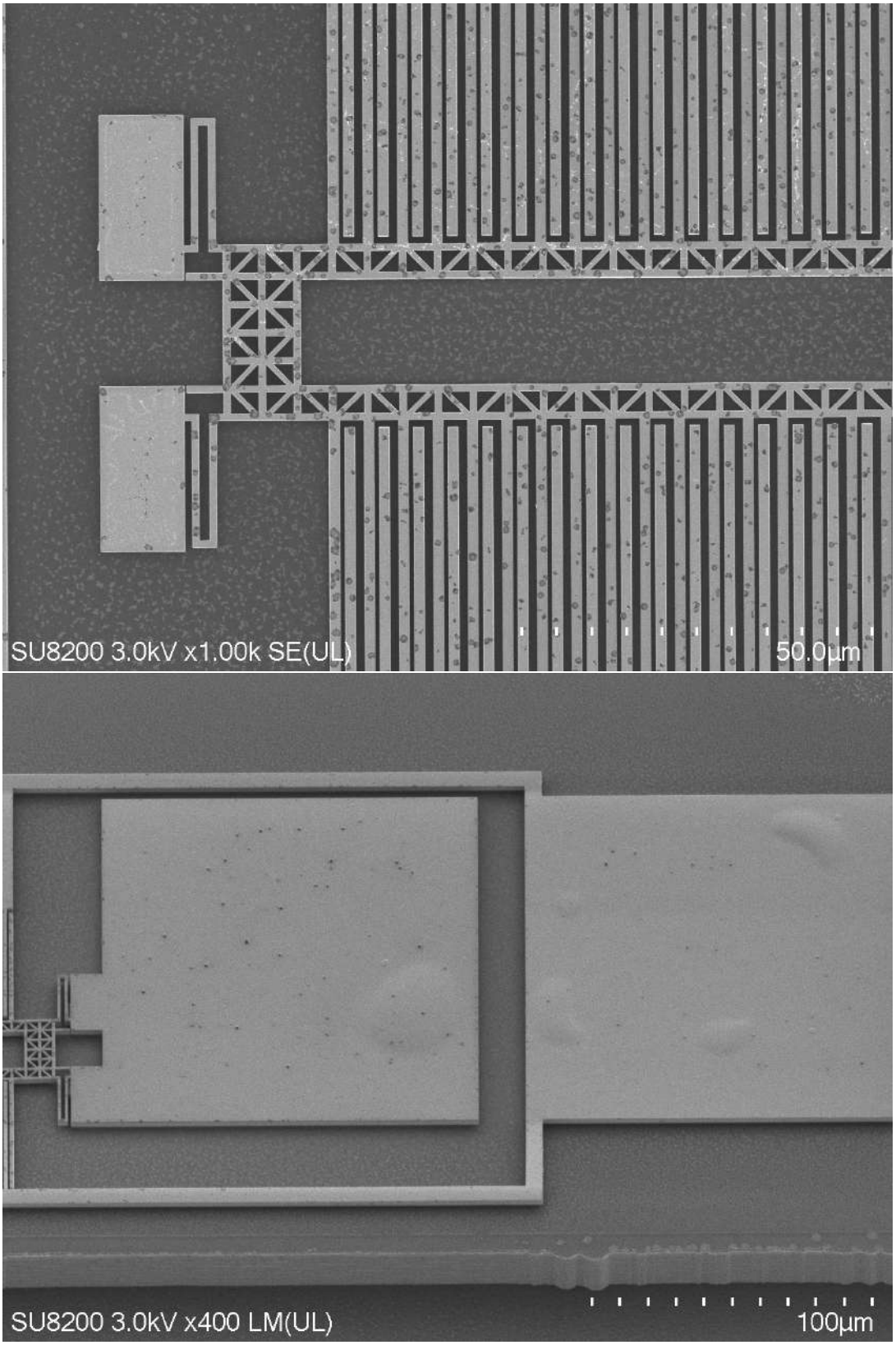

Figure 54: Following the vapor HF release step, SEM imaging reveals widespread black and white residues distributed fairly uniformly across the chip surface. Additionally, significant buckling of the platinum layer is observed in the electrode pad region, indicating possible mechanical stress or delamination.

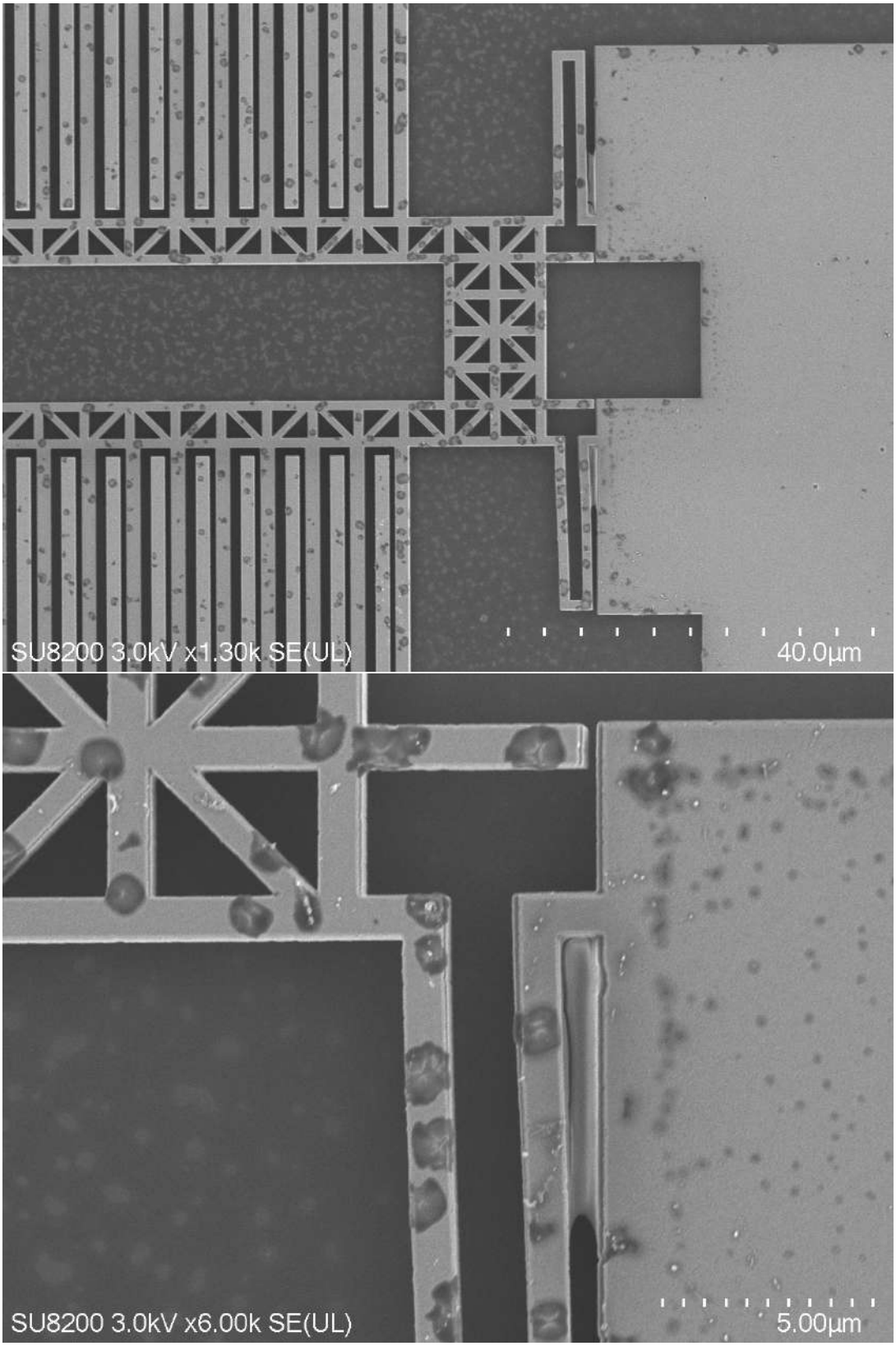

Figure 55: A close-up view of the MEMS structure's spring section reveals noticeable bending of the springs. Additionally, a greyish material bridging the spring and the electrode is visible. In the image below, careful inspection of the electrode pad edges shows the presence of a small gap , which may suggest either etching of the upper Pt-on-Ti layer or a possible delamination or slippage between the Ti and Pt layers on the silicon surface.

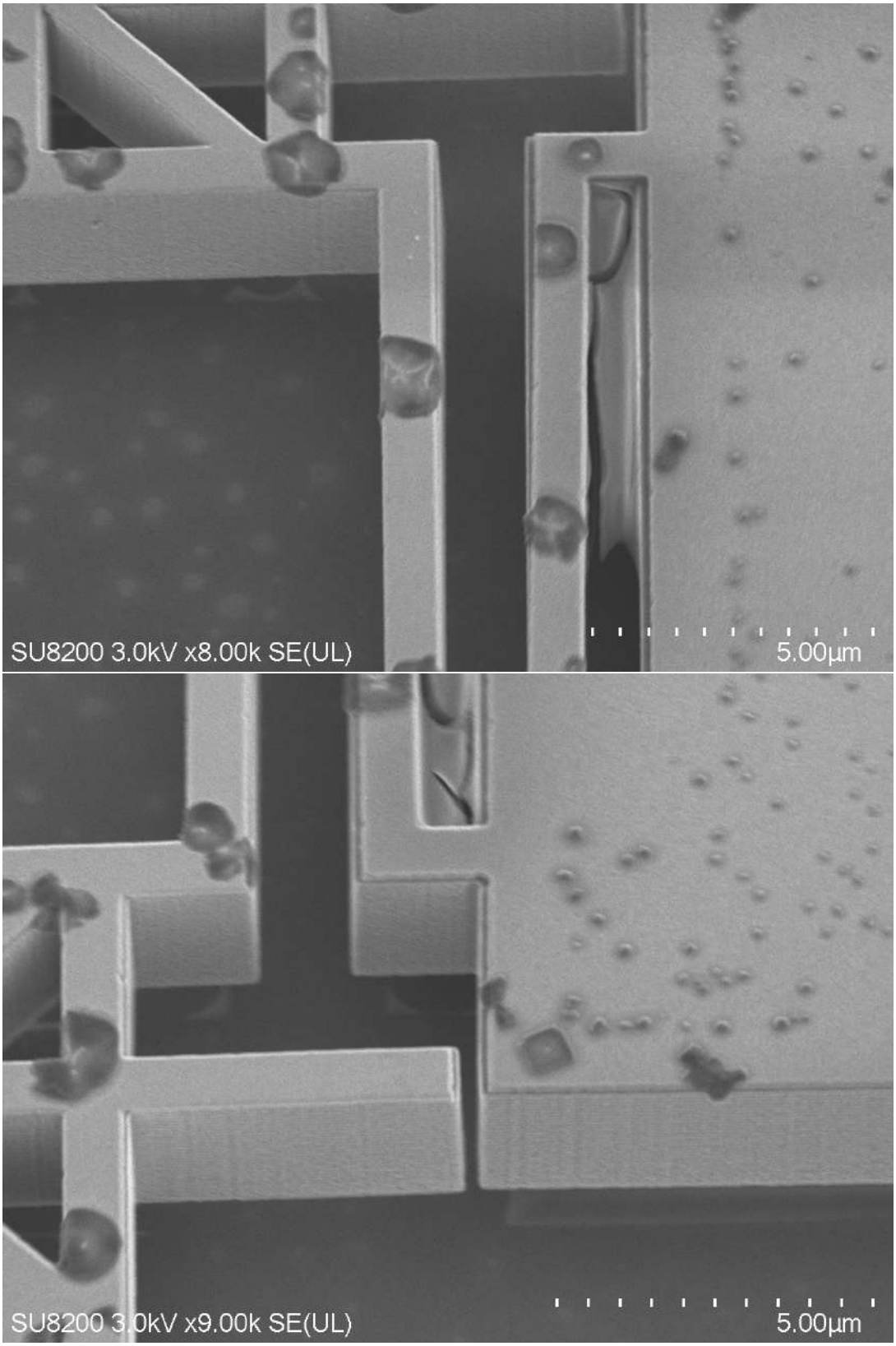

Figure 56: Close up image on the solid bridges section of the springs where the possible delamination can be seen more clearly. More importantly the black defects appear to be some sort of a residue which was accumulated or grown somehow.

First thing to note here is that the presence of Titanium as the adhesion layer on our

chip. In previous HF release trials where adhesion layer was still Titanium, no errors were encountered. However the current issue indicates that for the error-free recipe, a Titanium free structure should be used. Titanium is known to react with HF in the following way [38]

$$Ti + 3HF \rightarrow TiF_3 + \frac{3}{2}H_2$$

The etching of titanium with hydrofluoric acid HF results in the formation of titanium trifluoride TiF_3 and the release of hydrogen gas H_2.

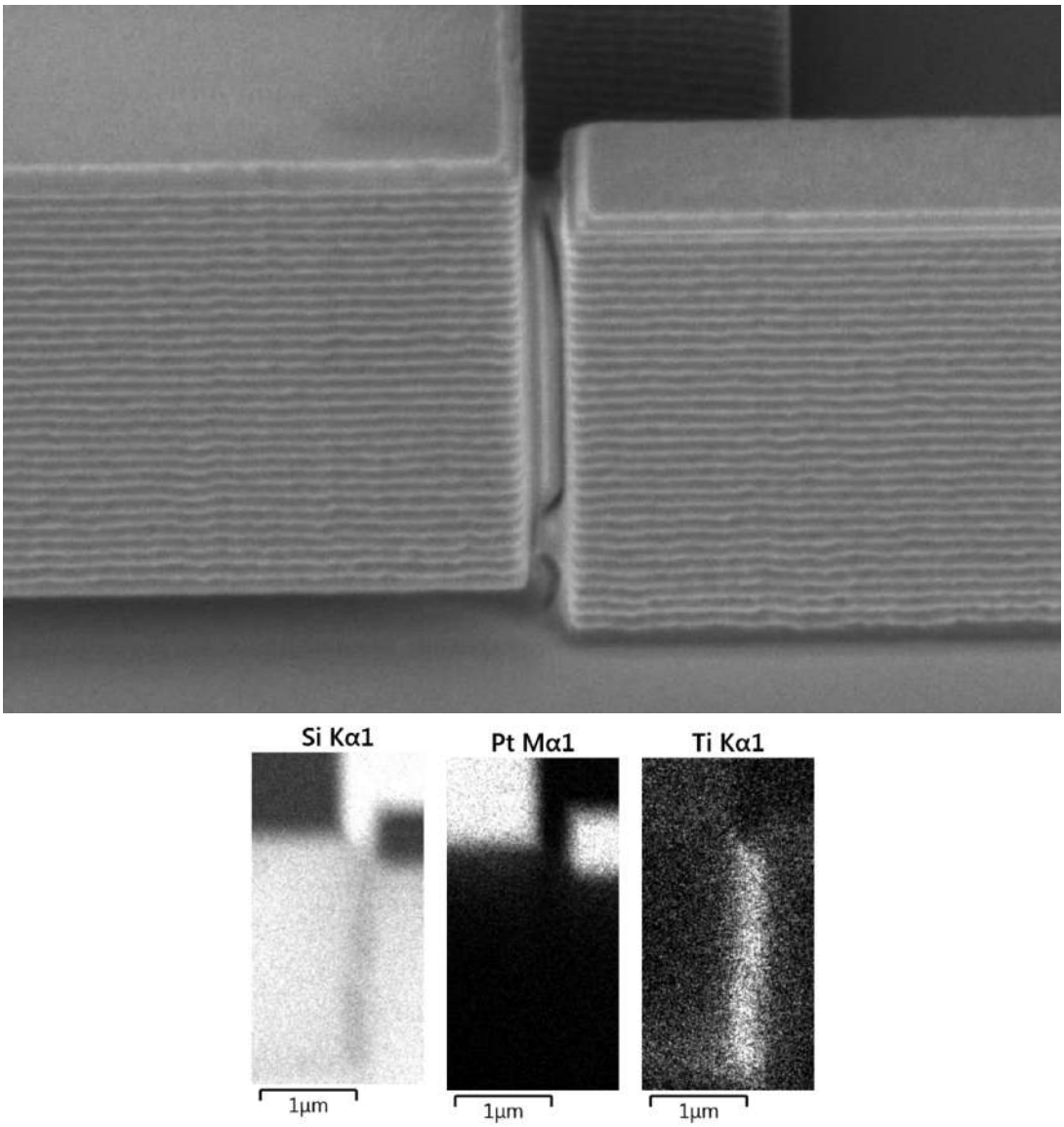

Figure 57: A close-up of the stopper structure shows the suspended element coming into contact with the electrode pad, effectively limiting further displacement. It appears that a solid bridge has formed at the contact point, effectively immobilizing the actuator and preventing any further movement.

An unexpected outcome is shown in the second image of the above figure, which presents an Energy Dispersive X-ray Spectroscopy (EDX) analysis used to determine the elemental composition of the materials. As anticipated, the characteristic X-ray signals

of silicon and platinum appear in their expected locations. In the case of silicon, there is no distinct absence (i.e., no sharp black line) at the gap area, which aligns with the presence of silicon behind the structure and at the handle layer surface.

Interestingly, titanium signals are detected within the stopper region, suggesting that titanium atoms may have migrated. This strongly implies that hydrofluoric acid (HF) has attacked the titanium layer, potentially forming compounds such as TiF_4 and H_2SiF_6. Unlike SiF_4 which is volatile and easily removed, these titanium- and silicon-based compounds are more stable and less volatile, likely leading to their accumulation and bridging within the structure. [39] Evading of this has been carried out by switching to Chromium as the adhesion layer.

4 Chapter 4 - Transmission over Carbon Nanotube using Nonequilibrium Green's Function Formalism

4.1 Introduction

As electronics continued to shrink in size, quantum effects became more significant, requiring device engineers to account for them in their designs.. Those such as nanowires, [40], next generation CMOS [41], next generation MOSFET [42], nanoscale transistors [43] were all simulated using the NEGF formalism, supplemented by the tight-binding method or density functional theory when appropriate. Therefore, in the realm of next-generation electronics—where quantum effects play a dominant role—quantum simulators become essential tools. The foundational developments of the nonequilibrium Green's function (NEGF) method trace back to the early 1960s, initiated by Schwinger [44], Kadanoff and Baym [45] and by Keldysh [46], where the Schwinger asked "Can one devise an action principle technique that is adapted to the direct computation of expectation values?". As early as 1961, it was recognized that accurately calculating nonequilibrium quantum expectation values at a given time t, based on their evolution from an earlier moment, required accounting for both forward and backward time evolution. This insight led to the formal definition of six distinct Green's functions. The next major advancement in the NEGF formalism came from the work of Kadanoff and Baym, who focused primarily on deriving quantum kinetic equations [47]. A significant milestone in applying NEGF to transport phenomena was the work by Caroli et al., which, for the first time, presented an explicit formula for the transmission coefficient expressed in terms of Green's functions. Within this formalism, it becomes possible to comprehensively and consistently handle multiple complex factors simultaneously. These include interactions between particles themselves, the influence of external driving forces or various perturbations applied to the system, as well as the coupling to environmental reservoirs or baths that possess an infinite number of degrees of freedom. By treating all these elements on an equal footing, the formalism provides a powerful and versatile framework for accurately modeling and understanding a wide range of quantum systems and their dynamics [48].

4.2 Implementation

In our case, we will be using the formalism to compute electron transmission over a carbon nanotube. Our implementation closely follows the description given by the works [49] [50] [51].

The way a simple model is constructed is by defining three regions of materials. First is the leads, second is the device region, third is the drain region, all of which are assumed to be part of the same carbon nanotube. The entire device is actually a tight binding model, where in the total Hamiltonian each atom is assumed to be connected to its nearest neighbors. In our case the Hamiltonian has a structure such that each row in the matrix should have always 3 non zero elements, which corresponds to the hexagonal lattice structure while assuming zero self energy of atoms. The transport of electrons is then computed by inputting this entire tight binding model.

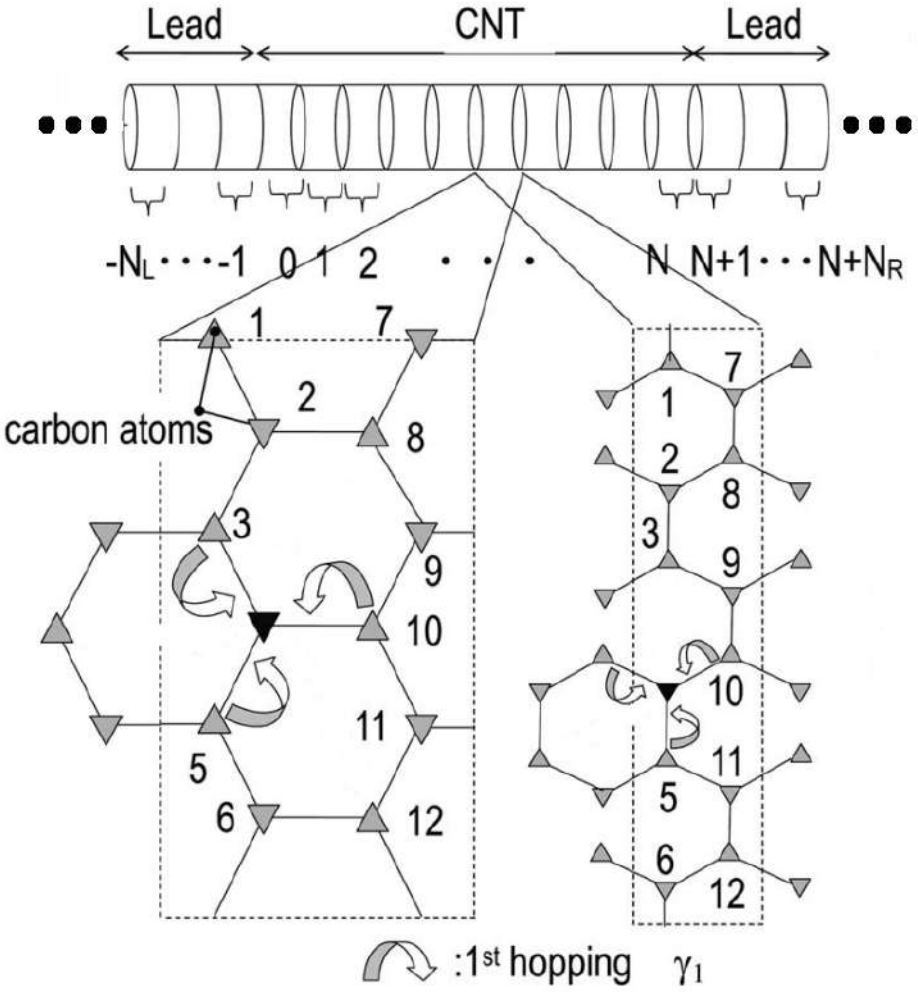

Figure 58: In the upper part of the figure, it can be seen the schematic shape of the carbon nanotube. It appears to be cut is segments, which is displayed below.

The segmented shape of the above model is again due to the way model is constructed. While the tight binding model of the carbon nanotube is built, the entire Hamiltonian is actually a tridiagonal block matrix. The down right part of the figure where, there are nodes of carbon atoms from 1 to 12 displays one block of the carbon nanotube.The left one display a zigzag type block and the right one displays armchair type block.

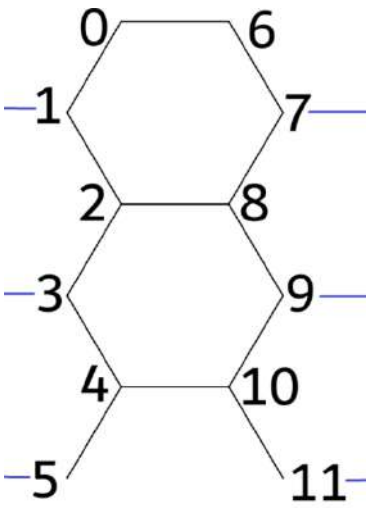

	0	1	2	3	4	5	6	7	8	9	10	11
0	0	-2.7	0	0	0	-2.7	-2.7	0	0	0	0	0
1	-2.7	0	-2.7	0	0	0	0	0	0	0	0	0
2	0	-2.7	0	-2.7	0	0	0	0	-2.7	0	0	0
3	0	0	-2.7	0	-2.7	0	0	0	0	0	0	0
4	0	0	0	-2.7	0	-2.7	0	0	0	0	-2.7	0
5	-2.7	0	0	0	-2.7	0	0	0	0	0	0	0
6	-2.7	0	0	0	0	0	0	-2.7	0	0	0	-2.7
7	0	0	0	0	0	0	-2.7	0	-2.7	0	0	0
8	0	0	-2.7	0	0	0	0	-2.7	0	-2.7	0	0
9	0	0	0	0	0	0	0	0	-2.7	0	-2.7	0
10	0	0	0	0	-2.7	0	0	0	0	-2.7	0	-2.7
11	0	0	0	0	0	0	-2.7	0	0	0	-2.7	0

	0	1	2	3	4	5	6	7	8	9	10	11
0	0	0	0	0	0	0	0	0	0	0	0	0
1	0	0	0	0	0	0	0	-2.7	0	0	0	0
2	0	0	0	0	0	0	0	0	0	0	0	0
3	0	0	0	0	0	0	0	0	0	-2.7	0	0
4	0	0	0	0	0	0	0	0	0	0	0	0
5	0	0	0	0	0	0	0	0	0	0	0	-2.7
6	0	0	0	0	0	0	0	0	0	0	0	0
7	0	0	0	0	0	0	0	0	0	0	0	0
8	0	0	0	0	0	0	0	0	0	0	0	0
9	0	0	0	0	0	0	0	0	0	0	0	0
10	0	0	0	0	0	0	0	0	0	0	0	0
11	0	0	0	0	0	0	0	0	0	0	0	0

Figure 59: Consider a zigzag nanotube composed of 12 atoms per unit block, as illustrated above. The matrix shown at the bottom left represents the tight-binding Hamiltonian for this unit block, corresponding to the node schematic displayed above. The blue lines extending from nodes 1, 3, 5, 7, 9, and 11 indicate the sites that facilitate electron hopping to the adjacent block. Also it can be seen that the node 0 is connected to node 5, which is needed due to the shape of the unit block which is a ring. Meanwhile, the matrix at the bottom right depicts the off-diagonal block that connects the current nanotube unit to the next one by establishing three hopping interactions between them. This off-diagonal matrix is placed in the lower diagonal position to represent the coupling from the right end of one block to the left end of the adjacent block. Because the Hamiltonian must be Hermitian, the conjugate transpose of this matrix is also included in the corresponding upper diagonal position. The number -2.7, which is in eV, in the entries is due to overlap energy of p orbital hybridization between carbon atoms.

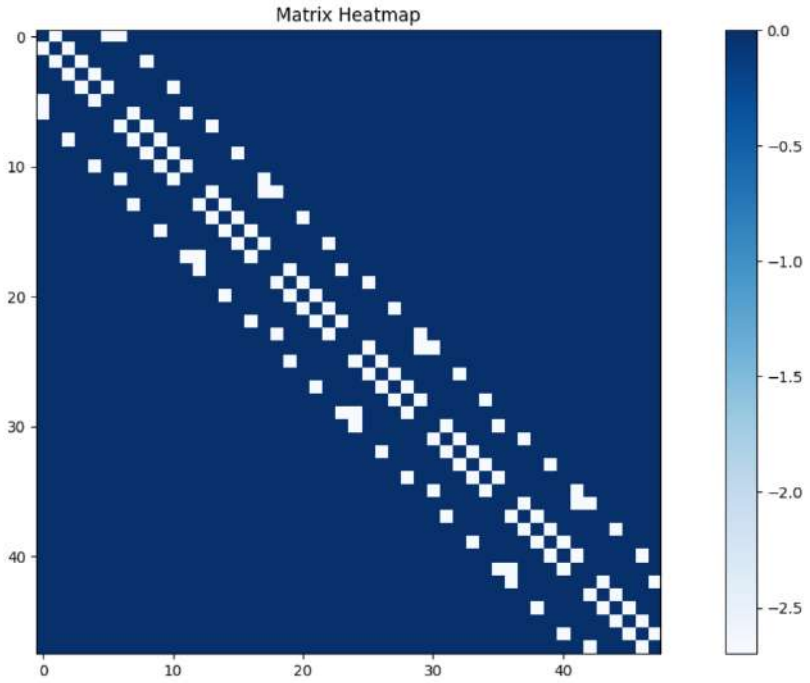

Figure 60: Total Hamiltonian of a carbon nanotube tight binding model with 4 connected blocks, each block having 12 atoms. White denotes value -2.7, blue denotes zero.

This way, after having the unit block of a nanotube of selected chirality and the corresponding off-diagonal block, one can construct a nanotube of any length easily by adding them consecutively along the diagonal and one off diagonal.

One can notice that the assumption of source and drain leads extending to infinity corresponds to infinite matrix, which is unusable in any way. The NEGF theory takes these infinite matrices into account by mathematically converting their presence at the ends of our device as additional energy.

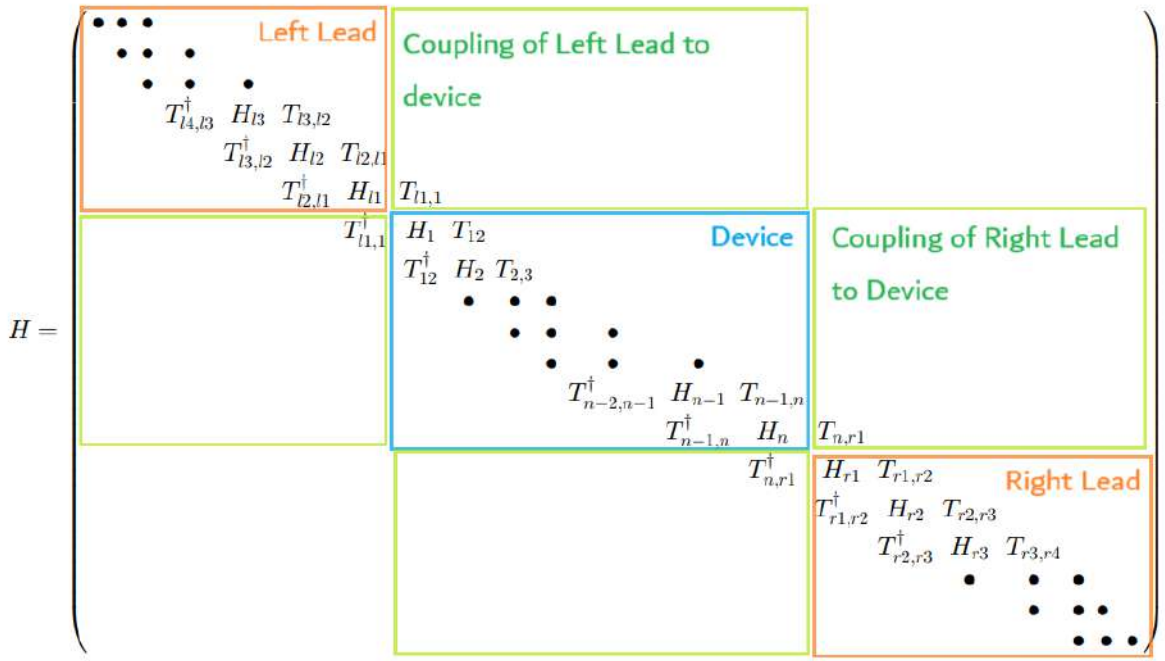

Figure 61: The Total Hamiltonian of infinite Right and Left Leads coupled to the Device. [49] In our simple model, all of the H's are the same H and all of the T's are the same T, which describes a uniform infinite carbon nanotube.

Employing the notation of the work [49], we have to calculate:

$$[A_{DD} - A_{DL}A_{LL}^{-1}A_{LD} - A_{DR}A_{RR}^{-1}A_{RD}]G_{DD} = I$$

Where $A = [EI - H]$, E being a scalar for energy, I being identity matrix, H being the total hamiltonian seen in above figure. This equation is solved order to find device greens function G_{DD}. However it can not be solved as the terms A_{LL}^{-1} and A_{RR}^{-1} are infinite dimensional. Important thing to notice is that for the calculation of the term $A_{DL}A_{LL}^{-1}A_{LD}$ or $A_{DR}A_{RR}^{-1}A_{RD}$ we only need the right bottom term of the matrix A_{LL}^{-1} and the top left term of the matrix A_{RR}^{-1}, due to the shape of the sparse matrices A_{DL},A_{DR},A_{LD} and A_{RD}. Naive approach is to construct a big matrix for both of them then invert it, which is costly, then take the selected term. However this approach is inefficient and does not converge fast. Instead one must employ the Sancho-Rubio method [52]. This method couples 2^n layers after n iterations, therefore it is exponentially faster. Considering again that our diagonal matrices are H and on off diagonals are T, the algorithm is the :

$$\epsilon_L^{(0)} = H \quad \text{(Left surface, } \epsilon_i^s\text{)} \tag{1}$$
$$\tilde{\epsilon}_R^{(0)} = H \quad \text{(Dual/right surface, } \tilde{\epsilon}_i^s\text{)} \tag{2}$$
$$\epsilon_B^{(0)} = H \quad \text{(Device)} \tag{3}$$
$$\alpha^{(0)} = T \quad \text{(Forward hopping)} \tag{4}$$
$$\beta^{(0)} = T^\dagger \quad \text{(Backward hopping)} \tag{5}$$
$$E_c = E + i\eta \quad \text{(Scalar complex value)} \tag{6}$$
$$\mathbb{E} = E_c \cdot \mathbb{I} \quad \text{(Identity matrix scaled with selected energy)} \tag{7}$$
$$\tag{8}$$

In literature, the energy contributions coming from the infinite leads which are folded back into the finite device Hamiltonian are also called surface greens energy.

The algorithm then iterates over the code below until a desired convergence is reached.

$$g_0^{(i)} = \left(\mathbb{E} - \epsilon_B^{(i)}\right)^{-1} \tag{9}$$
$$g_a^{(i)} = g_0^{(i)} \alpha^{(i)} \tag{10}$$
$$g_b^{(i)} = g_0^{(i)} \beta^{(i)} \tag{11}$$
$$A^{(i)} = \alpha^{(i)} g_b^{(i)} \tag{12}$$
$$B^{(i)} = \beta^{(i)} g_a^{(i)} \tag{13}$$
$$\epsilon_L^{(i+1)} = \epsilon_L^{(i)} + A^{(i)} \tag{14}$$
$$\tilde{\epsilon}_R^{(i+1)} = \tilde{\epsilon}_R^{(i)} + B^{(i)} \tag{15}$$
$$\epsilon_B^{(i+1)} = \epsilon_B^{(i)} + A^{(i)} + B^{(i)} \tag{16}$$
$$\alpha^{(i+1)} = \alpha^{(i)} g_a^{(i)} \tag{17}$$
$$\beta^{(i+1)} = \beta^{(i)} g_b^{(i)} \tag{18}$$

Finally we set

$$G_{LL}(E)_{00} = \left(\mathbb{E} - \epsilon_L^{(i)}\right)^{-1} \qquad \text{(Right bottom term of Left surface)} \tag{19}$$
$$G_{DD}(E) = \left(\mathbb{E} - \epsilon_B^{(i)}\right)^{-1} \qquad \text{(Device)} \tag{20}$$
$$G_{RR}(E)_{2^i 2^i} = \left(\mathbb{E} - \tilde{\epsilon}_R^{(i)}\right)^{-1} \qquad \text{(Top left term Right surface)} \tag{21}$$

Where $2^i 2^i$ indicates the row and column indexes of the matrix. The exponential scaling nature of the algorithm is seen from this expression. With this in hand, we define the following:

$$\Sigma_{\text{lead}1,1} = T^\dagger \, G_{LL}(E)_{00} \, T = \Sigma_L \tag{119}$$
$$\Sigma_{\text{lead}n,n} = T \, G_{RR}(E)_{2^i 2^i} \, T^\dagger = \Sigma_R \tag{22}$$

and the following expressions:

$$\Gamma_L(E) = -2 \, Imaginary \left[\Sigma_L(E)\right] \tag{137}$$
$$\Gamma_R(E) = -2 \, Imaginary \left[\Sigma_R(E)\right] \tag{23}$$

then,

$$\tilde{\Gamma}_L^{1;1} = \Gamma_L \tag{24}$$
$$\tilde{\Gamma}_R^{n;n} = \Gamma_R \tag{25}$$

where the $\tilde{\Gamma}$ matrix is a zero matrix with the same dimensions as our device hamiltonian. Furthermore, 1;1 means that we set the first block on top left of the matrix where we set to Γ_L, n;n means the the first block on bottom right of the matrix where we set to Γ_R.

Ultimately we reach the famous Caroli formula.

$$T(E) = \mathrm{Tr}\left[\tilde{\Gamma}_L(E)\, G_{DD}(E)\, \tilde{\Gamma}_R(E)\, G^{\dagger}_{DD}(E)\right] \tag{26}$$

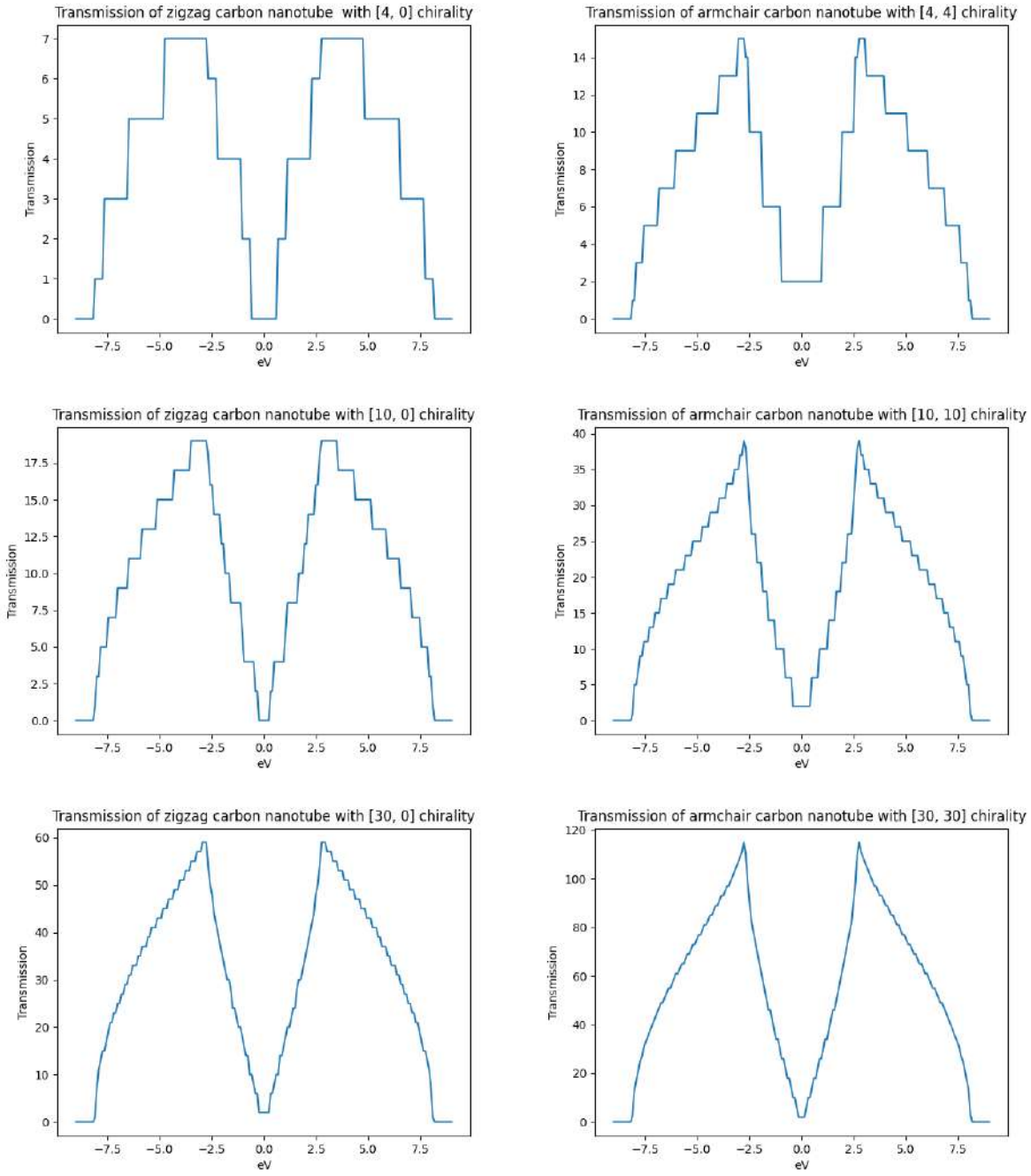

Figure 62: The Transmission plots of nanotubes with various chiralities. The band maximum and minimum is at energies +3t and -3t. In the case where t is taken -2.7eV, those maximum and minimum can be found at ±8.1eV, as it can be seen from the plots.

The effect of gating by applying voltage to the gate electrode just as it is done in field effect transistors, can be incorporated by adding onsite energies to the selected nodes of the device. In the following plots, onsite energy of one ring was increased by given eV.

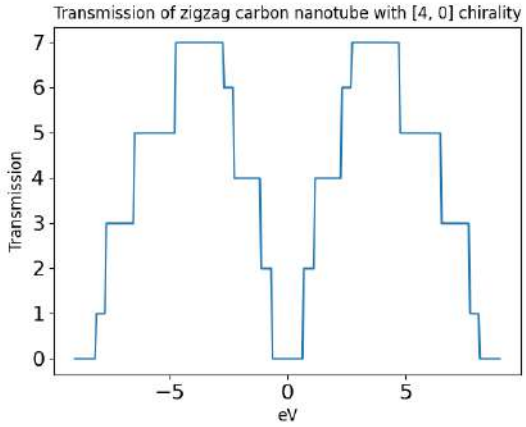

(a) 0 gating.

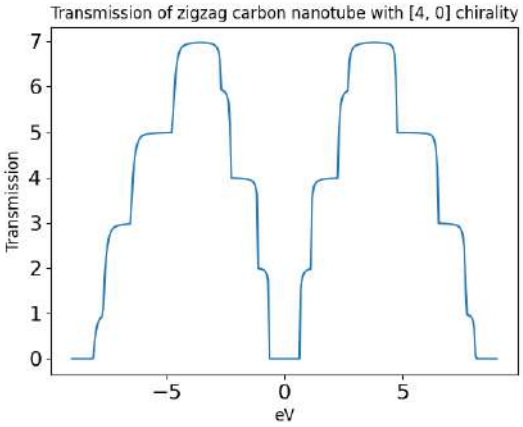

(b) Gated with 0.2 eV

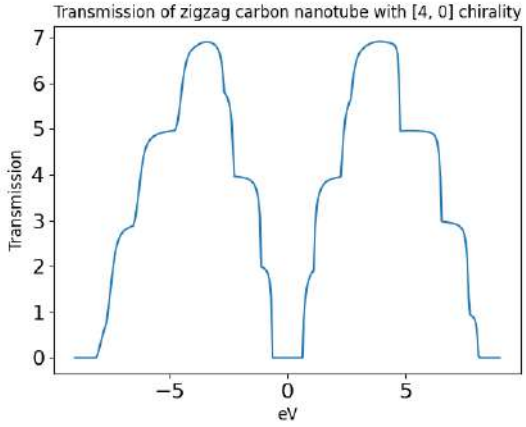

(c) Gated with 0.4 eV

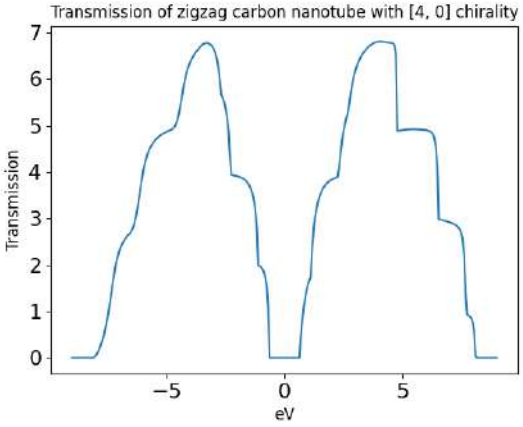

(d) Gated with 0.6 eV

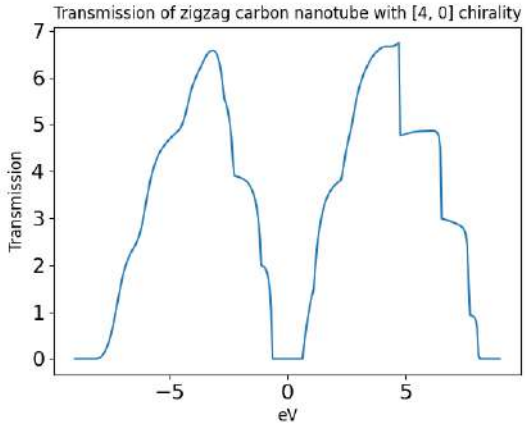

(e) Gated with 0.8 eV

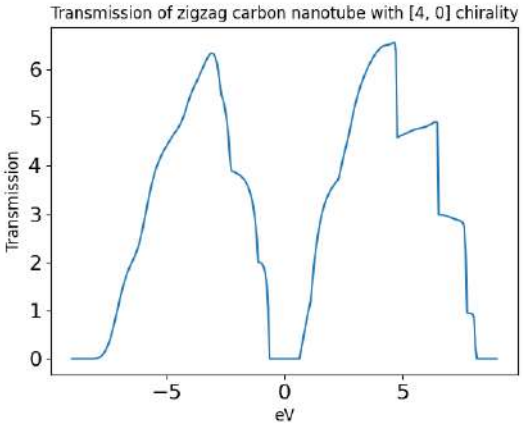

(f) Gated with 1 eV

Figure 63: Applying a gate voltage up to 1V initially smooths the transmission curve, but starting around 0.6V, it begins to distort the overall shape. The transmission in the negative energy range is more strongly affected than in the positive range, since the tunneling probability decreases more significantly when the gate barrier surpasses the particle energy in that region.

4.3 Effect of Strain on Nanotube Band Gap

To simulate the bandgap change in a strained carbon nanotube, we analyzed the transmission spectra. The region of zero transmission near 0eV indicates the absence of electronic states, confirming that the nanotube is semiconducting. This observation is consistent with the known semiconducting nature of zigzag nanotubes. The width of this zero-transmission plateau corresponds to the bandgap size and its variation under strain reflects changes in the bandgap.

To model the strain, we used the expression provided in Section 2.2,

$$t = t^{(0)}(\frac{d_0}{d})^2$$

where the $t^{(0)}$ is the original hopping parameter,d_0 is the original bond length and d is the new bond length. The change in the hopping parameter is determined by the variation in atomic bond length, which is determined by the positions of the carbon atoms of strained nanotube.

To determine the atomic positions in a strained carbon nanotube, molecular dynamics simulations are typically employed to capture atomic rearrangements under applied strain. However, to begin with a simplified model, we considered a zigzag nanotube with tuned bonds. In this approach, strain is introduced by adjusting the hopping parameters of the bonds aligned with the tube's axis.

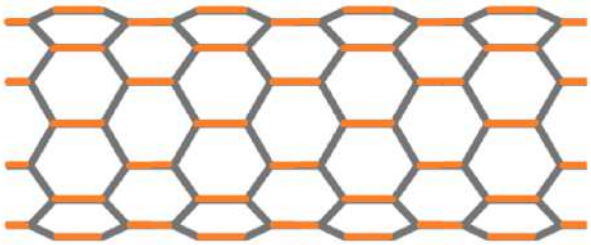

Figure 64: In our model, the bonds colored in orange are tuned according to $t = t^{(0)}(\frac{d_0}{d})^2$, rest of the hopping parameters are left the same.

Below the transmissions were plotted for each straining 0, 2, 4, 6, 8 and 10 percent. Since x% straining means $d = d_0(1 + x)$, new hopping parameter is $t = t^{(0)}(1/1 + x)^2$ when x is the straining percentage. The constructed device segment in this case is [16,0] zigzag nanotube with 10 unit ring cells, where each ring cell has 32 atoms giving a total of 320 atom device.

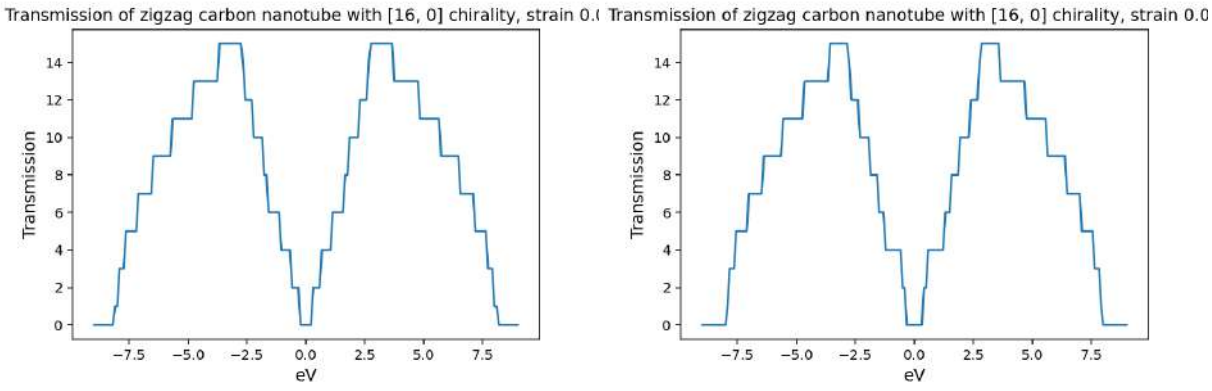

(a) 0% straining.

(b) 2% straining.

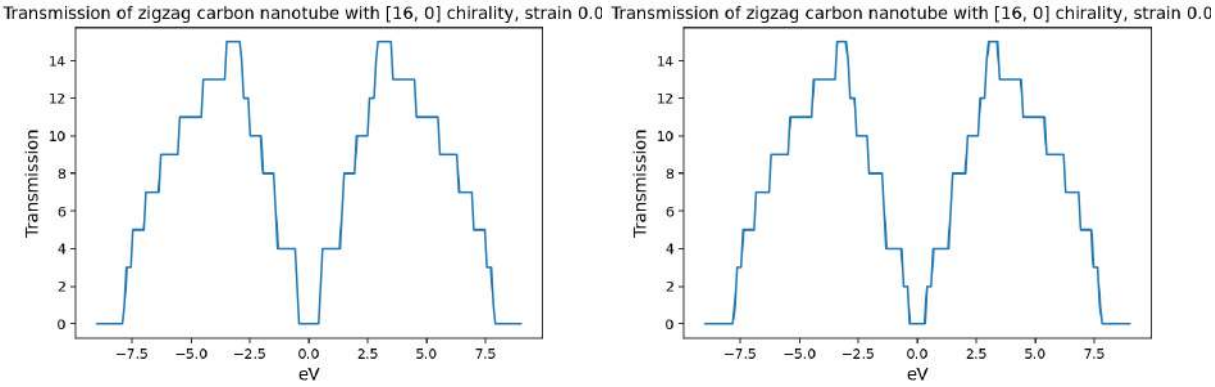

(c) 4% straining.

(d) 6% straining.

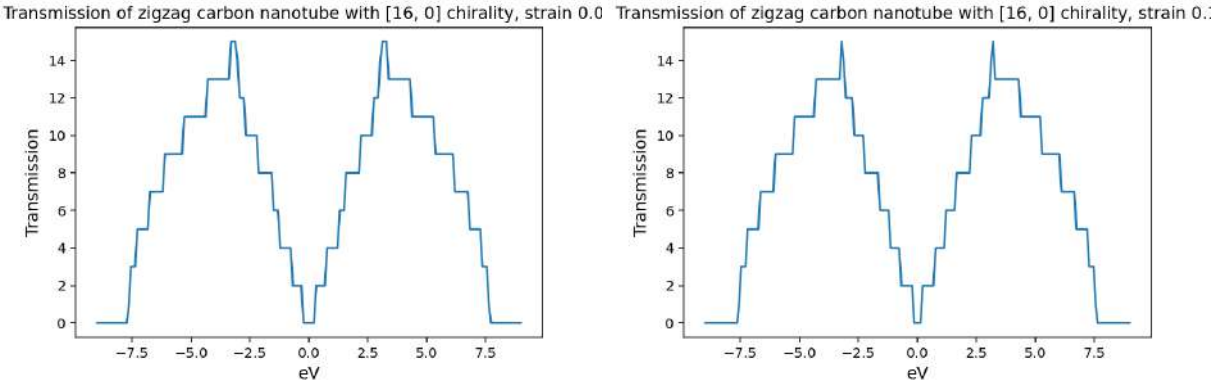

(e) 8% straining.

(f) 10% straining.

Figure 65: Transmission plots of strained carbon nanotube with [16,0] chirality with 10 unit ring cells.

Computing the band gaps from these plots sweeping the straining from 0 to 10 with 0.005 increments, we have the following plot.

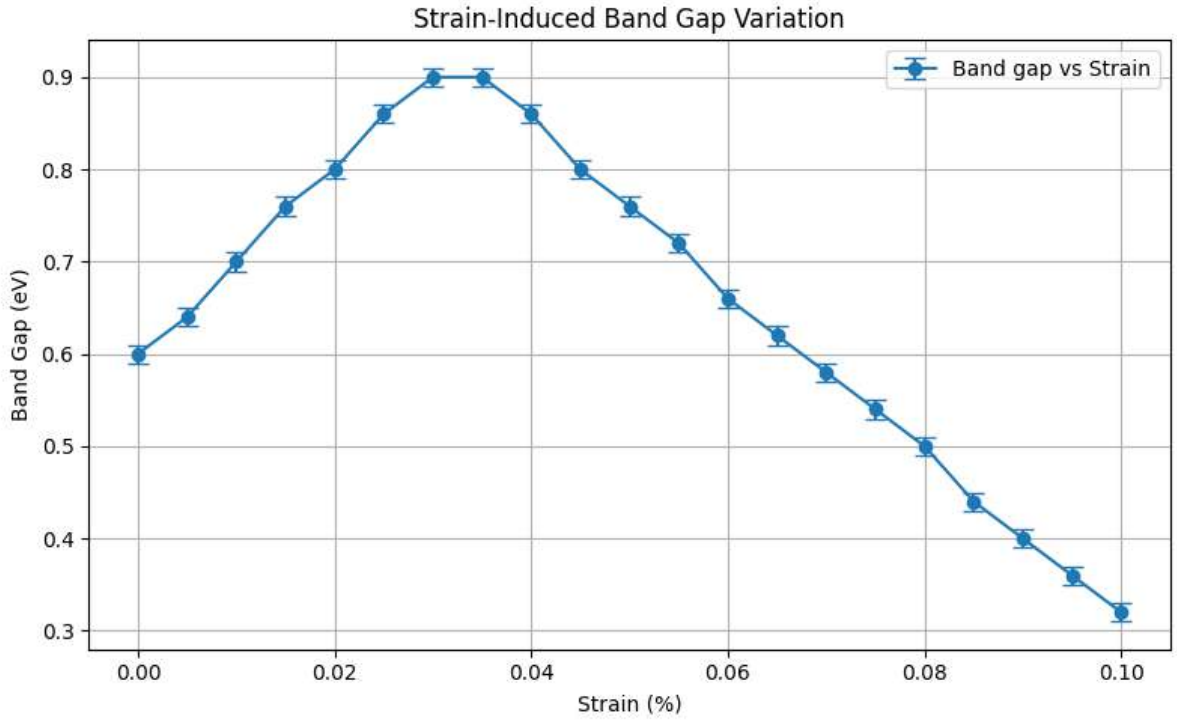

Figure 66: Band Gap (eV) versus Straing (%) plot of [16,0] chiral, 10 unit ring cell tube.

It is surprising to see that the band gap of nanotube has two seemingly linear slopes first increasing up to 3.5% straining, then begins to decline with again a linear behavior.

By directly solving for the bands of the device Hamiltonian, a much more accurate plot can be obtained. The way to obtain eigenvalues is by noting the symmetric block diagonal structure of the Total Hamiltonian. Solving the eigenvalues of the matrix for each k value in the below code gives the bandstructure.

For k between [-π, π] :

Solve eigenvalues of the matrix

$$T \cdot e^{-ik} + H + T^{\dagger} \cdot e^{-ik}$$

Plotting of the k versus eigenvalues plot gives the following for [16,0] chiral tube.

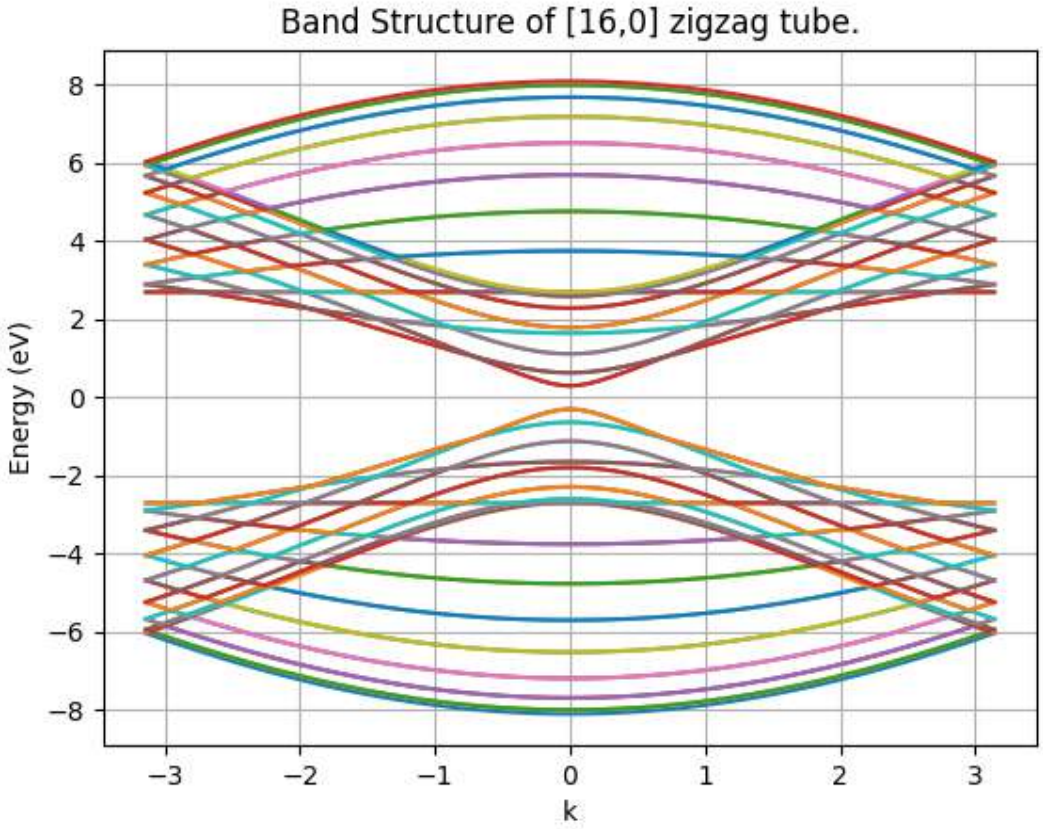

Figure 67: Electron bands of [16,0] zigzag nanotube.

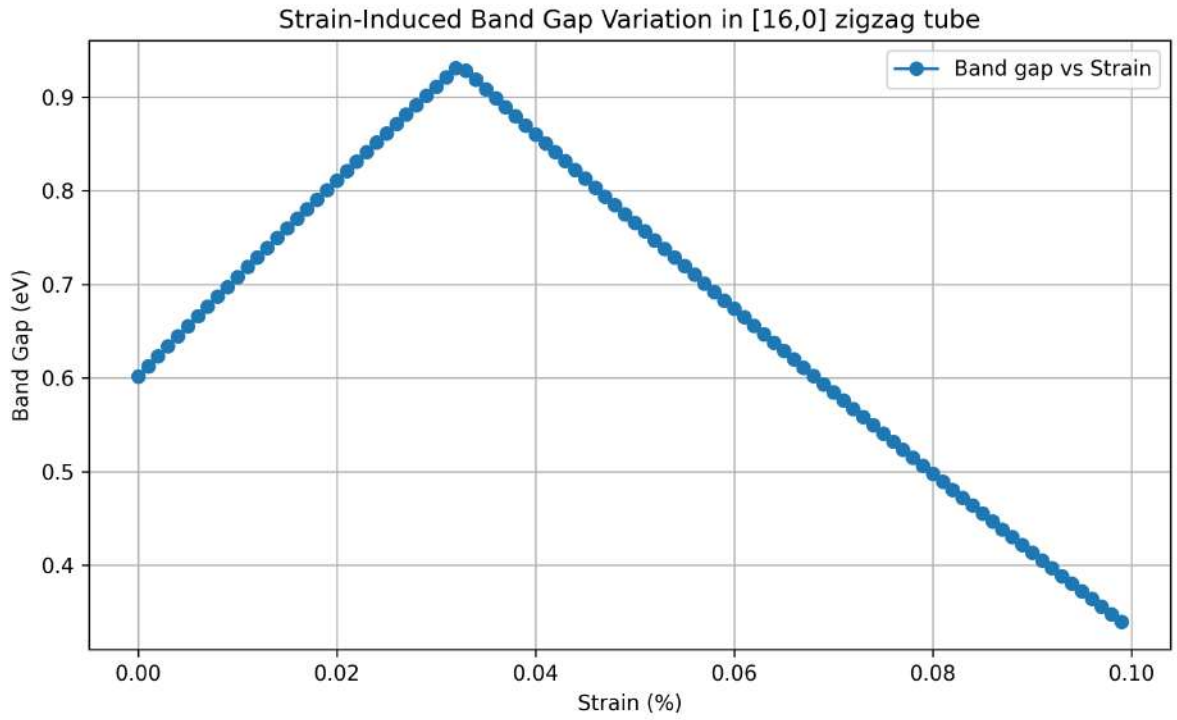

Figure 68: Band Gap (eV) versus Strain (%)of [16,0] zigzag nanotube. The kink around 3% strain is caused by two bands crossing each other, one band rises, while the other drops as strain is increased. The kink appears at the point where the minima of the two bands intersect.

A similar behavior has also been reported in the study cited study [53]. In their work, the authors analytically investigate the energy levels of carbon nanotubes subjected to mechanical strain, using a theoretical model that closely resembles the approach adopted in our study. Specifically, they apply strain by adjusting the interatomic bond lengths, which leads to a corresponding modification in the hopping parameters within the tight-binding Hamiltonian approach that parallels our method of modeling the influence of strain. Their analytical treatment and scaling of hopping terms follow the same functional form we have used to reflect bond elongation effects on electronic structure.

Notably, our results are in strong agreement with their findings. Both studies observe that the variation of the band gap due to strain is significantly more pronounced in zigzag-type carbon nanotubes compared to armchair configurations. The authors of the referenced work explain that this is because zigzag nanotubes are typically semiconducting, and thus their band structure is more sensitive to changes in atomic spacing caused by strain. In contrast, armchair nanotubes are intrinsically metallic and possess no band gap in their unstrained state. As a result, applying strain has a negligible effect on their electronic properties, at least in terms of opening a band gap. This corroborates our observations and strengthens the validity of using a simplified hopping-parameter-based strain model to capture the key qualitative trends in strained carbon nanotube band structures.

5 Chapter 5 - Discussion

The MEMS actuator design, validated using COMSOL simulations, confirmed the capability of achieving displacements up to 200 nm—sufficient for straining CNTs up to 10%, which is near the physical limit of CNTs. However, practical realization of this strain was hampered by fabrication defects, most notably those introduced during the vapor HF release and DRIE etching processes. As a result, the complete device with a transferred nanotube has not yet been successfully achieved.

The core aim—to study the modulation of the CNT band gap through mechanical strain—was validated both computationally and conceptually. Simulation results using the tight-binding NEGF formalism demonstrated band gap modulation behavior consistent with literature, particularly the strong strain sensitivity observed in zigzag CNTs as compared to armchair types. This aligns with theoretical expectations: semiconducting zigzag CNTs exhibit pronounced changes in their electronic structure under axial strain, while metallic armchair CNTs remain largely unaffected due to the absence of a band gap in their unstrained state.

Overall, this on-chip device for straining carbon nanotubes can serve as a versatile platform for a wide range of future studies. One potential application is in the functionalization of nanotubes, where the impact of attached compounds on properties such as band structure, electronic transmission, quantum dot characteristics, or mechanical behavior can be examined. For instance, the study [54] suggests that functionalizing single-walled carbon nanotubes with oxygen reduces mechanical properties like Young's modulus, stress, strain, and toughness as the degree of functionalization increases. Our setup is well-suited for conducting quantitative experiments on electronic transport, quantum dot phenomena, or the interplay between strain and functionalization.

Another study [55] conducted Raman spectroscopy on carbon nanotubes, focusing on two key features: the radial breathing mode (RBM) and the G-band. Their results showed that while the RBM remained unchanged under strain, the G-band exhibited a downward shift in frequency with increasing uniaxial strain in single-walled carbon nanotubes (SWNTs). Our approach is well-suited for such investigations. Applying strain to nanotubes to modulate phonon bands—and consequently, electron-phonon interactions—could provide valuable insights, particularly in exploring the predicted Peierls transition in carbon nanotubes.

The ability to dynamically tune the bandgap also opens the door to next-generation photodetector technologies. As demonstrated in [56], applying uniaxial strain to their carbon nanotube intramolecular junction photodetector led to a continuous blueshift in the peak responsivity wavelength. This shift reflects a corresponding increase in the bandgap of the carbon nanotubes. Since our setup allows bandgap tuning through applied strain, we can consequently achieve tunable peak responsivity in a photodetector.

The proposed MEMS actuator chip, designed to offer precise control over the targeted molecular junction, in this case carbon nanotubes, will grant us another knob to tune. By enabling the tuning of the bandgap and lattice structure, this technology contributes to the broader field of Hamiltonian engineering, where we are beginning to manipulate the most fundamental elements of the universe. Gaining advanced control over the parameters that define a system's Hamiltonian paves the way for the development of revolutionary quantum devices.

6 References

References

[1] https://cnanotube.com/comprehensive-guide-to-the-characterization-of-carbon-nanotubes/.

[2] https://tuball.com/articles/multi-walled-carbon-nanotubes.

[3] Sumio Iijima. Helical microtubules of graphitic carbon. *Nature*, 354(6348):56–58, November 1991. Publisher: Nature Publishing Group.

[4] T. W. Ebbesen, H. J. Lezec, H. Hiura, J. W. Bennett, H. F. Ghaemi, and T. Thio. Electrical conductivity of individual carbon nanotubes. *Nature*, 382(6586):54–56, July 1996.

[5] E.J. Pavlina and C.J. Van Tyne. Correlation of Yield Strength and Tensile Strength with Hardness for Steels. *Journal of Materials Engineering and Performance*, 17(6):888–893, December 2008.

[6] P. Kim, L. Shi, A. Majumdar, and P. L. McEuen. Thermal Transport Measurements of Individual Multiwalled Nanotubes. *Physical Review Letters*, 87(21):215502, October 2001.

[7] https://spectrum.ieee.org/chip-hall-of-fame-texas-instruments-digital-micromirror-device.

[8] https://www.empa.ch/web/s604/snsf-scientific-image-competition-2025.

[9] E. D. Minot, Yuval Yaish, Vera Sazonova, Ji-Yong Park, Markus Brink, and Paul L. McEuen. Tuning Carbon Nanotube Band Gaps with Strain. *Physical Review Letters*, 90(15):156401, April 2003. Publisher: American Physical Society.

[10] Jaeyong Lee, Soonjae Pyo, Dae-Sung Kwon, Eunhwan Jo, Wondo Kim, and Jongbaeg Kim. Ultrasensitive Strain Sensor Based on Separation of Overlapped Carbon Nanotubes. *Small*, 15(12):1805120, 2019. _eprint: https://onlinelibrary.wiley.com/doi/pdf/10.1002/smll.201805120.

[11] Jamie H. Warner, Neil P. Young, Angus I. Kirkland, and G. Andrew D. Briggs. Resolving strain in carbon nanotubes at the atomic level. *Nature Materials*, 10(12):958–962, December 2011. Publisher: Nature Publishing Group.

[12] S. Paulson, M. R. Falvo, N. Snider, A. Helser, T. Hudson, A. Seeger, R. M. Taylor, R. Superfine, and S. Washburn. *In situ* resistance measurements of strained carbon nanotubes. *Applied Physics Letters*, 75(19):2936–2938, November 1999.

[13] Yuli V. Nazarov. *Quantum Transport: Introduction to Nanoscience.*

[14] https://ocw.tudelft.nl/wp-content/uploads/lecture7-8-mesophy.pdf.

[15] J. M. Thijssen and H. S. J. Van Der Zant. Charge transport and single-electron effects in nanoscale systems. *physica status solidi (b)*, 245(8):1455–1470, August 2008.

[16] Pablo Jarillo-Herrero. *Quantum Transport in Carbon Nanotubes*. PhD thesis, Delft University of Technology.

[17] Mildred S. Dresselhaus, Gene Dresselhaus, and Phaedon Avouris. *Carbon Nanotubes: Synthesis, Structure, Properties, and Applications*. Number 80 in Topics in Applied Physics. Springer, Berlin Heidelberg, 2001.

[18] https://en.wikipedia.org/wiki/graphene.

[19] Victor L. Pushparaj, Lijie Ci, Subbalakshmi Sreekala, Ashavani Kumar, Sai Kesapragada, Daniel Gall, Omkaram Nalamasu, Ajayan M. Pulickel, and Jonghwan Suhr. Effects of compressive strains on electrical conductivities of a macroscale carbon nanotube block. *Applied Physics Letters*, 91(15):153116, October 2007.

[20] Dolores Bozovic, M. Bockrath, Jason H. Hafner, Charles M. Lieber, Hongkun Park, and M. Tinkham. Plastic deformations in mechanically strained single-walled carbon nanotubes. *Physical Review B*, 67(3):033407, January 2003. Publisher: American Physical Society.

[21] Marco Buongiorno Nardelli, B. I. Yakobson, and J. Bernholc. Mechanism of strain release in carbon nanotubes. *Physical Review B*, 57(8):R4277–R4280, February 1998. Publisher: American Physical Society.

[22] R. Heyd, A. Charlier, and E. McRae. Uniaxial-stress effects on the electronic properties of carbon nanotubes. *Physical Review B*, 55(11):6820–6824, March 1997.

[23] W. A. Harrison. *Electronic Structure and Properties of Solids*.

[24] Jia-Shiang Chen, Kasidet Jing Trerayapiwat, Lei Sun, Matthew D. Krzyaniak, Michael R. Wasielewski, Tijana Rajh, Sahar Sharifzadeh, and Xuedan Ma. Long-lived electronic spin qubits in single-walled carbon nanotubes. *Nature Communications*, 14(1):848, February 2023. Publisher: Nature Publishing Group.

[25] Paul L. McEuen, Marc Bockrath, David H. Cobden, Young-Gui Yoon, and Steven G. Louie. Disorder, Pseudospins, and Backscattering in Carbon Nanotubes. *Physical Review Letters*, 83(24):5098–5101, December 1999.

[26] Jonah Waissman, Maayan Honig, Sharon Pecker, Avishai Benyamini, Assaf Hamo, and Shahal Ilani. Realization of Pristine and Locally-Tunable One-Dimensional Electron Systems in Carbon Nanotubes. *Nature Nanotechnology*, 8(8):569–574, August 2013. arXiv:1302.2921 [cond-mat].

[27] Sami Sapmaz, Pablo Jarillo-Herrero, Leo P Kouwenhoven, and Herre S J Van Der Zant. Quantum dots in carbon nanotubes. *Semiconductor Science and Technology*, 21(11):S52–S63, November 2006.

[28] Zhihong Chen, Joerg Appenzeller, Joachim Knoch, Yu-ming Lin, and Phaedon Avouris. The Role of MetalNanotube Contact in the Performance of Carbon Nanotube Field-Effect Transistors. *Nano Letters*, 5(7):1497–1502, July 2005.

[29] Arash Kheyraddini Mousavi, Seyedhamidreza Alaie, and Zayd Chad Leseman. Basic MEMS Actuators. In Bharat Bhushan, editor, *Encyclopedia of Nanotechnology*, pages 1–16. Springer Netherlands, Dordrecht, 2016.

[30] Jun Mizuno. A Novel MEMS Actuator Driven with a Low DC Voltage. *Sensors and Materials*, 35(8):2909, August 2023.

[31] W Wai-Chi, A A Azid, and B Y Majlis. Formulation of stiffness constant and effective mass for a folded beam.

[32] R. J. Benham, C. G. Armstrong, and C. G. Drawford. *Mechanics of Engineering Materials*. Prentice Hall, Ltd., UK, 1996.

[33] Jonathan W. Wittwer and Larry L. Howell. Mitigating the Effects of Local Flexibility at the Built-In Ends of Cantilever Beams. *Journal of Applied Mechanics*, 71(5):748–751, September 2004.

[34] Lee Walter. Photoresist Damage in Reactive Ion Etching Processes. *Journal of The Electrochemical Society*, 144(6):2150, June 1997. Publisher: IOP Publishing.

[35] Wayne M. Moreau. *Semiconductor Lithography: Principles, Practices, and Materials*.

[36] Pradeep Dixit and Jianmin Miao. Effect of SF_6 flow rate on the etched surface profile and bottom grass formation in deep reactive ion etching process. *Journal of Physics: Conference Series*, 34:577–582, April 2006.

[37] https://www.epfl.ch/research/facilities/cmi/equipment/etching/spts-uetch/.

[38] Jeff Schroeffel. Etching Titanium with HF and Nitric Acid Solutions Part 1.

[39] https://en.wikipedia.org/wiki/titanium$_{t}etrafluoride$.

[40] Mathieu Luisier and Gerhard Klimeck. Atomistic full-band simulations of silicon nanowire transistors: Effects of electron-phonon scattering. *Physical Review B*, 80(15):155430, October 2009.

[41] Aryan Afzalian. Ab-initio NEGF Perspective of Ultra-Scaled CMOS: From 2D-material Fundamentals to Novel Dynamically-Doped Transistors. *npj 2D Materials and Applications*, 5(1):5, January 2021. arXiv:2010.06867 [physics].

[42] A. Svizhenko, M. P. Anantram, T. R. Govindan, B. Biegel, and R. Venugopal. Two-dimensional quantum mechanical modeling of nanotransistors. *Journal of Applied Physics*, 91(4):2343–2354, February 2002.

[43] Gennady Mil'nikov, Jun-ichi Iwata, Nobuya Mori, and Atsushi Oshiyama. RSDFT-NEGF transport simulations in realistic nanoscale transistors. *Journal of Computational Electronics*, 22(5):1181–1201, October 2023.

[44] J. Schwinger. Brownian motion of a quantum oscillator. *Journal of Mathematical Physics*, 2(3):407–432, 1961.

[45] L. P. Kadanoff and G. Baym. *Quantum Statistical Mechanics*. W. A. Benjamin, Inc, New York, 1962.

[46] L. V. Keldysh. Diagram technique for nonequilibrium processes. *Soviet Physics JETP*, 20:101, 1965.

[47] Jian-Sheng Wang, Bijay Kumar Agarwalla, Huanan Li, and Juzar Thingna. Nonequilibrium Green's function method for quantum thermal transport. *Frontiers of Physics*, 9(6):673–697, December 2014.

[48] M Ridley, N W Talarico, D Karlsson, N Lo Gullo, and R Tuovinen. A many-body approach to transport in quantum systems: from the transient regime to the stationary state. *Journal of Physics A: Mathematical and Theoretical*, 55(27):273001, June 2022. Publisher: IOP Publishing.

[49] M.P. Anantram, M.S. Lundstrom, and D.E. Nikonov. Modeling of Nanoscale Devices. *Proceedings of the IEEE*, 96(9):1511–1550, September 2008.

[50] Toshihito Umegaki, Matsuto Ogawa, and Tanroku Miyoshi. Investigation of electronic transport in carbon nanotubes using Green's-function method. *Journal of Applied Physics*, 99(3):034307, February 2006.

[51] Akansha Thakur and Niladri Sarkar. A tutorial on the NEGF method for electron transport in devices and defective materials. *The European Physical Journal B*, 96(8):113, August 2023.

[52] M. P. Lopez Sancho, J. M. Lopez Sancho, J. M. L. Sancho, and J. Rubio. Highly convergent schemes for the calculation of bulk and surface Green functions. *Journal of Physics F: Metal Physics*, 15(4):851, April 1985.

[53] Liu Yang, M. P. Anantram, Jie Han, and J. P. Lu. Band-gap change of carbon nanotubes: Effect of small uniaxial and torsional strain. *Physical Review B*, 60(19):13874–13878, November 1999.

[54] Mohesn Eghbalian, Reza Ansari, and Saeed Rouhi. Effects of geometrical parameters and functionalization percentage on the mechanical properties of oxygenated single-walled carbon nanotubes. *Journal of Molecular Modeling*, 27(12):351, November 2021.

[55] Zhongfan Liu, Jin Zhang, and Bo Gao. Raman spectroscopy of strained single-walled carbon nanotubes. *Chemical Communications*, (45):6902, 2009.

[56] Hui Wang, Xiang Cai, Xinyi Zheng, Yan Li, Bing Han, Haoyu Zhang, Xiaowei He, Huaping Liu, Qinghong Yuan, and Sheng Wang. Carbon Nanotube Intramolecular Junction Photodetector Via Strain Engineering. *Small*, n/a(n/a):2502735. _eprint: https://onlinelibrary.wiley.com/doi/pdf/10.1002/smll.202502735.